The Skyrme Model: Curved Space, Symmetries and Mass

THOMAS SIMON WINYARD

The Skyrme Model: Curved Space, Symmetries and Mass

Thomas Winyard

A Thesis presented for the degree of
Doctor of Philosophy

Centre for Particle Theory
Department of Mathematical Sciences
University of Durham
England

February 2016

Dedicated to

Fiona, Robert, Joseph and Isabelle Winyard

The Skyrme Model: Curved Space, Symmetries and Mass

Thomas Winyard

Submitted for the degree of Doctor of Philosophy
February 2016

Abstract

The presented thesis contains research on topological solitons in $(2+1)$ and $(3+1)$ dimensional classical field theories, focusing upon the Skyrme model. Due to the highly non-linear nature of this model, we must consider various numerical methods to find solutions.

We initially consider the $(2+1)$ baby Skyrme model, demonstrating that the currently accepted form of minimal energy solutions, namely straight chains of alternating phase solitons, does not hold for higher charge. Ring solutions with relative phases changing by π for even configurations or $\pi - \pi/B$ for odd numbered configurations, are demonstrated to have lower energy than the traditional chain configurations above a certain charge threshold, which is dependant on the parameters of the model. Crystal chunk solutions are then demonstrated to take a lower energy but for extremely high values of charge. We also demonstrate the infinite charge limit of each of the above configurations. Finally, a further possibility of finding lower energy solutions is discussed in the form of soliton networks involving rings/chains and junctions. The dynamics of some of these higher charge solutions are also considered.

In chapter 3 we numerically simulate the formation of $(2+1)$-dimensional baby Skyrmions from domain wall collisions. It is demonstrated that Skyrmion, anti-Skyrmion pairs can be produced from the interaction of two domain walls, however the process can require quite precise conditions. An alternative, more stable, formation process is proposed and simulated as the interaction of more than two segments

of domain wall. Finally domain wall networks are considered, demonstrating how Skyrmions may be produced in a complex dynamical system.

The broken planar Skyrme model, presented in chapter 4, is a theory that breaks global $O(3)$ symmetry to the dihedral group D_N. This gives a single soliton solution formed of N constituent parts, named partons, that are topologically confined. We show that the configuration of the local energy solutions take the form of polyform structures (planar figures formed by regular N-gons joined along their edges, of which polyiamonds are the $N = 3$ subset). Furthermore, we numerically simulate the dynamics of this model.

We then consider the $(3 + 1)$ $SU(2)$ Skyrme model, introducing the familiar concepts of the model in chapter 5 and then numerically simulating their formation from domain walls. In analogue with the planar case, it is demonstrated that the process can require quite precise conditions and an alternative, more stable, formation process can be achieved with more domain walls, requiring far less constraints on the initial conditions used.

The results in chapter 7 discuss the extension of the broken baby Skyrme model to the 3-dimensional $SU(2)$ case. We first consider the affect of breaking the isospin symmetry by altering the tree level mass of one of the pion fields breaking the $SO(3)$ isospin symmetry to an $SO(2)$ symmetry. This serves to exemplify the constituent make up of the Skyrme model from ring like solutions. These rings then link together to form higher charge solutions. Finally the mass term is altered to allow all the fields to have an equivalent tree level mass, but the symmetry of the Lagrangian to be broken, firstly to a dihedral symmetry D_N and then to some polyhedral symmetries.

We now move on to discussing both the baby and full $SU(2)$ Skyrme models in curved spaces. In chapter 8 we investigate $SU(2)$ Skyrmions in hyperbolic space. We first demonstrate the link between increasing curvature and the accuracy of the rational map approximation to the minimal energy static solutions. We investigate the link between Skyrmions with massive pions in Euclidean space and the massless case in hyperbolic space, by relating curvature to the pion mass. Crystal chunks are found to be the minimal energy solution for increased curvature as well as increased mass of the model. The dynamics of the hyperbolic model are also simulated, with

the similarities and differences to the Euclidean model noted.

One of the difficulties of studying the full Skyrme model in $(3+1)$ dimensions is a possible crystal lattice. We hence reduce the dimension of the model and first consider crystal lattices in $(2+1)$-dimensions. In chapter 9 we first show that the minimal energy solutions take the same form as those from the flat space model. We then present a method of tessellating the Poincare disc model of hyperbolic space with a fundamental cell. The affect this may have on a resulting Skyrme crystal is then discussed and likely problems in simulating this process.

We then consider the affects of a pure AdS background on the Skyrme model, starting with the massless baby Skyrme model in chapter 10. The asymptotics and scale of charge 1 massless radial solutions are demonstrated to take a similar form to those of the massive flat space model, with the AdS curvature playing a similar role to the flat space pion mass. Higher charge solutions are then demonstrated to exhibit a concentric ring-like structure, along with transitions (dubbed popcorn transitions in analogy with models of holographic QCD) between different numbers of layers. The 1^{st} popcorn transitions from an n layer to an $n+1$-layer configuration are observed at topological charges 9 and 27 and further popcorn transitions for higher charges are predicted. Finally, a point-particle approximation for the model is derived and used to successfully predict the ring structures and popcorn transitions for higher charge solitons.

The final chapter considers extending the results from the penultimate chapter to the full $SU(2)$ model in a pure AdS_4 background. We make the prediction that the multi-layered concentric ring solutions for the 2-dimensional case would correlate a multi-layered concentric rational map configuration for the 3-dimensional model. The rational map approximation is extended to consider multi-layered maps and the energies demonstrated to reduce the minimal energy solution for charge $B = 11$ which is again dubbed a popcorn transition. Finally we demonstrate that the multi shell structure extends to the full field solutions which are found numerically. We also discuss the affect of combined symmetries on the results which (while likely to be important) appear to be secondary to the dominant effective potential of the metric which simulates a packing problem and hence forces the popcorn transitions

to act accordingly with the 2-dimensional model.

Declaration

The work in this thesis is based on research carried out at the Particle Theory Group, the Department of Mathematical Sciences, Durham University, England. No part of this thesis has been submitted elsewhere for any other degree or qualification and it is all my own work unless referenced to the contrary in the text.

Acknowledgements

First and foremost I must thank my supervisor Paul Sutcliffe who has always been forthcoming with useful advice and guidance throughout my PhD and has demonstrated great patience with my shortcomings, especially my inability to complete paperwork. I would also like to thank a number of people for useful discussions. A special mention should be given to Paul Jennings, Alex Cockburn and Matthew Elliot-Ripley although there are many others.

Next I need to thank my family for their well grounded influence. My father and brother for the many alcohol fuelled arguments we have had on all topics over the dinner table and my mother for being one of the kindest and most supporting people I have encountered.

Finally I would like to thank those that encouraged me, especially at an early age, to be interested in the world around me. Paul Togher for sharing interesting and often confusing ideas about physics in a simple manner. Also Brian Dallaway for his ability to inspire and for demonstrating that there is more to physics than written exams, which ultimately pushed me to pursue a degree in the subject.

Contents

List of Figures

List of Tables

Preface

The majority of the work within this thesis is focussed on the Skyrme model of nuclear physics. It has mostly been published (or currently going through the publication process) in various journals, throughout my PhD.

The papers that contain some of the work presented in this thesis (though not in its entirety) are given, in order of release, with references below.

1. Broken Planar Skyrmions - Statics and Dynamics [1]
2. Hyperbolic Skyrmions [2]
3. Baby Skyrmions in AdS [3]
4. Skyrmion and Baby Skyrmion Formation from Domain Walls [4] (Accepted and appearing in Phys Rev D shortly)

Papers that are based upon the work in this thesis that are to be released as preprints shortly are as follows,

1. Broken Skyrmions
2. Numerical Solutions of the baby Skyrme Model
3. Hyperbolic Baby Skyrmions

Part I

Introduction

Chapter 1

Introduction

Solitons are stable solutions to nonlinear PDEs that give finite, smooth, localised lumps of energy. In particular we are interested in soliton solutions that exist within field theories and are stabilised due to some topological nature. These field theories will be defined by some set of fields (that take the form of functions mapping between two manifolds), along with an energy functional.

The study of solitons often necessitates a wide range of analytical approaches. However except in the most constrained cases, solutions are often only attainable via computationally intensive numerical techniques. Solitons are of considerable interest in particle theory, condensed matter physics and cosmology as well as many other fields.

For a comprehensive look at various types of soliton solutions and soliton theory see [5].

1.1 Soliton Theory

1.1.1 Topology

For topological solitons to exist, the solutions to a given energy functional must lie within a set of distinct manifolds. Each manifold in this set is a configuration space, classified by a topological invariant or topological charge, that is conserved. It is defined in integral form as [5],

$$B_\Phi = \int_X \Phi^\star(\Omega) \tag{1.1.1}$$

where B_Φ is the topological degree of the map $\Phi : X \to Y$ and $\Phi^\star$ the pullback of the normalised volume form Ω on Y. This can quite often be related to homotopy groups, for example $\Phi : S^n \to S^n$ has the important homotopy group $\pi_n(S^n) = \mathbb{Z}$ which is isomorphic to the integers, thus the degree of the map will take integer values. The exact nature of this topological charge will depend upon the nature of the field theory considered e.g. in the example above it acts as a winding number. Thus we have a set of distinct solutions, that cannot be continuously deformed into one another.

1.1.2 Derrick's Theorem

The final necessity for soliton solutions to occur is agreement with Derrick's theorem [6]. Derrick noted that for many flat space field theories, the energy functional has no minimal field configurations with respect to spatial rescaling, except the vacuum. Were non-vacuum solutions to exist they should be stable to spatial rescalings. Due to this, these theories, while they may still have homotopy classes, each class has the minimal energy solution of the vacuum, hence our set of solutions just has multiplicity equal to the order of the set and is trivial.

This can be interpreted as requiring both an expansion term and a dissipative term in the energy functional. Otherwise the solutions could shrink to a point or expand indefinitely. If we consider a spatial rescaling $\boldsymbol{x} \to \mu\boldsymbol{x}$, with $\mu > 0$ then $\Phi^{(\mu)}(\boldsymbol{x})$ is the one-parameter family of applying the rescaling to a field configuration $\Phi(\boldsymbol{x})$, where we define

$$e(\mu) = E\left(\Phi^{(\mu)}(\boldsymbol{x})\right). \tag{1.1.2}$$

Suppose that for an arbitrary, finite energy field configuration $\Phi(\boldsymbol{x})$, which is not the vacuum, the function $e(\mu)$ has no stationary point. Then the theory has no static solutions of the field equation with finite energy, other than the vacuum.

Naturally the scaling has to be defined based upon the form of the field configuration $\Phi(\boldsymbol{x})$, e.g. for a scalar field configuration the natural rescaling is,

$$\phi^{(\mu)}(\boldsymbol{x}) = \phi(\mu\boldsymbol{x}). \tag{1.1.3}$$

1.2 Kinks and Domain Walls

1.2.1 ϕ^4 Kinks

It is easiest to grasp the concepts introduced above when considering a simple example. Kinks are solutions in a $1+1$ dimensional field theory, with the Lagrangian density

$$\mathcal{L} = \frac{1}{2}\partial^\mu\phi\partial_\mu\phi - U(\phi) \tag{1.2.4}$$

It is standard practice to ensure that the vacua of the theory will occur when the potential is zero $U = 0$, which occurs at the points that form a submanifold $\mathcal{V} \subset \mathbb{R}$, which is the vacua manifold of the theory. It is a requirement to have multiple vacua for soliton solutions, as otherwise the homotopy group $\pi_0(\mathcal{V})$ is trivial.

Due to finite energy requirements, we require that the limit of the field at spatial infinity is the vacuum $\lim_{x\to\pm\infty} U = U(\phi_\pm) = 0$. If we select the same vacua for both directions $\phi_+ = \phi_-$, then the minimal energy solution is naturally the vacuum throughout space $\phi(x) = \phi_\pm$. It is quite clear that were I to select any path between the two vacua at spatial infinity, it could be continuously deformed such that the field lies in the vacuum at all points.

However if we select different vacua, then the solution must interpolate between them in some way. This gives our solution some topology and hence a topological charge. The soliton also obeys Derrick's theorem, applying a spatial rescaling of the energy functional to obtain

$$e(\mu) = \mu E_2 + \frac{1}{\mu}E_0 \tag{1.2.5}$$

where the subscript of each term gives the number of spatial derivatives. Thus

a minimum exists for some finite value of μ. The potential term will be minimised if the interpolation is as steep as possible while the gradient term will be minimised by a shallower interpolation. These two competing terms will cause the soliton to have a finite size.

The energy can be easily shown to be bounded below using the Bogomolny equations, which reduce the 2nd order equations to 1st order [7].

$$E \geq \left| \int_{\phi_-}^{\phi_+} \sqrt{2U\left(\phi\right)} d\phi \right| \tag{1.2.6}$$

These sorts of bounds for the energy of the system in purely terms of topological data are attainable in many soliton systems and will be used later in the thesis.

The simplest choice of $U\left(\phi\right)$ that admits kink like solutions is one with two vacua, such that the homotopy group becomes $\pi_0\left(\mathcal{V}\right) = \mathbb{Z}_2$. The simplest form for a polynomial in ϕ^2 is a quartic form, along with some simple assumptions we obtain the potential

$$U\left(\phi\right) = \lambda\left(m^2 - \phi^2\right)^2 \tag{1.2.7}$$

where the degenerate global minima occur at $\phi = \pm m$. We can now write the topological data of this system quite intuitively,

$$N = \frac{\phi_+ - \phi_-}{2m} = \frac{1}{2m}\int_{-\infty}^{\infty} \phi'\, dx \tag{1.2.8}$$

The Bogomolny equation can also be rewritten as,

$$\phi' = \sqrt{2\lambda}\left(m^2 - \phi^2\right) \tag{1.2.9}$$

which unlike most equations for topoligcal systems can be integrated to yield an exact analytical solution,

$$\phi\left(x\right) = m\tanh\left(\sqrt{2\lambda} m\left(x - a\right)\right), \tag{1.2.10}$$

where a is a constant from the integration and represents the translational symmetry of the solution. Substituting this into the energy equation we obtain

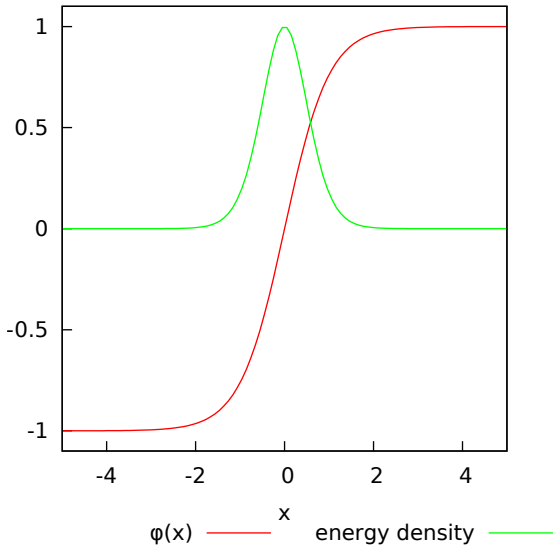

Figure 1.1: Plot of a kink solution with charge $N = 1$, for the parameters $\lambda = \frac{1}{2}, m = 1, a = 0$. The red line indicates the field $\phi(x)$ and the green line the energy density $\mathcal{E}(x)$. The position of the soliton is interpreted to be at $a = 0$.

$$E = \int_{-\infty}^{\infty} \mathcal{E}(x)\, dx = \int_{-\infty}^{\infty} 2\lambda m^4 \sec^4\left(\sqrt{2\lambda} m\,(x-a)\right)\, dx = \frac{4}{3} m^3 \sqrt{2\lambda}. \tag{1.2.11}$$

We plot both the form of the field $\phi\,(x)$ and energy density $\mathcal{E}(x)$ in figure 1.1. We can see that the point at which the field is half way through its interpolation ($\phi\,(x) = 0$), is also the point at which the energy density is maximal, as well as the topological charge density (which has a similar shape to the energy density profile). This point occurs as the point $x = a$ which is naturally interpreted as the position of the topological soliton, this interpretation will be useful later in defining the position of more complicated solitons.

A final note on the dynamics of the system, we can Lorentz boost our static solution to obtain a dynamical solution with velocity v,

$$\phi\,(t, x) = m \tanh\left(\sqrt{2\lambda} m\gamma\,(x - vt - a)\right). \tag{1.2.12}$$

In our units $c = 1$ is the speed of light and γ is the Lorentz factor. We can now consider multiple kinks in our system. While our topological charge N cannot

exceed 1 we can place chains of alternating kink anti-kink solutions whose local charge density, when summed, cancel, causing the total charge not to exceed 1. If we superimpose these solutions well separated we can interpret them as multiple solitons that ultimately attract and annihilate. If we include a damping term to remove any additional kinetic energy the solution will eventually reduce to the static solution we had before. The interaction of a kink and anti-kink can be seen in figure 1.2.

It is clear that a kink and anti-kink will attract as shown above and ultimately annihilate. The force of this attraction can actually be calculated analytically for a well separated configuration.

One thing that reduces the complexity and also interesting nature of the ϕ^4 model is the non-existence of stable multi-kink solutions, which is due to the simplistic nature of it's vacua structure. It isn't difficult to consider a system that will produce multi-kink solutions, with one of the simplest being the Sine-Gordon model [8],

$$\mathcal{L} = \frac{1}{2}\partial_\mu\phi\partial^\mu\phi - (1 - \cos\phi) \tag{1.2.13}$$

where vacua solutions are of the form $\phi = 2\pi n$, where $n \in \mathbb{Z}$, giving the vacua structure to be,

$$\pi_0(\mathcal{V}) = \mathbb{Z}. \tag{1.2.14}$$

This is a far richer model, that has applications to modelling elementary particles [9]. We have chosen not the consider it however due to the relation of ϕ^4 kinks to domain walls in higher dimensional theories. That being said, the Sine-Gordon model is perhaps a much better introductory look at soliton solutions with copious information available in [5].

1.2.2 Domain Walls

Domain walls are similar to kinks, being an interpolation between vacua in one spatial dimension, however they exist in higher dimensional theories. This of course means that the field configuration is now independent in at least one spatial direc-

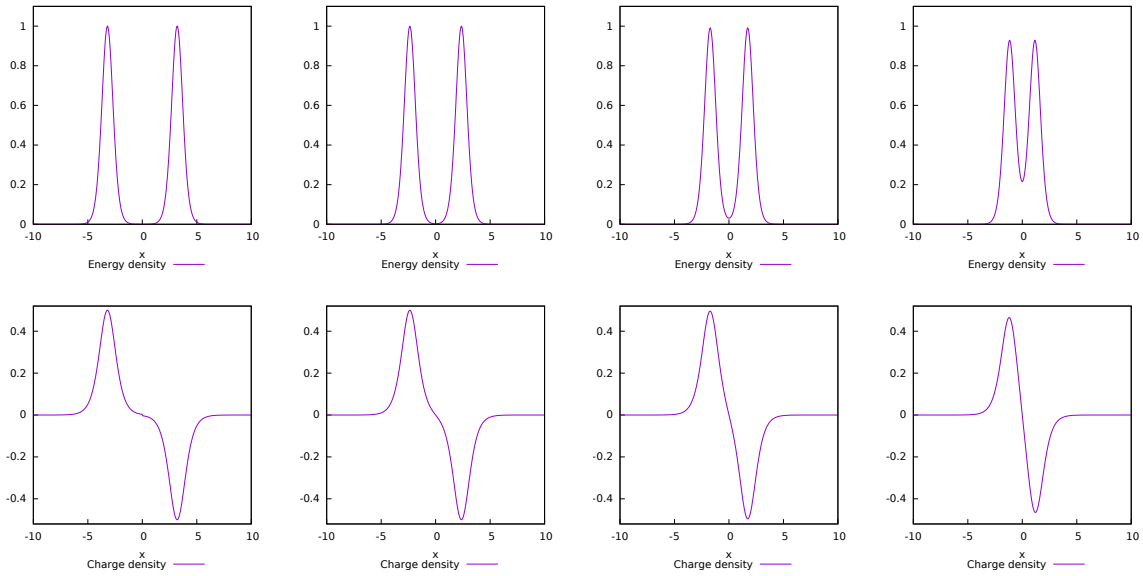

$t = 0$ $t = 120$ $t = 132$ $t = 135.2$

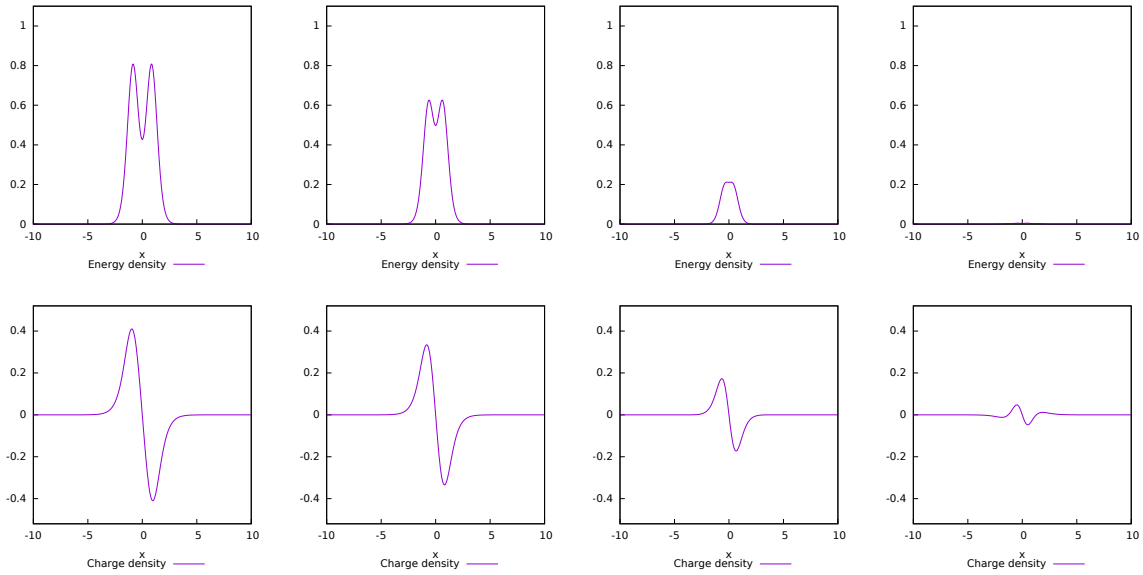

$t = 136$ $t = 136.4$ $t = 136.8$ $t = 137$

Figure 1.2: Plot at various time slices of a well separated kink anti-kink system with no initial velocity attracting and annihilating. The top plot shows the potential energy density, while the lower plot shows the topological charge density. The total charge remains zero throughout the simulation. Simulation was performed using a 4th order Runga-Kutta numerical technique on a grid with $dx = 0.01$. Parameters used were $m = 1$ and $\lambda = \frac{1}{2}$. Initial conditions were formed using a superposition of the fields $\phi(x) = \phi_1(x) + \phi_2(x) + 1$.

tion, $\phi(x^1,t) = m\tanh\left(\sqrt{2\lambda}m\gamma\left(x^1 - vt - a\right)\right)$. This means that domain walls are no longer topological soliton solutions as they have infinite length. If we were to consider the effect on the boundary in the infinite directions, we observe that there must be an interpolation on the boundary, meaning they contribute infinite energy. They are useful to consider in finite systems as interpolations between different vacua throughout space, that have occurred due to phase transitions. Domain walls are of great interest in cosmology due to phase transitions in the early universe [10], as well as finite condensed matter systems [11].

While domain walls contain no topological charge in and of themselves, they do have stability requirements, similar to that of Derrick's theorem. The interpolation of vacua solutions gives the topological stability requirement. Domain walls that interpolate the field in opposite directions will attract and annihilate, similar to figure 1.2 in the 1-dimensional case.

1.3 Sigma Model

If we consider the extension of the kink model to $(d+1)$ dimensions, then we can perform a spatial rescaling of the resulting energy,

$$e\left(\mu\right) = \mu^d E_2 + \mu^{d-2} E_0. \tag{1.3.15}$$

To satisfy Derrick's theorem we can only have $d = 1$ in the above case, or there will be no minimum with respect to μ. Hence for soliton solutions to be stable in higher dimensional theories, we need to adjust the terms. For $d = 2$, one possible way is to remove the mass term $E_0 = 0$, making the theory conformally invariant. This is known as the $O\left(3\right)$ sigma model in $(2+1)$ dimensions [12], with Lagrangian density,

$$\mathcal{L} = \frac{1}{4}\partial_\mu \boldsymbol{\phi}\cdot\partial^\mu\boldsymbol{\phi} + \nu\left(1 - \boldsymbol{\phi}\cdot\boldsymbol{\phi}\right) \tag{1.3.16}$$

where $\boldsymbol{\phi}$ is a 3-component unit vector field, with the constraint that $\boldsymbol{\phi}\cdot\boldsymbol{\phi} = 1$ enforced by the Lagrange multiplier ν.

While this method of evading Derrick's theorem will give static solutions that will not evolve, they are not minima with respect to spatial rescalings and hence are

not true topological soliton solutions, they are called lump like solutions.

We want to consider this theory in both $d = 2$ and 3 dimensions, however due to Derrick's theorem we will need additional terms to stabilise our solutions. The relevant models will be presented in sections 2 and 3 in detail.

Part II

(2+1) Baby Skyrme Model

Chapter 2

Baby Skyrme Model

2.1 Introduction

The work in this section is initially introductory in nature (though some additional local minima were produced for charges $B = 6, 7$ as they are of use later), but section 3 onwards contains my own work on higher charge solutions, followed by some interesting dynamical systems. My own work in this chapter is intended to be placed into a paper to appear on the arxiv shortly.

The Skyrme model [13] is a $(3+1)$-dimensional theory that admits soliton solutions, called Skyrmions, which represent baryons. This has been well studied [5] and is discussed in detail in chapter 5. In this chapter however we consider the baby (or planar) Skyrme model [14] which is the $(2+1)$-dimensional analogue of the full Skyrme model. Baby Skyrmions are of great interest in condensed matter physics, where they have been proposed as a future candidate for creating superior memory storage devices [15, 16]. They appear in many systems such as ferromagnetic quantum Hall systems [17], and more recently have been observed in chiral ferromagnets [18]. They are also useful as a toy model for the full Skyrme model, which is a candidate for describing baryons within a nonlinear theory of mesons.

2.2 The Model

The planar Skyrme model has the form of a non-linear modified sigma model, described by the Lagrangian density

$$\mathcal{L} = \frac{1}{2}\partial_\mu \boldsymbol{\phi} \cdot \partial^\mu \boldsymbol{\phi} - \frac{\kappa^2}{4}\left(\partial_\mu \boldsymbol{\phi} \times \partial_\nu \boldsymbol{\phi}\right) \cdot \left(\partial^\mu \boldsymbol{\phi} \times \partial^\nu \boldsymbol{\phi}\right) - m^2 V[\boldsymbol{\phi}], \tag{2.2.1}$$

where $\boldsymbol{\phi}(\mathbf{x}, t)$ is a 3-component unit vector field, $\boldsymbol{\phi} = (\phi_1, \phi_2, \phi_3)$. The energy of the model can be written as

$$\begin{aligned} E = &\int \left(\frac{1}{2}\dot{\boldsymbol{\phi}} \cdot \dot{\boldsymbol{\phi}} + \frac{\kappa^2}{2}(\dot{\boldsymbol{\phi}} \times \partial_i \boldsymbol{\phi}) \cdot (\dot{\boldsymbol{\phi}} \times \partial_i \boldsymbol{\phi})\right) \mathrm{d}^2\mathbf{x} \\ &+ \int \left(\frac{1}{2}\partial_i \boldsymbol{\phi} \cdot \partial_i \boldsymbol{\phi} + \frac{\kappa^2}{4}\left(\partial_i \boldsymbol{\phi} \times \partial_j \boldsymbol{\phi}\right) \cdot \left(\partial_i \boldsymbol{\phi} \times \partial_j \boldsymbol{\phi}\right) + m^2 V[\boldsymbol{\phi}]\right) \mathrm{d}^2\mathbf{x}. \end{aligned} \tag{2.2.2}$$

This energy functional has $O(3)$ symmetry (dependant on the choice of mass term $V[\boldsymbol{\phi}]$). The vacuum solution takes the form of any constant value of $\boldsymbol{\phi}$, that results in $V[\phi] = 0$.

Due to finite energy arguments, the model requires $\boldsymbol{\phi}$ to be the vacuum at spatial infinity $\lim_{|\boldsymbol{x}|\to\infty} \boldsymbol{\phi} = \boldsymbol{\phi}_\infty$, which without loss of generality can be chosen to be $\boldsymbol{\phi}_\infty = (0, 0, 1)$. Hence it can be viewed as the map from the compactified physical space, $\mathbb{R}^2 \cup \{\infty\} = S^2$ to the target space S^2. Since the second homotopy group $\pi_2(S^2) = \mathbb{Z}$, the degree of this map can be characterised as a winding number. This degree gives the topological charge of a solution and can be calculated using the pull back of the normalised area form of the target space S^2, to give an integral form of,

$$B = -\frac{1}{4\pi}\int \boldsymbol{\phi} \cdot \left(\partial_1 \boldsymbol{\phi} \times \partial_2 \boldsymbol{\phi}\right) \mathrm{d}^2\mathbf{x}. \tag{2.2.3}$$

The selection of the field on the boundary of the space breaks the $O(3)$ symmetry of the model to an $O(2)$ symmetry, which acts on the fields ϕ_1 and ϕ_2. We will also consider models with symmetries that are subgroups of this, through particular choices of the mass term $V[\boldsymbol{\phi}]$.

Applying a rescaling $\boldsymbol{x} \to \mu\boldsymbol{x}$ to the energy functional (2.2.2) of the model, we acquire the following,

$$e\left(\mu\right) = E_2 + \mu^2 E_4 + \frac{1}{\mu^2}E_0. \tag{2.2.4}$$

For non-zero potential energy, static soliton solutions are possible. This is due to the addition of the second term in the Lagrangian, stabilising the sigma model to spatial rescalings, which was shown to be unstable in the previous section.

This term is referred to as the Skyrme term, in accordance with its relation to the 3-dimensional Skyrme model. Hence soliton solutions of the theory are referred to as planar or baby Skyrmions. While any term that is more than quadratic in derivatives would stabilise the sigma model, the Skyrme term is unique in that it is the lowest order expression, that retains the second order nature of the equations of motion in terms of time derivatives. By differentiating the above equation we can also obtain that the scale of the soliton is proportional to the constant $\sqrt{\kappa/m}$.

As this is a modification of the sigma model by the addition of a positive definite term, the same lower bound can be used through a Bogomolny type argument.

$$\begin{aligned} E &\geq \int \frac{1}{2}\left(\partial_i \boldsymbol{\phi}\cdot\partial_i\boldsymbol{\phi}\right)\, d^2\boldsymbol{x} \\ &= \int \left\{\frac{1}{4}\left(\partial_i\boldsymbol{\phi}\pm\epsilon_{ij}\boldsymbol{\phi}\times\partial_j\boldsymbol{\phi}\right)\cdot\left(\partial_i\boldsymbol{\phi}\pm\epsilon_{ik}\boldsymbol{\phi}\times\partial_k\boldsymbol{\phi}\right)\pm\frac{1}{2}\epsilon_{ij}\boldsymbol{\phi}\cdot\left(\partial_i\boldsymbol{\phi}\times\partial_j\boldsymbol{\phi}\right)\right\} d^2\boldsymbol{x} \\ &\geq \int \pm\boldsymbol{\phi}\cdot\left(\partial_1\boldsymbol{\phi}\times\partial_2\boldsymbol{\phi}\right)\, d^2\boldsymbol{x} \\ &= 4\pi\,|B| \end{aligned} \tag{2.2.5}$$

The energy of a baby Skyrmion exceeds this lower bound, tending towards 4π as $m\to 0$. It however cannot attain this bound as the mass term is required for stable solutions and the size of the solution becomes infinite in the limit.

The field equation that follows from the Lagrangian is,

$$\begin{aligned} -m^2\frac{\delta V}{\delta\boldsymbol{\phi}} - \partial_\mu\partial^\mu\boldsymbol{\phi} + \kappa^2\left[\partial_\mu\partial^\mu\boldsymbol{\phi}(\partial_\nu\boldsymbol{\phi}\cdot\partial^\nu\boldsymbol{\phi}) + \partial_\mu\boldsymbol{\phi}(\partial_\nu\boldsymbol{\phi}\cdot\partial^\mu\partial^\nu\boldsymbol{\phi})\right. \\ \left. -\partial_\mu\partial_\nu\boldsymbol{\phi}(\partial^\mu\boldsymbol{\phi}\cdot\partial^\nu\boldsymbol{\phi}) - \partial_\mu\boldsymbol{\phi}(\partial^\mu\boldsymbol{\phi}\cdot\partial_\nu\partial^\nu\boldsymbol{\phi})\right] + \lambda\boldsymbol{\phi} = 0, \end{aligned} \tag{2.2.6}$$

where λ is a Lagrange multiplier to enforce the condition that $\boldsymbol{\phi}\cdot\boldsymbol{\phi}=1$, that results from the addition of a zero value term $\lambda\left(\boldsymbol{\phi}\cdot\boldsymbol{\phi}-1\right)$ to the Lagrangian. The form for λ can be found by taking the scalar product of the e.o.m. and rearranging. While this is sufficient analytically, numerically we will need to pull our target space back onto the sphere regularly by normalising the value of $\boldsymbol{\phi}$ after each loop. If we are

considering dynamics we will need to do a similar process for the time derivative, removing any component of $\boldsymbol{\phi}$ to ensure $\partial_t \boldsymbol{\phi} \cdot \boldsymbol{\phi} = 0$ The field equation is highly non-linear, and to study the behaviour of the system we must resort to numerical techniques.

A variety of different potentials have been proposed [19–22], the standard potential term [14] is the analogue of the pion mass term in the Skyrme model,

$$V[\boldsymbol{\phi}] = 1 - \phi_3. \tag{2.2.7}$$

This choice of potential term breaks the general $O(3)$ symmetry to an $O(2)$ symmetry, selecting the unique vacuum to be $\boldsymbol{\phi}_\infty = (0, 0, 1)$, which is the boundary value we have selected throughout regardless. We will use this mass term throughout this chapter.

2.3 Low Charge Solutions

Due to the principle of symmetric criticality and the symmetries of our energy functional and space, one would expect a static charge 1 solution to have $O(2)$ symmetry. This is in fact the case for both $B = 1$ and 2, as can be seen in figure 2.2 for full field simulations. This symmetry can be used to reduce the dimensionality of the energy functional (2.2.2), using the radial ansatz

$$\boldsymbol{\phi} = \left(\sin f(\rho) \cos B\theta, \sin f(\rho) \sin B\theta, \cos f(\rho)\right), \tag{2.3.8}$$

where ρ, θ are polar coordinates and $f(\rho)$ is a monotonically decreasing profile function, that has the boundary conditions $f(0) = \pi$ and $f(\infty) = 0$. This is not an analytic solution to the equations, as the profile function must be obtained numerically. Note that this initial approximation has the maximal symmetry $O(2)$, in the sense that the spatial rotation $\theta \to \theta + \alpha$ can be compensated for by global rotation symmetry, while the reflection $\theta \to -\theta$ can be balanced by a global reflection. Substituting this into the energy functional (2.2.2) we get the following 1-dimensional energy,

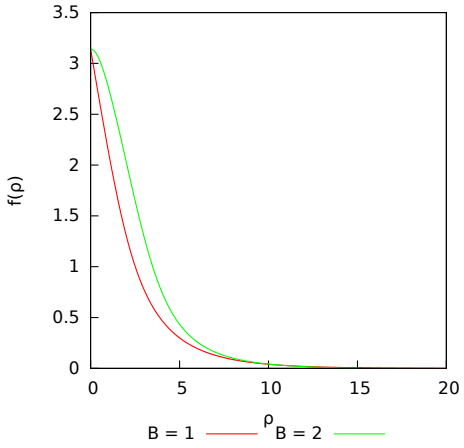

Figure 2.1: Profile functions for radial ansatz $f(\rho)$ of charges 1 and 2, found by a gradient flow method for parameters $\kappa = 1$, $m = \sqrt{0.1}$.

$$E = 2\pi \int_0^\infty \left\{ \frac{1}{2} f'^2 + \left(1 + \kappa^2 f'^2\right) \frac{B^2}{2r^2} \sin^2 f + m^2 \left(1 - \cos f\right) \right\} r \, dr \tag{2.3.9}$$

Varying the energy in (2.3.9) gives the following equation of motion

$$\left(1 + \frac{\sin f^2}{\rho^2}\right) f'' + \left(1 - \frac{\sin f^2}{\rho^2}\right) \frac{f'}{\rho} + \frac{\sin 2f}{2\rho^2} \left(f'^2 - 1\right) - m^2 \sin f = 0 \tag{2.3.10}$$

Linearising this equation gives the asymptotic behaviour of the baby Skyrmions to be exponential,

$$f\left(\rho\right) \sim \frac{A}{\sqrt{\rho}} e^{-m\rho}, \tag{2.3.11}$$

unlike the algebraic decay of the massless lump solutions of the $O(3)$ sigma model.

The profile function can be found using a simple gradient flow method on (2.3.9) and is displayed for the parameters $m = \sqrt{0.1}$ $\kappa = 1$ for charge 1 and 2 in figure 2.1.

This radial approach can be generalised for all charges, however it is only the global minimal energy solution for $B = 1, 2$ and only forms a local minimum for higher charges, requiring a smaller perturbation to flow to a lower energy solution as the charge increases.

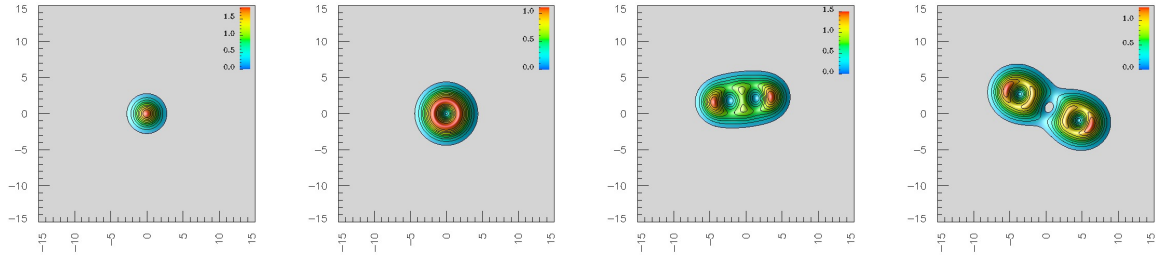

(a) $B = 1$ (b) $B = 2$ (c) $B = 3$ (d) $B = 4$

Figure 2.2: Energy density contour plots for charges $B = 1 - 4$ minimal energy solutions for $\kappa = 1$ and $m^2 = 0.1$. Note, a contour plot using charge density produces a similar result.

To acquire the numerical solutions for all charges we must simulate the field equation (2.2.6). This was performed using a 4th order Runga-Kutta method with 2nd order finite difference derivatives. To find static solutions, the time derivative of the field was set to zero at regular intervals, or if the potential energy increased. To acquire the numerical solutions for higher charges, we must perturb some initial conditions that can then flow to a lower energy solution. The first initial configuration we can use is a perturbation of the radial ansatz above. An alternative method is to place lower charge solutions at various points of the grid using the product ansatz. We first describe our field using stereographic coordinates,

$$W = \frac{\phi_1 + i\phi_2}{1 + \phi_3}. \tag{2.3.12}$$

We can then assume that if the solitons are well separated in relation to their size, then we can approximate the resulting solution as,

$$W = \sum_{i}^{N} W_i \tag{2.3.13}$$

where N is the number of solitons and $B = \sum_i^N B_i$ is the total topological charge of the system.

Various combinations of the two types of initial conditions mentioned above were used to find numerical solutions upto charge $B = 10$. The grid was simulated using $dx = 0.057$. The results of this numerical process can be observed in figure 2.2 for

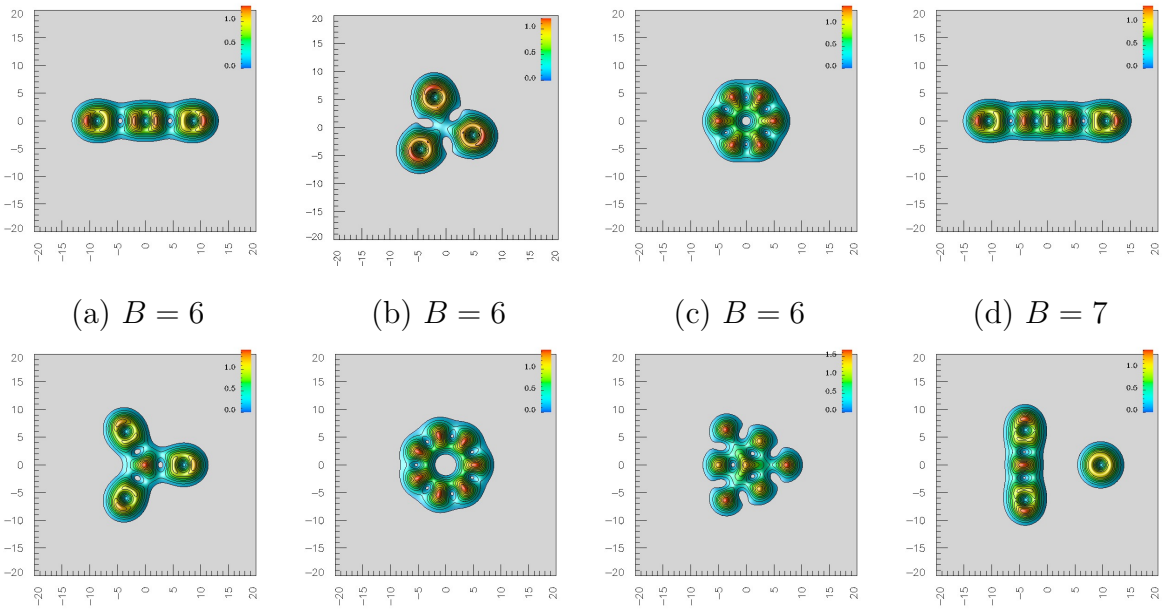

(a) $B = 6$ (b) $B = 6$ (c) $B = 6$ (d) $B = 7$

(e) $B = 7$ (f) $B = 7$ (g) $B = 7$ (h) $B = 7$

Figure 2.3: Energy density contour plots for charges $B = 6$ and $B = 7$ for configurations with similar energies. The chain solutions retain the global minimum. The parameters used for the model were $\kappa = 1$ and $m^2 = 0.1$. The energies of the configurations in these plots are shown in table 2.1.

charges $1 - 4$, whose global minimum are relatively simple to attain. This results are well known and were first found in [14].

For charges $6, 7$ we discover more local minima with similar energies to that of the global energy minimum. These are shown in figure 2.3 with the relative energies given in table 2.3, however the chain solution retains the global minimum as predicated in [23].

2.4 Higher Charge Solutions

It has been proposed in [23] that the minimal energy solutions for higher charges take the form of straight chains of single solitons alternating their phase by π. Here we consider additional forms of solution and compare the energies with the suggested straight chains.

B	$E/(4\pi B)$	G	Image
6^*	1.4622	D_2	2.3(a)
6	1.4632	D_3	2.3(b)
6	1.4717	D_6	2.3(c)
7^*	1.4619	D_2	2.3(d)
7	1.4637	D_3	2.3(e)
7	1.4806	D_7	2.3(f)
7	1.4965	D_3	2.3(g)
7	1.4659	D_2	2.3(h)

Table 2.1: Energies for various local minima for charges $B = 6, 7$ as shown in figure 2.3, for parameters $\kappa = 1$ and $m = \sqrt{0.1}$. The symmetry group G of the energy density configuration is also given. The global minimum solutions are indicated by a * by the charge and correspond to the chain solutions.

2.4.1 Rings/Chains

The most natural extension to the straight chains proposal is to realise that the energy density peaks at either end of the chains. This could be reduced by linking the ends into a ring-like solution. For even Baryon number the standard alternating of phases by π will suffice. However for an odd charge, alternating the phase by π would force two solitons with the same phase to sit adjacent, which has a large energy cost.

There are two ways of circumventing this. One is to alternate the phases by $\pi - \alpha$ where $\alpha = \pi/B$. Or alternatively one of the baby Skyrmions could be removed from the ring and sit either inside or outside the ring.

The energy density contour plots for $B = 20$ and $B = 21$ are presented in figure 2.4. Here the ring solutions have a lower energy than the predicted chain solutions. The energies for both chain and ring solutions for increasing charge are shown in both table 2.4.1 and figure 2.5.

Looking at the plot, we see that the chain solutions initially give the minimal energy and then the ring solutions become the minimal energy, tending towards the

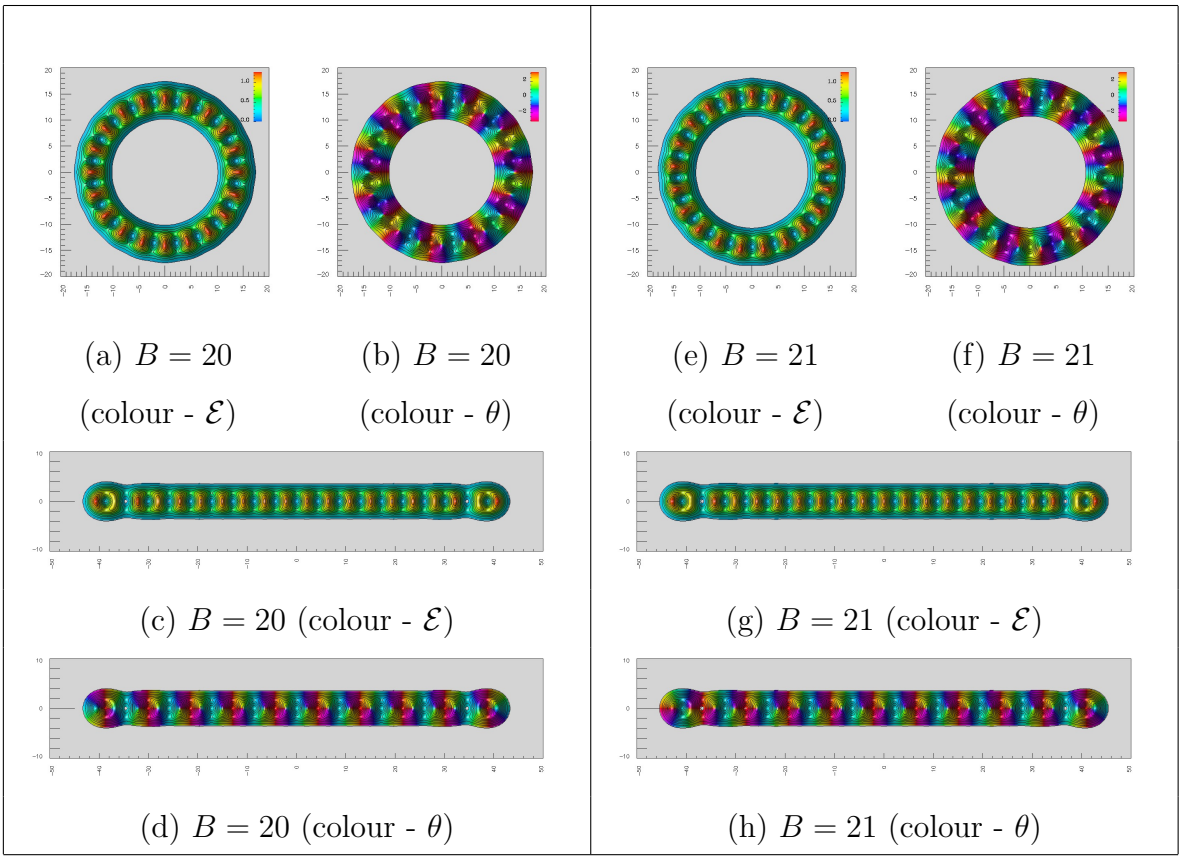

(a) $B = 20$ (colour - $\mathcal{E}$)

(b) $B = 20$ (colour - θ)

(e) $B = 21$ (colour - $\mathcal{E}$)

(f) $B = 21$ (colour - θ)

(c) $B = 20$ (colour - $\mathcal{E}$)

(g) $B = 21$ (colour - $\mathcal{E}$)

(d) $B = 20$ (colour - θ)

(h) $B = 21$ (colour - θ)

Figure 2.4: Energy density contour plots for ring and chain solutions for charges $B = 20$ and $B = 21$, coloured by the energy density ($\mathcal{E}$) or the phase $\theta = \tan^{-1}\frac{\phi_2}{\phi_1}$. The parameters used for the model were $\kappa = 1$ and $m^2 = 0.1$. The rings solutions here are the global minimum for these charges.

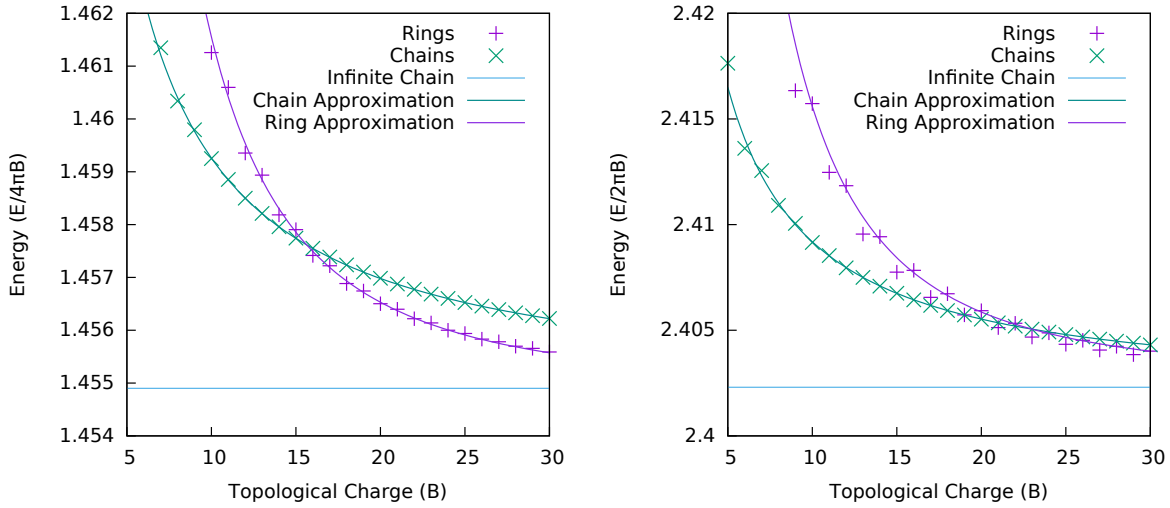

(a) $m = \sqrt{0.1}$ (b) $m = 1$

Figure 2.5: Plots of decreasing energy with charge for ring and chain solutions. The left plot is for $m = \sqrt{0.1}$ and the right $m = 1$. We see that the ring solutions start with a higher energy, but reduce toward the infinite chain energy faster than the chain solution for both values. Included is an approximation for the energies, assuming they can be written as predictable deviations from the infinite chain energy. The chain energy correction term, is given by the energy contribution of the stoppers. The ring correction term ,is given by the curvature of the ring.

infinite chain energy quicker. Note that the crossing point is different for the two choices of mass, so it would appear that the crossing point is dependent on the mass of the model. This is unsurprising, as it affects the scale of the solutions and hence the radius of the ring. With a higher curvature one would expect the defect in the energy to be higher.

The chain solutions appear to be very uniform, except for the ends of the chains which we refer to as stoppers. The uniform qualitatively matches up with that shown in the next section where infinite chains are discussed. It would appear that the deviation from the infinite chain energy is due to the stoppers. If this is the case it would lead to a predictable form for the energy, related to the topological charge B, namely for the energy normalised by the Bogomolny bound,

$$E_{chain} = E_\infty + \frac{2}{B} E_{stopper} \tag{2.4.14}$$

where E_∞ is the normalised energy of the infinite chain (found numerically in the next section) and $E_{stopper}$ is the energy contribution of each stopper in the system, normalised by 4π. If we perform a least squares fit on the data in figure 2.5, we get the chain approximation line plotted, which matches the data remarkably accurately. For $m = \sqrt{0.1}$ we get $E_\infty = 1.4547$ and $E_{stopper} = 0.02283$ and for $m = 1$ we get $E_\infty = 2.4019$ and $E_{stopper} = 0.03658$. These values for the infinite chain are very close the numerically calculated values in the next section, this along with the remarkable accuracy of the approximation, suggests the proposition is correct.

To predict the energy of the ring systems is somewhat more challenging. There are no longer any stoppers but the rings curvature forces the separation of solitons to no longer be optimal. Hence it makes sense to try and model the energy as an infinite chain with a correction based upon the curvature of the ring.

$$E_{ring} = E_\infty + \delta(\kappa) \tag{2.4.15}$$

were κ is the curvature of the ring and the energies have been normalised by the Bogomolny bound. The curvature of the ring (as it is really a B-gon) can be easily calculated $\kappa = \frac{2}{l} \sin \frac{\pi}{B}$ where l is the separation of each vertex (soliton). Note that

$m = \sqrt{0.1}$		
B	E_{chain}	E_{ring}
1	1.5641	-
2	1.4678	-
3	1.4745	-
4	1.4645	1.4906
5	1.4645	1.4863
6	1.4620	1.4717
7	1.4613	1.4696
8	1.4603	1.4647
9	1.4598	1.4635
10	1.4592	1.4613
11	1.4589	1.4606
⋮	⋮	⋮
16	1.4576	1.4574
17	1.4574	1.4572
18	1.4572	1.4569
19	1.4571	1.4567
20	1.4570	1.4565
21	1.4568	1.4564

$m = 1$		
B	E_{chain}	E_{ring}
1	2.5702	-
2	2.4244	-
3	2.4333	-
4	2.4179	2.4695
5	2.4176	2.4185
6	2.4136	2.4363
7	2.4126	2.4185
8	2.4109	2.4226
9	2.4101	2.4163
10	2.4092	2.4157
11	2.4085	2.4125
⋮	⋮	⋮
18	2.4064	2.4067
19	2.4061	2.4057
20	2.4059	2.4059
21	2.4057	2.4051
22	2.4055	2.4053
23	2.4054	2.4047

Table 2.2: Energies for increasing charge for chains and rings for both $m = \sqrt{0.1}$ and $m = 1$. All the energy values are given normalised by the bogomolny bound $E/4\pi B$.

the separation is not necessarily the same as with straight chains (though it is fairly similar).

By inspection we can see that the ring solution energies appear to follow some inverse square relation, hence fitting the approximation $E_{ring} = E_\infty + \kappa^2 E_\kappa$ leads to the curves displayed in figure 2.5. The resulting values are $E_\infty = 1.4548$, $E_\kappa = 0.3247$ for $m = \sqrt{0.1}$ and $E_\infty = 2.40251$, $E_\kappa = 0.1615$ for $m = 1$. Unlike for the chain energies this isn't quite as accurate, though this may not be surprising as there seems to be larger fluctuations at lower charges between even and odd charge configurations.

2.4.2 Junctions

Another possibility of lowering the energy of a chain is introducing a junction. The reason single solitons attract is to reduce the change in the field, it is sensible to predict that the energy can then be reduced further by having more solitons in close proximity. We have already seen such a local solution in figure 2.3(e), however it has a higher energy than the chain solution. This may be due to having 3 as opposed to 2 stoppers, which has a large affect on low charge configurations. As we have calculated approximations for $E_{stopper}$ we can predict whether the various junctions do indeed lower the energy of the chain itself. We predict the normalised energy contribution of a junction to follow the following formula,

$$E_Y = E - BE_\infty - 3E_{stopper} \tag{2.4.16}$$

$$E_X = E - BE_\infty - 4E_{stopper} \tag{2.4.17}$$

where E is the total energy of the configuration normalised by 4π. $E_{Y/X}$ then gives the normalised energy difference in having a junction present. Note, there are three types of junction, depending on whether the centre soliton is charge 1, 2 or there is no linking soliton. We will consider having both 3 and 4 chains emanating from the centre for each type. The corresponding configurations are shown in figure 2.6.

When it comes to attempting to calculate the energy differences due to each

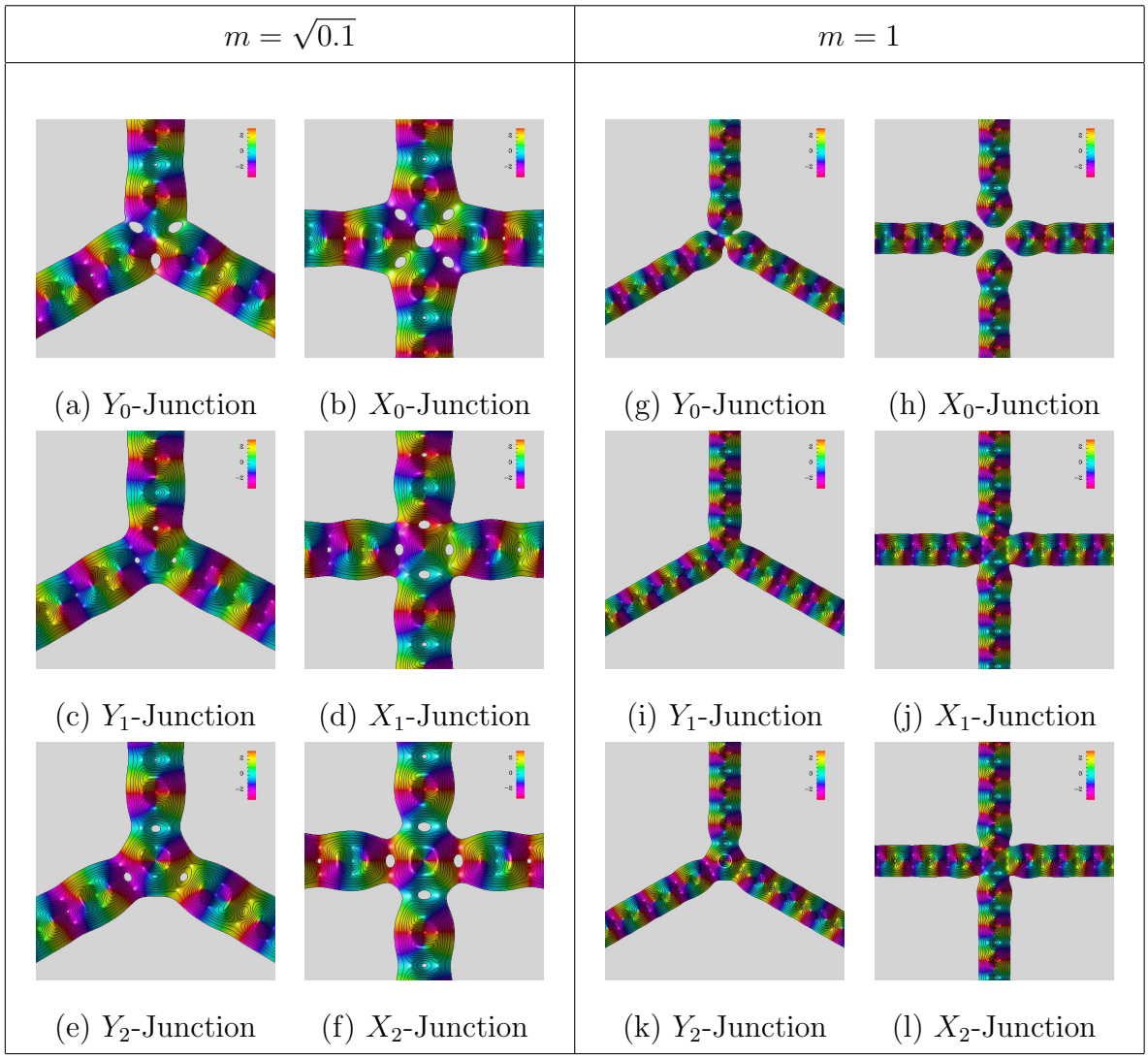

Figure 2.6: Energy density contour plots of X and Y junctions for charge 0, 1 and 2 centres. The junctions for $m = \sqrt{0.1}$ are shown on the left and $m = 1$ on the right. The plots are coloured by the phase $\theta \in [-\pi, \pi]$. Each plot is labelled by the type (X or Y) along with a subscript that gives the charge of the centre soliton.

junction we find that the emanating chains must be fairly long and the differences in energy are therefore small compared to the total energy. The accuracy used here made it challenging to gain a clear picture of what was happening. It would be useful to repeat the processes here using extremely accurate methods, so as to ascertain whether junctions have a positive or negative effect on the total energy. Alternately it would be useful to find a minimal energy solution for higher charge that exhibits these configurations. Finally we have also considered the simplest form for junctions to take, there could be some more complex form with more of a deformation to the emanating chains that lowers the energy further.

Even though junctions may not be energetically favourable they do appear as local minima. If a random configuration of single solitons is considered and an energy minimisation method applied, we find junctions forming of various lengths and type. Hence, it would appear that if we consider a large collection of baby Skyrmions, we should be able to model them as a network with various junctions.

2.4.3 Crystal Chunks

The final form for finite solutions we will consider, is taking a section of the infinite lattice and comparing the energy for increasing charge to the other solutions presented thus far. In reality we take an initial condition of charge 2 solitons placed at equivalent points with the same symmetry and flow the system to a minimal energy solution that is similar to a chunk of the infinite crystal lattice. It has previously been shown that a hexagonal lattice should produce the minimal energy [24] and thus this is the symmetry we will consider. We will present the results in the form of increasing hexagonal layers for some n-layer system. The numerical results for $n = 1 - 4$ are presented in figure 2.7, with the corresponding energies plotted in figure 2.8.

By inspection we can see that the form of the interior solitons are extremely similar to that of the full lattice, however the exterior solitons are slightly warped. It appears that the form of the warping depends upon the number of free (unbonded) sides of the fundamental hexagon the soliton resides in. Hence, we model the crystal chunk solution by assuming that each $B = 2$ soliton has 6 sides, matching the D_6

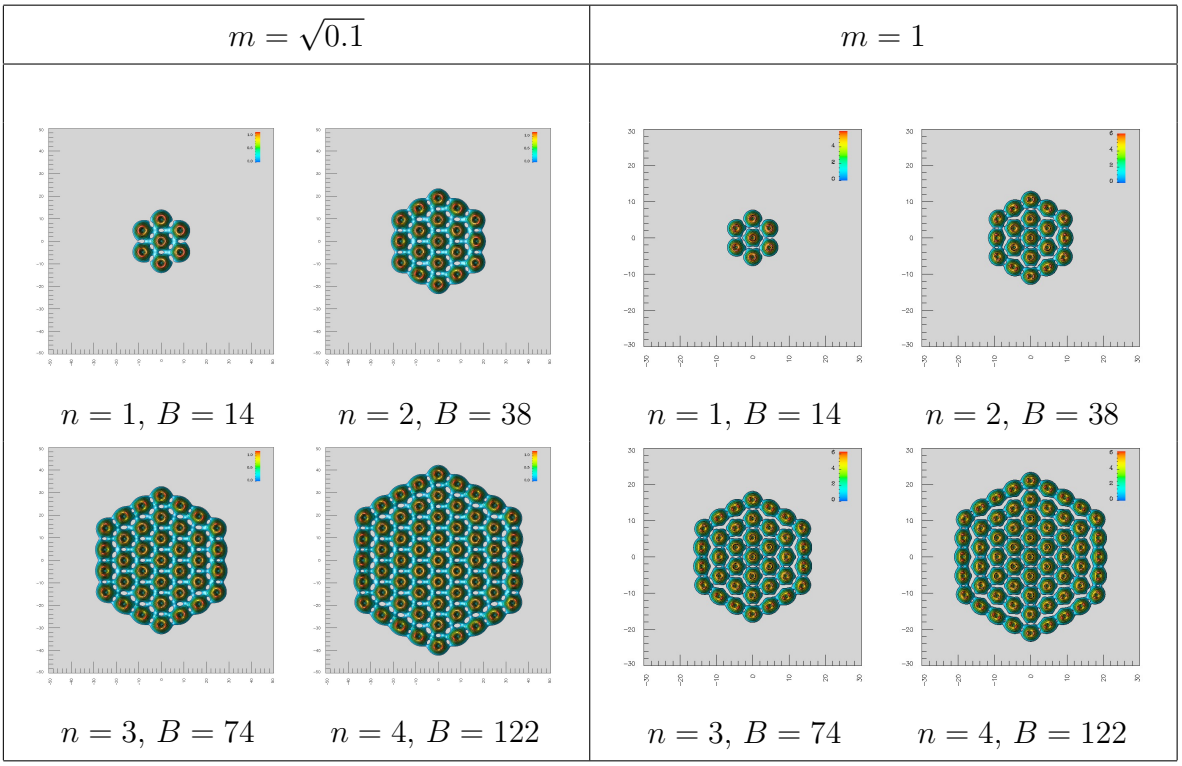

Figure 2.7: Energy density contour plots of crystal chunk solutions for both values of mass for increasing number of layers n. The corresponding energies are plotted in figure 2.8.

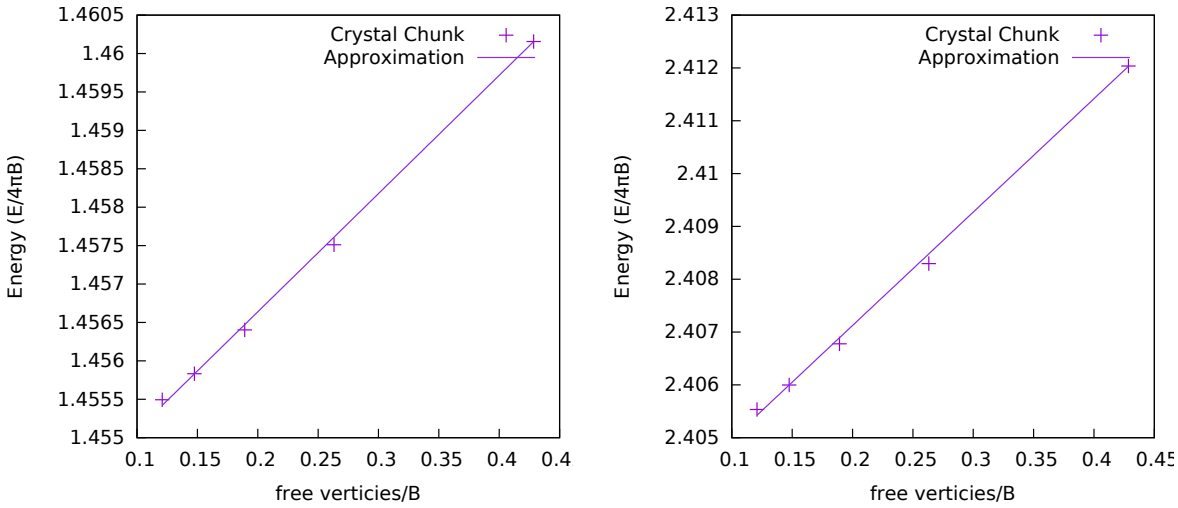

(a) $m = \sqrt{0.1}$ (b) $m = 1$

Figure 2.8: Plots of the normalised energy for crystal chunk solutions as they change with the number of free vertices. The energies are normalised by $4\pi B$. The best fit line was found using a least squares fit on the function $E_{crystal} + N_v E_{free}/B$, where N_v is the number of free vertices in a hexagonal lattice. The left plot is for $m = \sqrt{0.1}$ and the right $m = 1$.

symmetry for the interior points. We then suggest that the energy of the system depends upon the number of solitons as a whole, and the number of free sides. Hence to acquire the energy per charge we assume that the energy can be written as,

$$E_{chunk} = E_{crystal} + \frac{12n+6}{2(1+3n(n+1))} E_{free} \tag{2.4.18}$$

where the denominator gives the charge of the system and the numerator the number of free sides for each system. The energy $E_{crystal}$ is the energy of the infinite lattice with D_6 symmetry. We perform a least squared fit for this method, the results of which can be observed in figure 2.8. The fit seems reasonable, though the number of points is very small and at the lower end of the charge scale, where deviations tend to be greater. The least squares fit gives the values of $E_{crystal} = 1.4536$, $E_{free} = 0.01539$ for $m = \sqrt{0.1}$ and $E_{crystal} = 2.4028$, $E_{free} = 0.0215$ for $m = 1$. The values for $E_{crystal}$ are reasonably close to that found in the next section considering the inaccuracy of the method and number of points.

2.4.4 Global/Local Minima

Placing single solitons around the grid at random and performing an energy minimising flow will tend to give solutions formed of chains that consist of the following building blocks:

- Chains (Curved and Straight)
- Rings
- Y-Junctions
- X-Junctions
- Stoppers

It would appear that these types of simple solution form the basis of at least most of the reasonable energy solutions that occur. One may expect the Crystal Chunk solutions to appear, however they only have low energy for extremely high

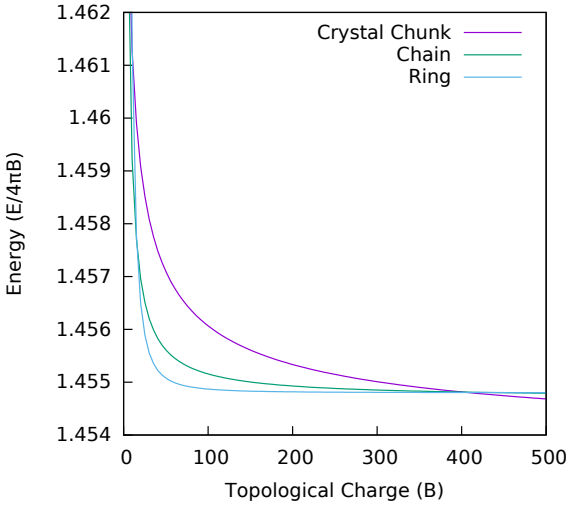

Figure 2.9: Plot showing the normalised energy for the three main type of solution as topological charge is increased for $m = \sqrt{0.1}$. The values were found by running the topological charge for the previously found approximations and parameters for each of the three types.

charges, hence we will consider baby Skyrmion networks and crystal chunks separately. Due to these simple building blocks we can predict the energy of most network configurations as,

$$E = \sum_{i=0}^{B} \left(E_\infty + \kappa^2 E_\kappa\right) + N_Y E_Y + N_X E_X + N_s E_{stopper} \tag{2.4.19}$$

As we have created approximations for each of the different types of simple solution, we can consider which will be the minimal energy solutions for various charges. Plotted in figure 2.9 we see the three main type of solutions for $m = \sqrt{0.1}$, the results for $m = 1$ are too inaccurate to be able to compare in a similar manner. This shows chains starting as the minimal energy solution, transitioning to rings and finally for very high charges, to crystal chunks. All that can really be taken from this plot is the extremely high charge required for crystal chunks to be the minimal energy solution. The results are not accurate enough to extrapolate any more detail.

Due to the work done on junctions in chains, we may find that between the ring and crystal chunk solutions, that more exotic solutions, involving rings and junctions

are in fact the minimal energy solutions. More work is needed to either rule these out or find some of these exotic forms.

These ideas should change the way we look at the baby Skyrme model for higher charges. Instead of simple straight chains the solutions seem to exhibit transitions at various charges (dependent on the parameters of the model). This is much more like the full 3-dimensional Skyrme model solutions.

2.5 Infinite Charge Configurations

In this section we discuss infinite charge solutions. In [23] the infinite charge straight chain is considered. We have already demonstrated that the straight chains are not optimal for higher charge solutions. As discussed in the previous section we can represent both chain and ring energies as deviations from the contribution from a single Skyrmion in an infinite chain. We then see that these deviations tend to zero as the topological charge of the configurations increase.

$$\lim_{B\to\infty} \kappa(B) = 0 \qquad \lim_{B\to\infty} \frac{BE_{lattice} + 2E_{stopper}}{B} = E_{lattice}. \tag{2.5.20}$$

Hence the infinite limit of rings and straight chains are equivalent. This has already been found in [23] however it was not found with enough accuracy to differentiate whether this or the traditional hexagonal lattice energies were lower for infinite charge configurations. We have therefore repeated the calculations with higher accuracy, which are displayed below. We have also performed the calculations for different masses.

2.5.1 Skyrmions on a Cylinder

To calculate the energy of an infinite chain we place a charge 2 configuration on a cylinder, parametrised as a rectangle periodic in the x-direction and $\lim_{|y|\to\infty} \boldsymbol{\phi} = (0, 0, 1)$. Due to the interaction energy given in (2.6.21) it is clear that the chain will form with relative phase for neighbouring solitons $\chi = \pi$. We then alternate the periodic length of the cell to find the minimal length and hence energy for an infinite

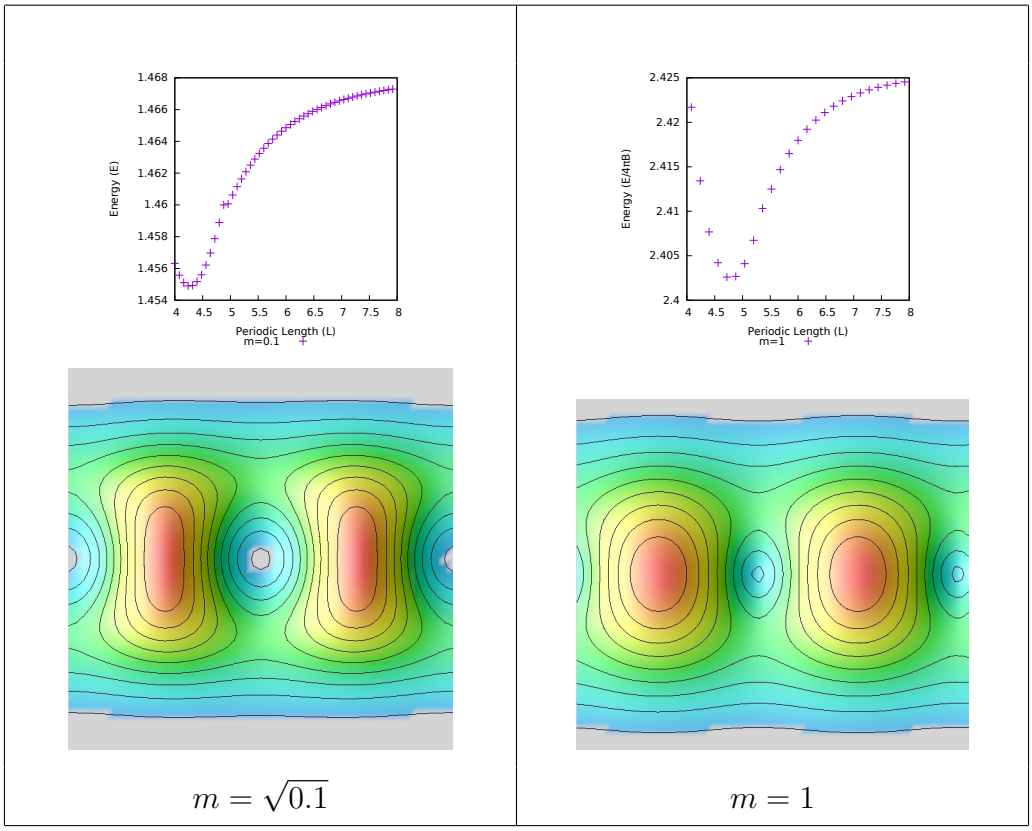

Figure 2.10: Results from simulating a $B = 2$ configuration on a cylinder of periodic length L for both $m = \sqrt{0.1}$ and $m = 1$. The top plots show the energy change as the periodic length L is varied. The bottom plot is an energy density contour plot of the fundamental cell, with periodic length L equal to the value that corresponds to the minimal energy.

chain, the plot demonstrating the changing energy against periodic length for both $m = \sqrt{0.1}$ and $m = 1$ is shown in figure 2.10. For $m = \sqrt{0.1}$ the minimal energy is found for $L = 8.56$, similar to [23] with the energy $E_{chain} = 1.4549$. For $m = 1$ the optimal periodic length was found to be $L = 4.76$ with an energy $E_{chain} = 2.4026$. The corresponding minimal energy configurations are also shown in figure 2.10 for both values of mass. Note that baby Skyrmions on a cylinder correspond to both the infinite straight chain and the infinite ring.

2.5.2 Hexagonal Lattice

The hexagonal lattice was proposed by [24]. We will use the fact that 8 hexagons perfectly tessellate a doubly periodic rectangle of sides $L \times \sqrt{3}L$. This means we model the baby Skyrmion on the physical space of a torus $\boldsymbol{\phi} : \mathbb{T}^2 \to S^2$ parametrised as a doubly periodic rectangle. We performed a similar process to above, alternating the value for L, however this time with two periodic directions.

If we follow [23] each hexagon contributes a $\frac{1}{2}$ charge, totalling $B = 4$. Performing the minimisation for this assumption we get the minimal length to be $L = 10.4$ with minimal energy $E_{lattice} = 1.4555$.

A more intuitive configuration can found by allowing each hexagon to contribute charge 2, totalling $B = 16$. Note that were the configuration suggested by [23] be the minimal configuration then we would mearly see the configuration repeated 4 times on a lattice of size $L \to 2L$ as the minimal energy. However what we observe is a slightly different energy, the results are presented in figure 2.11(b). We observe the minimal energy occurring at $L = 19.36$ with corresponding energy $E_{lattice} = 1.4541$. The corresponding minimal energy configuration, also shown in figure 2.11, demonstrates a clear hexagonal symmetry. This configuration also has a significantly lower energy than the form considered previously and thus suggests that the lattice solution is indeed lower in energy than the periodic chain solution presented above.

Finally we have performed the process for the hexagonal lattice with $m = 1$ shown in figure 2.11. Here we find the minimal energy to be $E_{lattice} = 2.4023$ corresponding to the cell length $L = 12.0$.

2.6 Dynamics

The dynamics of baby Skyrmions have been well studied for low charge interactions, they are presented here predominantly for comparison with the dynamics of alternate models later and hence we will not discuss them in detail. For an in depth discussion of low charge dynamics see [5, 25].

The interaction energy between two baby Skyrmions can be approximated by a

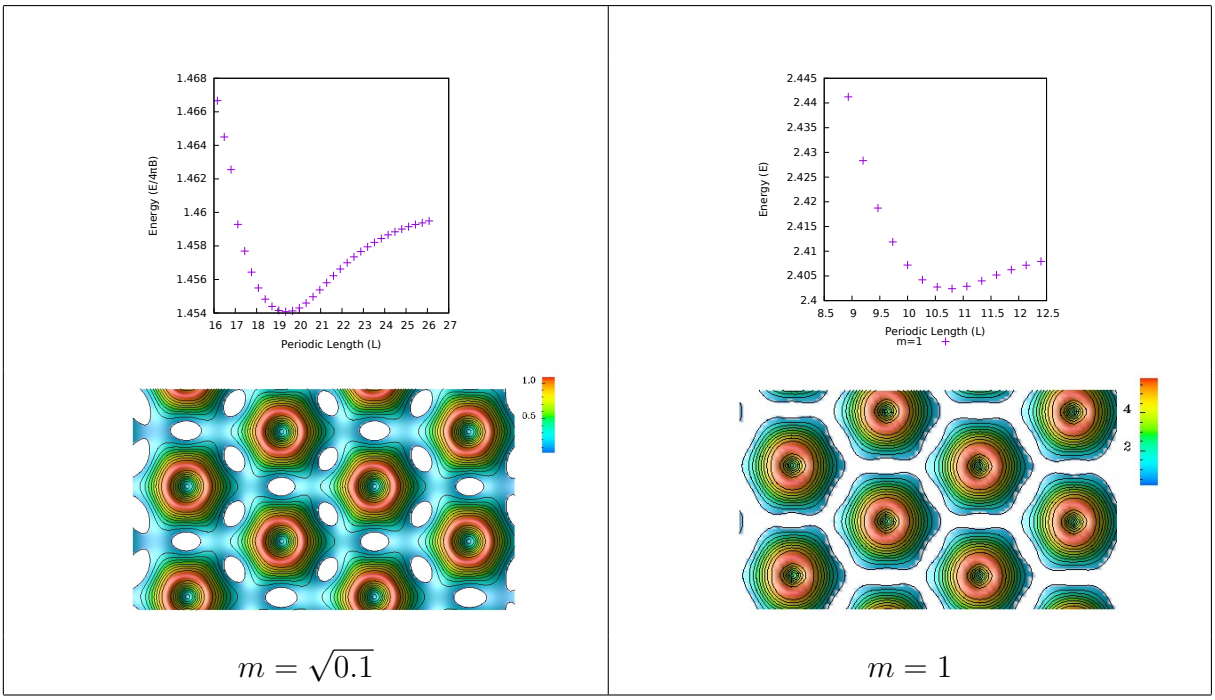

Figure 2.11: Results from simulating a $B = 16$ configuration on a rectangle with sides $L \times \sqrt{3}L$, allowing it to be tessellated by complete hexagons, for both $m = \sqrt{0.1}$ and $m = 1$. The top plot shows the energy for various values of L. The bottom plots show an energy density contour plot that corresponds to the minimal energy value of L.

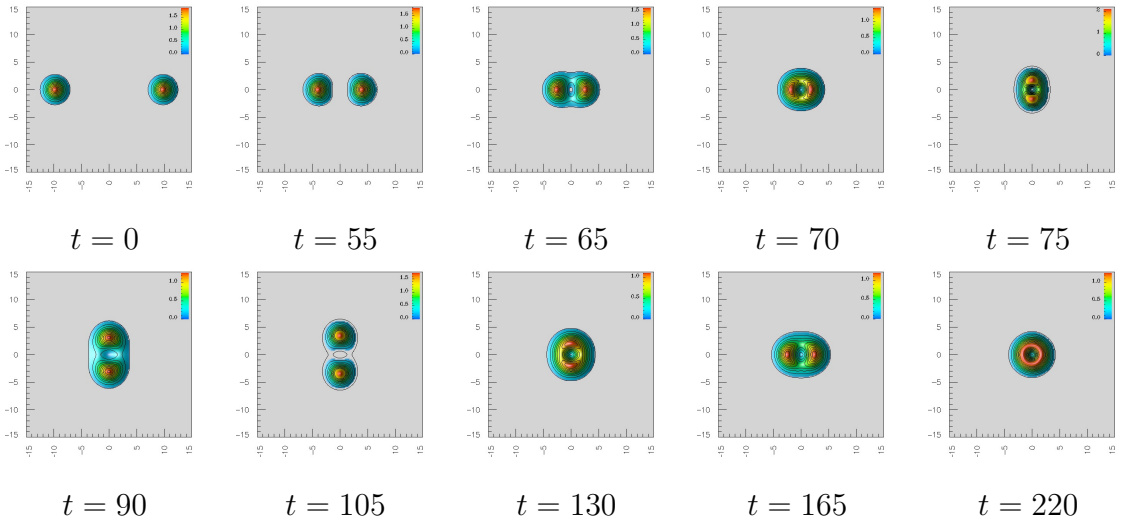

Figure 2.12: Scattering of two single solitons in the attractive channel, with initial velocities of $v = 0.2$. The solitons scatter at $\frac{\pi}{2}$, passing through the $B = 2$ radial solution. The solitons then attract and scatter in the same way again. This process continues with kinetic energy being emitted each time they coalesce, until they cannot overcome the attractive potential and form a $B = 2$ static solution.

dipole interaction,

$$U_\chi = \frac{p^2 m^2}{\pi} K_0 (mr) \cos(\chi), \tag{2.6.21}$$

where K_0 is the order zero modified Bessel function, p is a numerically found asymptotic decay constant, χ is the relative rotation and r the separation of the centres of the solitons ($\phi_3 = -1$). It is simple to see that the maximally attractive channel corresponds to U_π and the maximally repulsive channel to U_0.

The maximally attractive channel scattering of two single solitons is shown in figure 2.12. This exhibits the well known scattering by $\frac{\pi}{2}$. The two solitons attract and coalesce into a charge 2 radial solution. They are then emitted at an angle of $\frac{\pi}{2}$ from their initial trajectories. Much work has been done on the effect of impact parameters also [25]. What we are particularly interested in however, is the interactions of larger chain like solutions which have not been studied before.

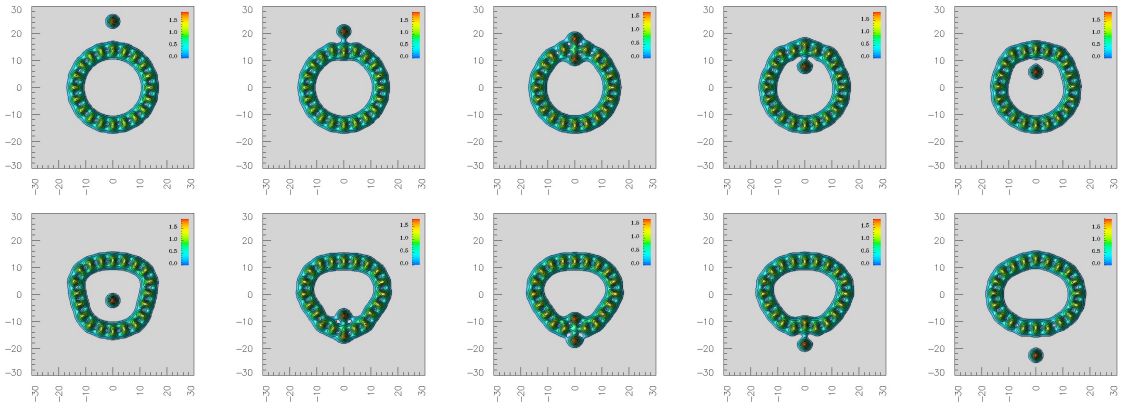

Figure 2.13: Scattering of a single soliton with a $B = 20$ ring solution, where the incident soliton is in the repulsive channel with the interaction point. The initial velocity is $v = 0.2$. The incident soliton replaces the one within the ring which then fires out doing the same with the soliton it meets.

2.6.1 Nuclear Interactions

We would like to consider the affect of fireing a single baby Skyrmion at a large atomic nucleus. We can consider this as a model of interacting a neutron or proton with a nucleus. We consider a stable $B = 20$ ring solution and a $B = 1$ Skyrmion with various velocities. The simulations were performed on a 1001x1001 grid with $dx = 0.1$.

If the soliton is in the repulsive channel with the soliton at the point of contact (and has enough energy) it will push the soliton out of the ring, taking its place in the ring. This soliton then interacts similarly with a soliton on the opposite side of the ring. This can be seen in figure 2.13.

Alternately, if the soliton is in the attractive channel with it's point of contact, it will be absorbed into the ring. The ring then propogates the energy from the collision around the ring, which allows the phase of each of the solitons to vary slightly so it can relax into the familiar minimal energy $B = 21$ configuration. This can be seen in figure 2.14.

Finally if the velocity is particularly high, it will split the ring. The incident soliton will rip the soliton it interacts with out of the ring, fireing the constituents out, bound together in multiple lower charge forms. This can be seen in figure 2.15.

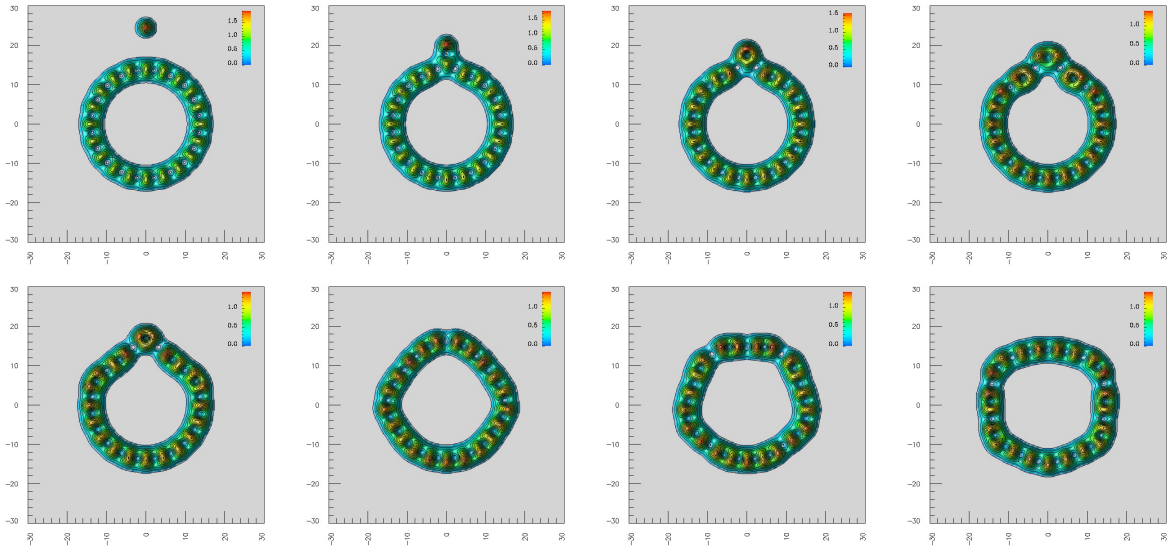

Figure 2.14: Scattering of a single soliton with a $B = 20$ ring solution, where the incident soliton is in the attractive channel with its interaction point. The initial velocity of the incident soliton is $v = 0.2$. The incident soliton coalesces with the soliton in the ring forming a $B = 2$ solution that then joins the ring, that must now correct the phases around the ring. The energy oscillates around the ring oscillating the relative phases between neighbours slightly, until they relax down to the correct configuration.

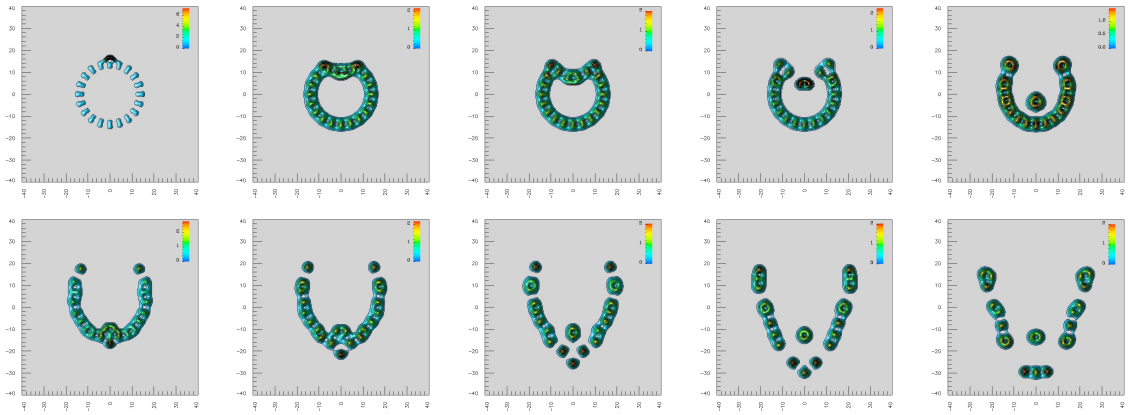

Figure 2.15: Scattering of a single soliton with a $B = 20$ ring solution, where the incident soliton is in the attractive channel with the interaction point and has a very high initial velocity of $v = 0.75$. The incident soliton rips the one it meets in the ring out from the chain, splitting it. It then charges into the ring again fireing the single soliton out as it isn't in the attractive channel. In the first image, the extremely high energy of the incident soliton compared to the static ring, increases the contour plot threshold.

2.6.2 Ring Interactions

Here we consider the interactions of multiple rings. We start by colliding two rings of charge $B = 20$ that have the same orientation, the results of which can be seen in figure 2.16. The rings repel each other, though given more time they will attempt to align themselves in phase. This is less interesting than the collision of the two rings that are in phase, shown in figure 2.17. Here the rings attempt to combine at multiple points forming two rings, one inside the other. These ultimately interact again and the final configuration is that of a large ring with two $B = 5$ chains emitted.

2.7 Conclusions

Firstly, we have shown that the suggestion that minimal energy soliton solutions take the form of increasing length straight chains is not the case and in fact the solutions to the baby Skyrme model are far more complex and intricate in nature.

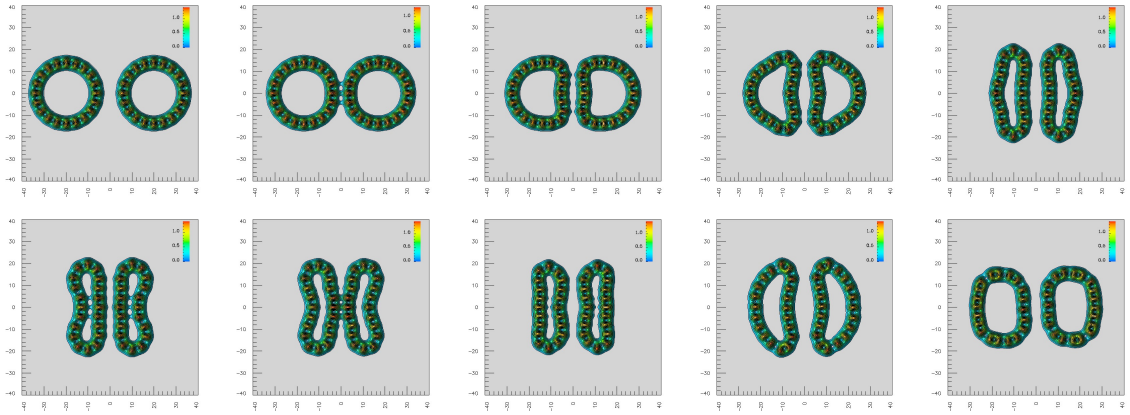

$t = 90$ $t = 105$ $t = 130$ $t = 165$ $t = 220$

Figure 2.16: Scattering of two $B = 20$ ring solutions in the repulsive channel and initial velocities of $v = 0.2$. The rings repel, bunching up and finally moving back out towards the boundary.

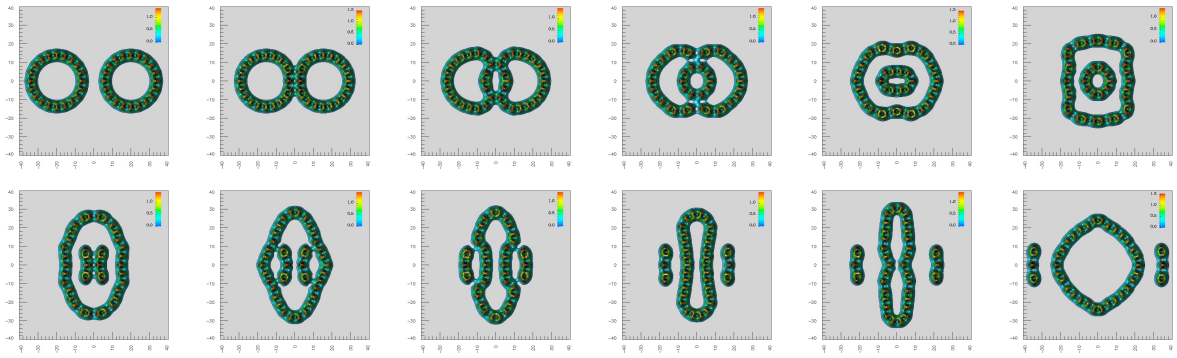

Figure 2.17: Scattering of two $B = 20$ rings in the attractive channel. They intersect at several points creating a multi-ring structure, that re-interacts to form one large ring, along with some emissions.

We have demonstrated that a number of transitions occur in the nature of the static solutions. Initially the form of static solution does indeed take that of chains of alternating phase baby Skyrmions. However this is quickly overtaken by linking the end of these chains to form rings of solitons with discrete symmetry D_B. The phases now alternate in various ways depending on if there is an even or odd number of solitons. Finally we showed the minimal energy solution becomes chunks of the crystal lattice solution, which appear to be mappable to a fundamental hexagon, contributing $B = 2$ to the total charge, with opposite sides identified.

We also suggested that the solutions between the ring solutions and crystal chunk solutions should produce more exotic results due to junctions that decrease the total energy of the system. While it is an intuitive transition to the crystal chunk solutions, it is unclear from the presented results if this is actually the case. Regardless to if they form minimal energy solutions, junctions are clearly prevalent in large charge complicated dynamical systems. It would be very interesting to find some approximating simulation for networks of baby Skyrmions, that could predict the nature of some of these higher charge networks and if they exists at all.

We presented some of the possible types for infinite charge solutions, showing that the method in [23] did not give the correct minimal energy crystal and that it is indeed the crystal that has a lower energy rather than the infinite chain solution.

Finally we considered the implications for ring solutions on the dynamics of various systems. Generally the systems we considered were quite simple but displayed some interesting behaviour. However, one particularly interesting feature of the existence of stable ring solutions is the possibility of modelling Spin-Orbit coupling. A toy model for the Skyrme model has been analytically studied, both classically and in its quantised form [26]. This was done by taking a 2-dimensional slice of a Skyrmion and modelling this using the interactions of uniform discs with some phase dependence. This is essentially the baby Skyrme model and hence the results could be applied to the ring solutions presented here.

Chapter 3

Baby Skyrmion Formation

3.1 Introduction

This chapter is taken from the first part of the paper [4] (with the remainder of the paper being included in part III). We simulate the collisions of domain walls in such a way as to form stable baby Skyrmion anti-baby Skyrmion pairs. Normally domain walls will annihilate, however if they interact in such a way as to produce the correct winding in the target space, then soliton anti-soliton pairs can be formed. In the $(2+1)$ model, this consists of the domain walls intersecting to form a ring, with the phase changing by some multiple of 2π around the ring.

There is a large amount of increased interest in how solitons can be formed, especially in the baby Skyrme model, due to it's proposal for use in spintronics and condensed matter memory systems [15, 16]. There is also interest in the interaction of large domain wall systems and Skyrmions.

3.2 The Model

The baby Skyrme model we consider in this section has an alternate mass term to the previous section which has previously been considered in [27],

$$V[\boldsymbol{\phi}] = \left(1 - \phi_3^2\right) \tag{3.2.1}$$

Due to our choice of potential there are now two choices of vacua denoted $\boldsymbol{\phi}_{\pm}$,

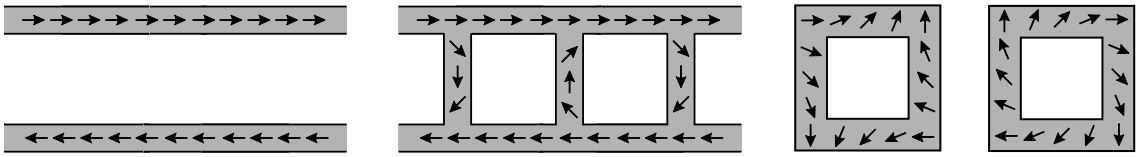

Figure 3.1: Annihilation of two domain walls by the formation of bridges, that interpolate the phase of the walls, forming in such a way as to produce a winding effect. With the correct winding, a soliton anti-soliton pair are formed

giving the boundary conditions for our physical space (due to finite energy requirements) to be,

$$\boldsymbol{\phi}_\infty = \lim_{|\boldsymbol{x}|\to\infty} \boldsymbol{\phi}(\boldsymbol{x},t) = \boldsymbol{\phi}_\pm = (0,0,\pm 1)\,. \tag{3.2.2}$$

The inclusion of this mass term breaks the $O(3)$ symmetry to $O(2)\times\mathbb{Z}_2$, the selection of a vacua on the boundary of the physical space then breaks the symmetry further to an $O(2)$ symmetry. This new mass term has been selected as there needs to be at least two choices of distinct discontinuous vacua to allow domain walls to form. In fact for the purposes of baby Skyrmion formation, it is optimal for these disconnected vacua to lie on antipodal points of the target S^2 space.

Domain walls were introduced in part 1 as the 2 dimensional extension to the kinks considered previously. The walls interpolate from the two possible vacua $\boldsymbol{\phi}_\pm$. Normally they have no topological charge in and of themselves, however special domain wall solutions have been found that do contain winding [28,29]. This winding is given stability due to the constraining domain wall.

It has been suggested that baby Skyrmion solutions can be formed from domain wall collisions [30]. If the domain walls collide in such a way as to form channels between them, with the correct winding round the loops formed, then baby Skyrmion anti-Skyrmion pairs can be formed, as shown in figure 3.1. Note that this doesn't break topological charge invariance, as a soliton anti-soliton pair has been formed.

If we consider the process in terms of the target space, the domain walls traverse between the two antipodal vacua of the target S^2. The domain walls intersect at points along their length. To achieve this, a bridge must form that sweeps around

the target sphere to match the field configuration of the opposite domain wall. The bridge essentially has a choice, it can sweep one of two ways around the target space. If two bridges form adjacent to each other, that wind round the target space in the opposite direction, then when they coalesce, a loop has formed that winds round the target space once.

While this has formed a baby Skyrmion or anti-Skyrmion (depending on which way round the bridges formed), topological charge invariance will not be broken. This is due to domain walls being infinitely long or forming in loops, which segment areas of space into different vacua. If we return to the example presented before where the domain walls meet and form only two bridges, which wind correctly. We can consider these bridges as physical objects that propagate along the walls in both directions. If the walls are infinitely long then the bridges will meet opposite bridges on both sides forming a soliton anti-soliton pair. Hence a chain of soliton anti-soliton pairs can form. If the domain walls are loops, then the bridges will meet at the initial interaction point, however they will then propagate around the walls and meet again to produce the opposite winding.

3.3 Baby Skyrmion Formation Examples

Simulations of the nonlinear time-dependent PDE that follow from the variation of (2.2.1) were performed using a fourth order Runge-Kutta method, on a grid of 501x501 grid points, with 4^{th} order finite difference derivatives. We used Neumann boundary conditions (the spatial derivative normal to the boundary vanishes), which allows the domain walls to move unhindered. In theory the domain walls are infinitely long (or formed from systems of domain wall loops), however in any simulation or experimental system we deal with a finite segment.

We first simulate the process outlined in figure 3.1, however this requires our initial conditions to be highly constrained. Domain walls by their nature want to minimise their length (become straight in $\mathbb{R}^2$). They also want to match the phase of any other incident walls. One can see the production process of a soliton anti-soliton pair from two domain walls in figure 3.2. If the phases are correctly wound, then

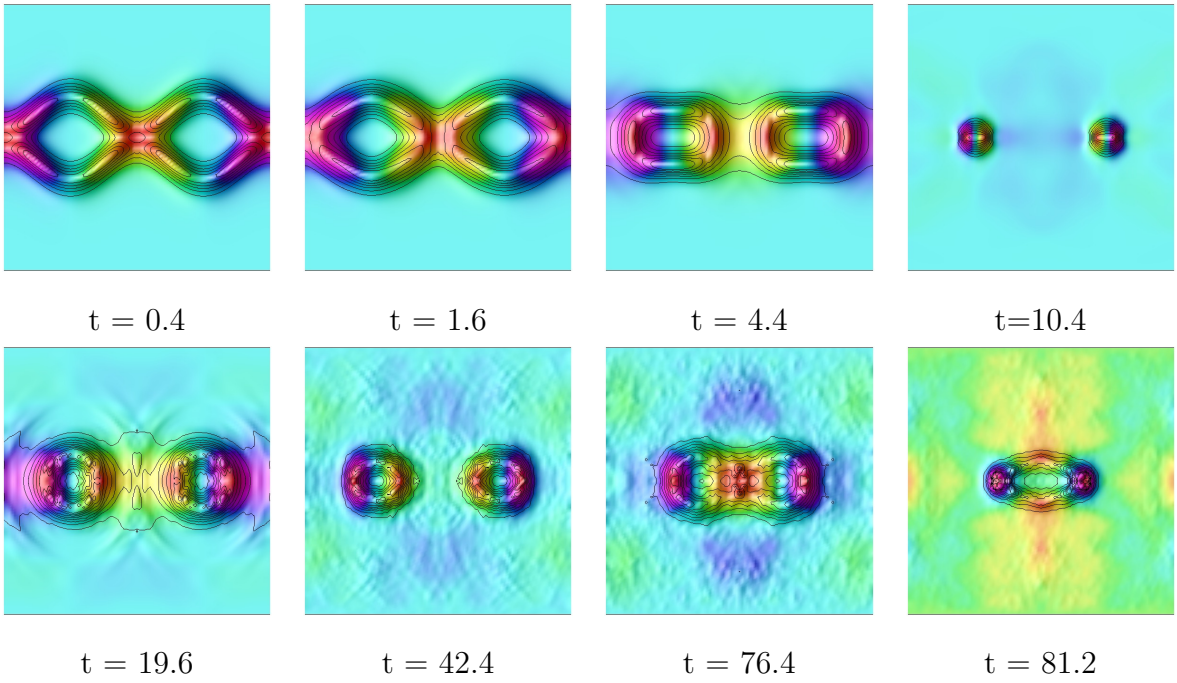

Figure 3.2: An energy density contour plot of 2 domain walls that have been perturbed to simulate the forming of bridges. The bridges are oriented to cause the fields to wind correctly to form a soliton anti-soliton pair. The two solitons initially reduce in size then they attract and annihilate. Due to the large quantities of energy involved, the solitons oscillate in size while attracting, until they ultimately annihilate. The plot is coloured by the value of the ϕ_1 field.

the pair forms and ultimately annihilates. In this simulation we have perturbed two standard straight domain walls to simulate bridges forming and winding the phases round. However this doesn't naturally happen in a simulation, as the walls will normally collide across their length, having equalised their phases across the length of the walls. It is possible that this could occur in a domain wall network, where there are more interactions occurring with other domain walls in the system. It is likely the walls could then meet on a scale far larger than the size of a Skyrmion and hence the bridges formed would not affect each other initially, allowing opposite directions around the target space to be selected.

To produce a production process in which we don't have to heavily constrain the initial conditions, we have to add an additional domain wall. The formation process for a single soliton can be seen for 3 domain walls in figure 3.3 and for 4

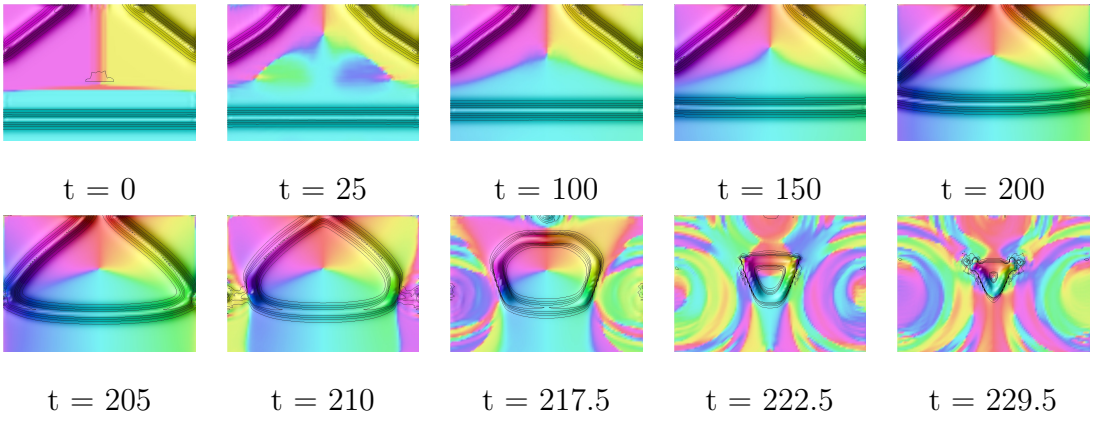

Figure 3.3: Energy density plot for three incident domain walls with different phases. The walls attract, attempting to equalise their phases on both sides. This leads to the correct winding for a soliton, once the walls have interacted. The plot is coloured by the phase $\theta = \tan^{-1}\frac{\phi_2}{\phi_1}$.

domain walls in figure 3.5. Note that we are now only considering the part that forms the soliton, not the matching anti-soliton that should be formed further down the domain wall interaction.

We observe that the domain walls will try to match their phase with the domain walls on either side of them, causing the phase to partially wind along the length of the wall. Should the phases of each incident domain wall be well separated, then the winding around all the domain walls will produce a single charge soliton, as the walls annihilate with each other.

The large amount of kinetic energy makes keeping the resulting soliton stable quite challenging, hence the process was repeated with high damping, resulting in figure 3.4. Here the resulting soliton remains constant and the topological charge has also been plotted showing an increase from $B = 0$ to $B = 1$. One can see that this has occurred due to a discontinuous deformation made to the system, moving the domain wall away from the boundary of the space. This requires damping to counteract this but allows the topological charge to be artificially changed.

In figure 3.5 one can observe a single soliton being formed by 4 domain walls in a similar manner. If the incident phases in the 4 wall case wind round the target space twice it should be possible to form a charge 2 soliton instead of a charge 1. However

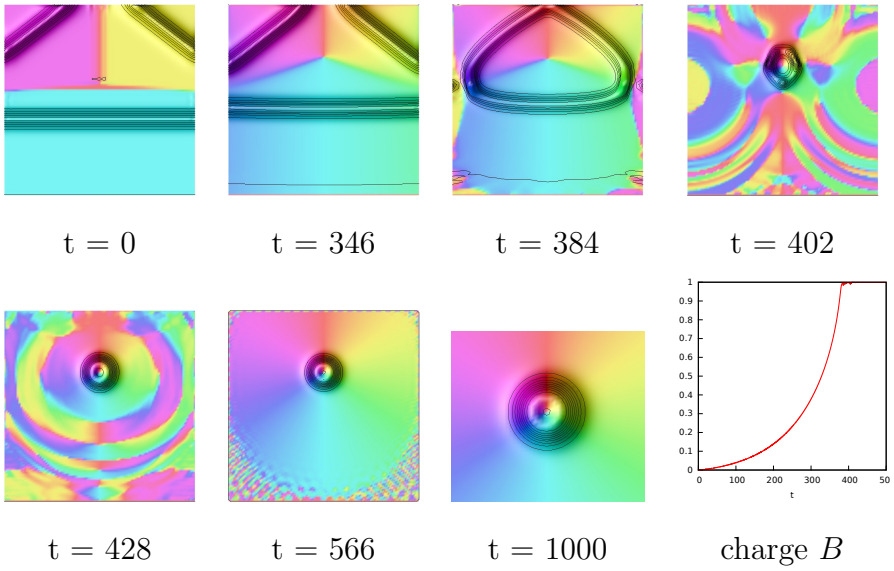

Figure 3.4: Energy density plot of three incident domain walls with different phases and heavy damping. They match phases and create the correct winding. The penultimate panel shows a blown up image of the resulting baby Skyrmion and the final panel is the changing topological charge over time.

it requires the same stringent initial conditions as with the 2 domain walls forming a single soliton in figure 3.2. Alternatively a large scale would be required to ensure the bridges don't interact before they have chosen a route round the target space. However if one considers the meeting of 5 domain walls, then the winding can be easily created for a charge 2 soliton. This result should continue for higher numbers of incident domain walls, assuming the phases are distributed in the correct manner.

This leads us to conclude that multiple interacting domain walls have a higher chance to produce a baby Skyrmion, rather than the highly constrained requirements of two domain walls annihilating. This idea can be put into practice in a condensed matter system. Here the formation of baby Skyrmions at will is of great interest. If three domain walls were to meet at a bifurcation point (Y-junction) in a system, then the chances of producing a stable soliton would be quite high. The difficulty would arise in having phases that are well separated. This can be achieved by considering a theory that promotes certain phases for domain walls. To achieve this a mass term can be used that breaks the traditional $O(2)$ symmetry of the theory to some dihedral group. Such a potential has been studied in [1, 31] (shown in 3.3.3) that

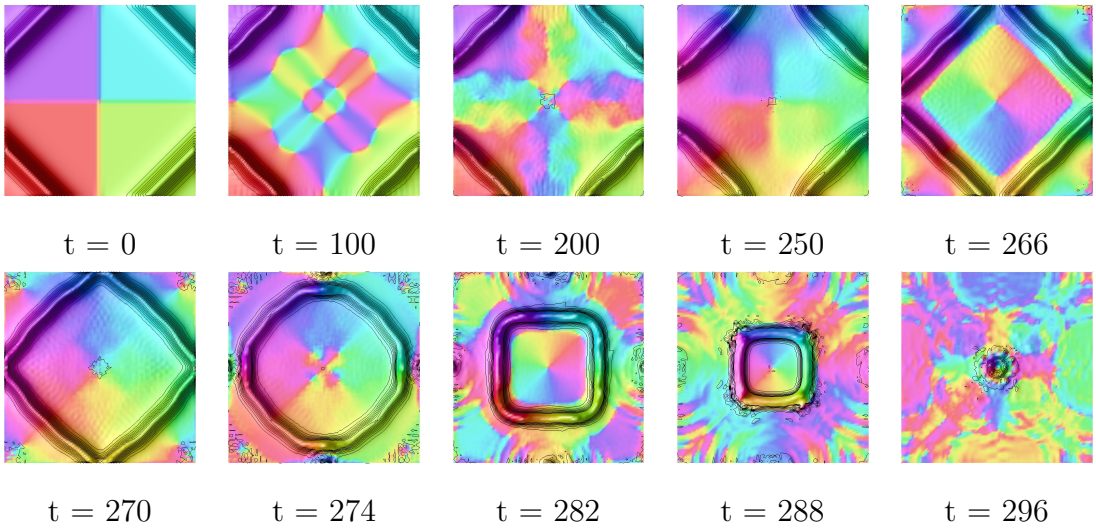

Figure 3.5: Energy density plot of four incident domain walls with different phases. They match phases and create the correct winding. This could create a charge 2 solution if two adjacent wall phases were swapped, due to the field needing to wind twice. It is likely a larger scale is needed for this to occur however. The plot is coloured by the phase $\theta = \tan^{-1}\frac{\phi_2}{\phi_1}$.

breaks the symmetry to a D_N subgroup. By this we mean the dihedral symmetry group containing the symmetries of a standard N-gon. A sensible choice would be to set N equal to the number of incident walls, ensuring their phases are well separated.

$$V[\boldsymbol{\phi}] = \left|1 - (\phi_1 + i\phi_2)^N\right|^2 (1 - \phi_3). \tag{3.3.3}$$

This term has the correct D_N symmetry however there is a subtlety in that it creates new possible vacua, that are no longer antipodal. Hence domain walls can now form at the N points on the equator of the target space where $(\phi_1 + i\phi_2)^N = 1$.

For the optimal potential we must remove these vacua while keeping the dihedral symmetry and add two antipodal vacua, which is quite simple mathematically,

$$V[\boldsymbol{\phi}] = \left|\alpha - (\phi_1 + i\phi_2)^N\right|^2 (1 - \phi_3^2) \tag{3.3.4}$$

where $\alpha \gg 1$. In practice this potential seems somewhat artificial, though it serves the purpose of demonstrating how a system should be constrained, to allow

increased production of the correct winding to form baby Skyrmions.

3.4 Domain Wall Systems

One system in which a baby Skyrmion can be formed is a system of interacting domain walls. This consists of vacua separated by domain walls in loops, that want to annihilate to reduce the energy of the system. We will consider simple interactions, that may occur between loops of domain walls, in such a way as to create baby Skyrmions. Note that as we are no longer considering infinite objects, the energy of the system is now finite. It also allows us to set the boundary of our system to be the same value ϕ_+, and Neumann boundary conditions are no longer required.

A single interaction has been drawn in figure 3.6, showing how two loops, if they form bridges, can produce a temporary local topological charge density. Note that it may seem again that we have broken topological charge invariance, however the produced Skryrmion winding is counteracted by the winding of the domain wall surrounding it, which winds in the opposite direction. This may not be obvious at first, as the phase winds in the same direction for both objects. However, the surrounding domain wall interpolates ϕ_3 in the opposite direction, hence producing negative winding to the baby Skyrmion in the centre.

The numerical simulation of 2 domain wall loops interacting can be seen in figure 3.7. The numerics here have a high damping term to ensure the baby Skyrmion is stable and to prevent the domain wall loops collapsing quickly. Note that while a large system is considered here, one may expect domain wall systems to be of an order much larger than the size of a single baby Skyrmion. The local charge density is created in the centre of the resulting domain loop, however the charge of the entire system remains zero. The domain wall then collapses in on the baby Skyrmion, ultimately annihilating.

A less constrained case is modelled with 3 domain wall bubbles meeting at various points in figure 3.8 (here quite symmetrically, though this is merely a product of minimising the size of the grid used). This time 3 bridges are formed, these meet

and form a baby Skyrmion at the centre of the system. The bridges create a partial winding on the surrounding domain wall loop that spread out. Ultimately the domain wall loop shrinks and annihilates with the interior baby Skyrmion. The values for ϕ_3 are also shown in figure 3.9 to demonstrate the vacua structure at various times of the simulation.

The final simulation, seen in figure 3.10 demonstrates 4 bubbles meeting to form a soliton and anti-soltion. The fractional windings annihilate around the surrounding domain wall loops. The soliton and anti-soliton are well separated hence don't annihilate. The domain wall boundary collapses in absorbing the solitons into the wall. The windings then annihilate around the domain wall boundary as it collapses.

These simulations represent what may happen at the meeting of two domain wall bubbles. It is also possible that bubbles may meet in several places forming chains of Skyrmion anti-Skyrmion pairs, as with the examples in the previous section. This means in a large system of domain walls one would find a complicated system of local charge distributions, within some walls which have sections of fractional winding, that effectively shield the exterior space from observing any change in topological charge.

It would be interesting to consider whether the interior system and interactions could be represented by what occurs on the boundary in some way. It would also be interesting to consider how the fractional winding sections interact with each other when traversing the domain wall.

3.5 Conclusions

We have demonstrated several situations in which Skyrmion solutions can be produced by domain wall interactions in the $(2+1)$-dimensional baby Skyrme model. We also demonstrated that using more than 2 domain walls, decreases the required constraints on the system for formation to occur. It is possible that these techniques could be utilised in condensed matter systems to produce Skyrmions. We have also modelled the interactions of domain wall networks, demonstrating how baby Skyrmions can be formed within these. It was shown that for the topological

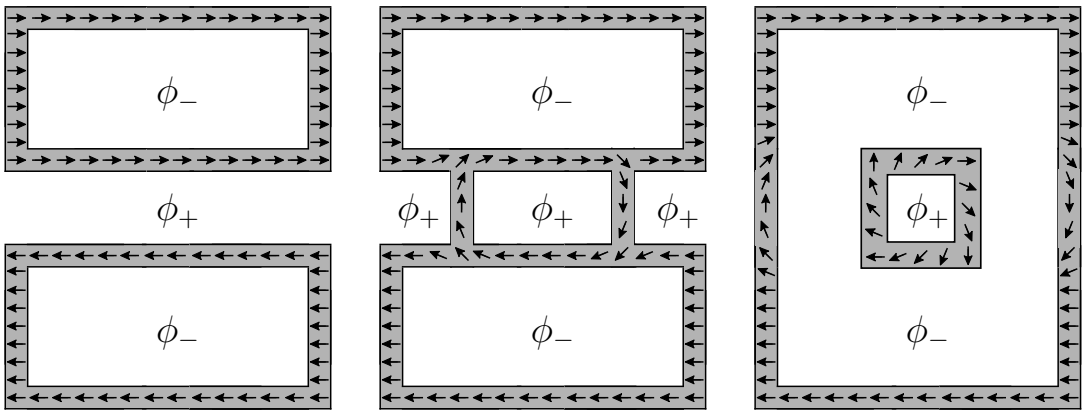

Figure 3.6: Annihilation of two domain wall bubbles. Bridges form, interpolating between the phase of the two domain walls that wind correctly to form a Skyrmion. As the bridges annihilate a Skyrmion forms and some fractional winding is created on either side of the boundary domain wall. The fractional winding sections on the domain wall cancel the winding of the Skyrmion as the domain wall interpolates ϕ_3 in the opposite direction to the interior Skyrmion. The various vacua regions the domain walls interpolate between are denoted $\phi_\pm$.

charge to remain conserved, a counteracting winding was formed along the boundary of the system.

This chapter has raised a few interesting questions that have gone unanswered here. Firstly, how feasible would this method be for forming Skyrmions in a condensed matter system at a bifurcation point (Y-junction). Also, could a condensed matter system be used to give the D_N symmetry to the incident domain walls, to increase the probability of formation to occur. Secondly, does the counteracting winding on the boundary of a domain wall system, allow any information regarding the interior winding to be attained. To understand this we are likely to need to understand the nature of interactions of the bridges, or fractional winding segments that propagate around the boundary. Finally it would be interesting to be able to make some statistical predictions on the formations of Skyrmions in a large domain wall network. This may also be able to be related to the excitation of a vacuum state of a system, to see if Skyrmions could be formed this way, in a non-perturbative manner.

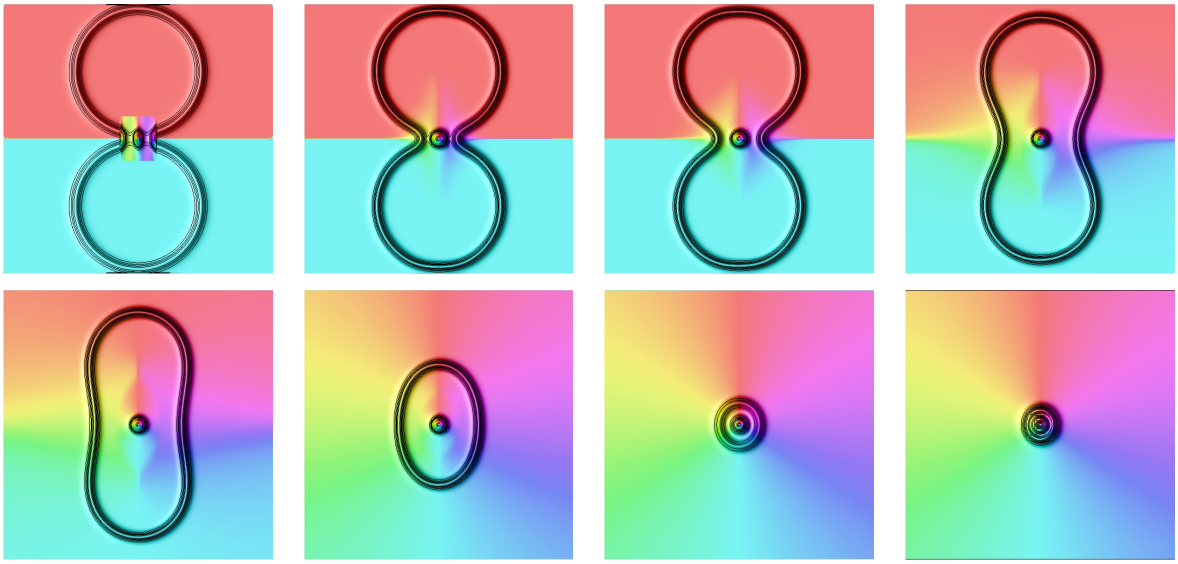

Figure 3.7: Energy density plot of two domain wall bubbles meeting and forming a local winding and a baby Skyrmion. The wall has two points of fractional winding that cancel the interior baby Skyrmion. The fractional windings spread as the wall contracts ultimately annihilating with the interior baby Skyrmion. The initial conditions are highly constrained to produce the correct winding. The plot is coloured by the phase $\theta = \tan^{-1}\frac{\phi_2}{\phi_1}$.

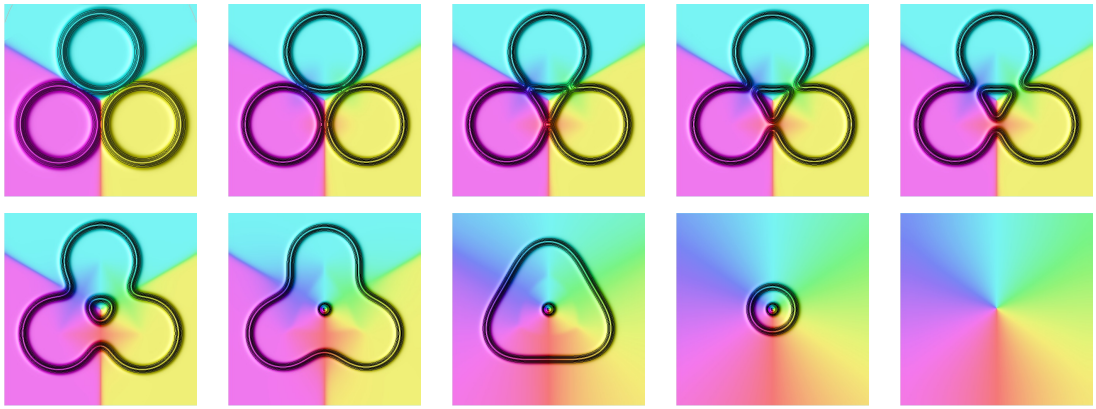

Figure 3.8: Energy density plot of three domain wall bubbles meeting and forming a local winding and a baby Skyrmion. The boundary then has three points of fractional winding that cancel the interior baby Skyrmion. The fractional windings spread as the wall contracts ultimately annihilating with the interior baby Skyrmion to the vacuum. The plot is coloured by the phase $\theta = \tan^{-1}\frac{\phi_2}{\phi_1}$.

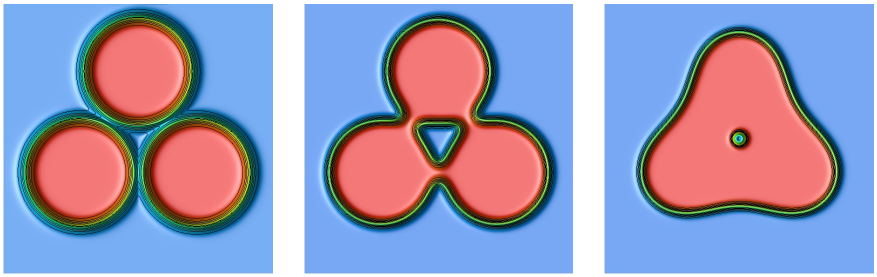

Figure 3.9: Energy density plot of three domain wall bubbles meeting and forming a local winding and a baby Skyrmion. It is coloured by the ϕ_3 value to show the vacua structure of the system at various constant time slices. The plots correspond with the simulation in figure 3.8.

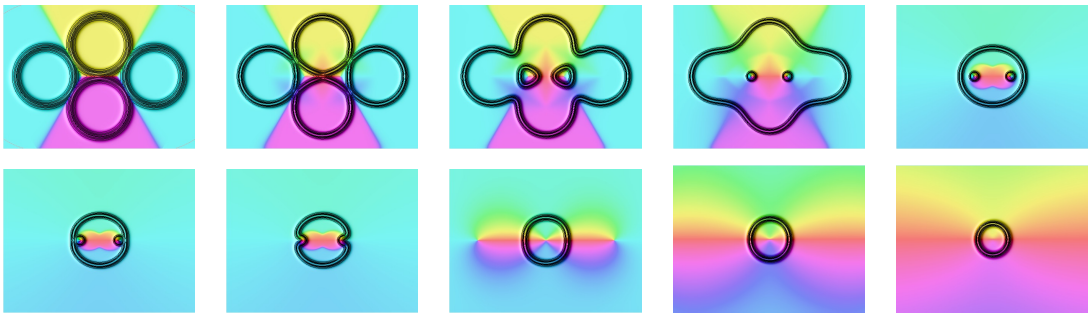

Figure 3.10: Energy density plot of four domain wall bubbles interacting to form a soliton and anti-soliton. The boundary has no resulting winding as the local charge of the soliton anti-soliton pair cancel. The two solitons are absorbed into the wall, with their winding then subsequently annihilating round the wall. The plot is coloured by the phase $\theta = \tan^{-1}\frac{\phi_2}{\phi_1}$.

Chapter 4

Broken Baby Skyrmions

4.1 Introduction

This section is based upon the work published in the paper [1], which seeks to correct the issue that the Skyrme model or baby Skyrme model exhibits no classical colour dependence, despite being seen as models of QCD. The number of colours, N, appears only when the models are quantised (as a coefficient of the Wess-Zumino-Witten term). In this chapter we are interested in a model that has a classical colour dependence, which has been proposed by Jäykkä *et al.* [31]. For the resulting solitons of the three-colour theory, it was found that the energy density was arranged in lumps, called partons. Links were also identified between the structure of the higher charge solitons and polyiamonds. This paper left interesting open questions as to how this would generalise for systems with a greater number of colours.

In this paper we consider this planar Skyrme model with discrete symmetry, and examine static soliton field configurations for a range of N-colour systems. By examining the structure of the static solutions, we consider how the connection to polyiamonds generalises for higher-colour systems to polyforms. Finally we go on to consider the dynamics of these solitons and ascertain whether their structure impacts upon the scattering behaviour.

4.2 The Model

In this paper we consider the potential

$$V[\boldsymbol{\phi}] = \left|1 - (\phi_1 + i\phi_2)^N\right|^2 (1 - \phi_3), \tag{4.2.1}$$

for some integer $N \geq 2$, which was considered for the $N = 3$ case by Jäkkä *et al.* [31]. Note that up to quadratic order in ϕ_1 and ϕ_2 this reduces to the pion mass potential. Hence physically the fields ϕ_1 and ϕ_2 are massive fields with mass given by the constant m, as with the standard potential. This choice of potential breaks the $O(3)$ symmetry of the system to the dihedral group D_N, generated by rotation $(\phi_1 + i\phi_2) \to (\phi_1 + i\phi_2)e^{2\pi i/N}$ and reflection $\phi_2 \to -\phi_2$. This choice of potential has vacua at $\boldsymbol{\phi} = (0, 0, 1)$ and at the Nth roots of unity on the $\phi_3 = 0$ equatorial circle. The vacuum at spatial infinity is chosen to be

$$\boldsymbol{\phi}_\infty = \lim_{|\mathbf{x}|\to\infty} \boldsymbol{\phi}(\mathbf{x}, t) = (0, 0, 1). \tag{4.2.2}$$

This choice does not further restrict the symmetry of the model since the generators of the dihedral group are independent of ϕ_3. We will follow the notation of paper [31] and hence refer, somewhat suggestively, to the system for a particular choice of N as the N-colour system.

4.3 Static Planar Skyrmions

In this section we specialise to the static case and examine the structure of (local) minimal energy solutions. The only work to date is for the three-colour system [31]. We shall recreate and then extend these findings, as well as examining the static solutions for higher-colour systems.

To find these soliton solutions we use an energy-minimising gradient flow algorithm, choosing to set $\kappa = m = 1$ on a square grid with $(501)^2$ grid points and lattice spacing $\Delta x = 0.04$. Spatial derivatives are approximated using fourth-order finite difference methods. We also fixed the boundary of our grid to be the vacuum at spatial infinity $\boldsymbol{\phi}_\infty = (0, 0, 1)$. For all our simulations the topological charge, when computed numerically, gives an integer value to five significant figures, indicating the accuracy of the results.

The gradient-flow algorithm requires an initial approximation to the static soliton. Consider the field configuration

$$\boldsymbol{\phi} = (\sin(f)\cos(B\theta), \sin(f)\sin(B\theta), \cos(f)), \tag{4.3.3}$$

for polar coordinates r and θ, and where f is a monotonically decreasing function of r. The boundary conditions on f are $f(0) = \pi$ and $f(R) = 0$, where the circle of radius $r = R$ lies inside the grid. Outside this radius the rest of the grid is set to the vacuum ϕ_∞. We can see that this describes a field on the grid with topological charge B, and so for a suitable choice of f this gives us our initial approximation.

We note that this initial approximation has the maximal symmetry D_{NB}, in the sense that the spatial rotation $\theta \to \theta + 2\pi/NB$ can be compensated for by global rotation symmetry, while the reflection $\theta \to -\theta$ can be balanced by a global reflection.

To find solutions with lower symmetry we also considered similar initial conditions but with a symmetry breaking perturbation. Once a pattern was discernible for these lower symmetry forms, we also used a product ansatz for our initial conditions. In other words we placed single solitons about our grid and then performed our gradient flow procedure.

4.3.1 Single Soliton Solutions

Applying our energy minimizing code on the initial conditions in equation (4.3.3) for $N = 3, 4$ and 5, and $B = 1$, we obtain the contour plots in the top half of figure 4.1 (note that all images in this section show the entire grid and hence are to scale). These energy density plots exhibit the maximal symmetry group D_N, giving the predicted N parton structure. Note that a plot of topological charge density will yield a similar result. The energy is given to be $E = 34.79, 34.58$ and 34.41 respectively.

We can further embellish the parton interpretation by introducing colour into our visualisation. Each peak of the energy density will have an associated colour, derived from the segment of the target 2-sphere in which the parton lies. These segments are formed by taking the angle in the ϕ_1, ϕ_2 plane (phase), and splitting

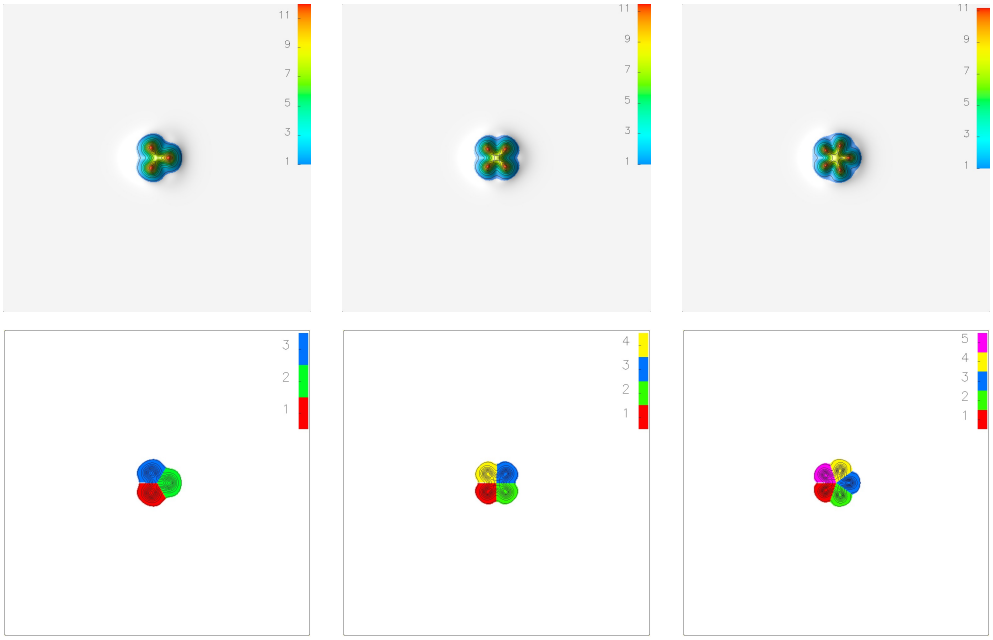

(a) $N = 3$, $B = 1$ (b) $N = 4$, $B = 1$ (c) $N = 5$, $B = 1$

Figure 4.1: Energy density plots of the single soliton solutions for a)$N = 3$, b)$N = 4$ and c)$N = 5$. The top image is coloured based on the energy density and the bottom image is coloured based on the segment in which the point lies in the target space.

the plane into N segments using the phases of the N vacua on the $\phi_3 = 0$ equator.

Each of these segments, or partons, contributes $1/N$ to the topological charge. Naturally this means that the combination of the vacua structure and the requirement of integer topological charge, forces these partons to be topologically confined. If we add this additional structure to our figures, we obtain the results given in the lower half of figure 4.1.

4.3.2 Multi-soliton Solutions

For higher values of topological charge, we observe two prominent types of solution. These are shown in figure 4.2 for $N = 3$, figure 4.3 for $N = 4$ and in the appendices for $N = 5, 6$. The maximal symmetry solutions, shown in figures 4.2(a,c,e) and 4.3(a,b,e), are composed of NB partons, situated on the vertices of a regular NB-gon. They retain the maximal symmetry of the initial conditions, namely D_{NB}. The $B > 2$ maximally symmetric solutions have energies higher than that of the

lower symmetry solutions, forming local minima. However for $B \geq 5$ the maximally symmetric solution could not be found.

For $B = 2$ the hexagonal $N = 3$ solution (4.2(b)) has an energy comparable with the lower symmetry solution (4.2(a)). Due to our expected numerical accuracy, we cannot determine which of the solutions is the global minimum of our model. However for all $N > 3$, the lower symmetry solution appears to be an unstable saddle point and could not be attained via gradient flow. Hence the maximal D_{2N} solution is the only solution found for $B = 2$, $N \geq 4$ and is hence identified as the global minimum.

The lower symmetry solution for $N = 3$, $B = 2$, shown in figure 4.2(b), is formed by two $B = 1$ single solitons, with a relative spatial rotation by π. This is as expected due to the form of the asymptotic fields being the same as for the standard planar Skyrme model. The leading order result states that two single solitons are in the maximally attractive channel when rotated relative to each other by π [25]. Due to the potential breaking axial symmetry, beyond leading order the asymptotic forces will discriminate between various orientations of the two solitons.

The most energetically favorable orientations for $B \geq 2$ appears to be that of polyforms [32], planar figures formed by regular N-gons joined along their edges. For the $N = 3$ case these are known as polyiamonds and for $N = 4$ polyominoes. Polyforms have been studied for millennia, with the earliest reference from ancient masters of the strategy game Go. We will represent each soliton as a regular N-gon, with N different colours located at the vertices, which are then joined along common edges. We can then see that each of the solutions shown in figures 4.2 and 4.3 exhibit this polyform structure.

Studying the solutions for $B = 3$, $N = 4$ as an example, the initial conditions described in equation (4.3.3) produces the unstable D_{12} maximally symmetric solution with energy $E/B = 33.43$. A slight perturbation of these initial conditions, breaking the maximal symmetry, forms either the  (line) solution in figure 4.3(c) or the solution in figure 4.3(d) with energies $E/B = 32.66$ and 32.77 respectively, this pattern continues for all $N \geq 4$. In this example the line solution appears to be the global energy minimum and this emerges to be the case for all N and $B \geq 3$.

Table 4.1: The energy for soliton solutions and their symmetry group G for $B \leq 4$ and (left) $N = 3$ (right) $N = 4$

B	form	E	E/B	G	figure
1		34.79	34.79	D_3	4.1(a)
2		66.07	33.04	D_6	4.2(a)
2		66.12	33.06	D_2	4.2(b)
3		101.04	33.68	D_9	4.2(c)
3		98.47	32.82	D_1	4.2(d)
3		100.94	33.65	D_3	4.4(a)
4		138.98	34.75	D_{12}	4.2(e)
4		130.65	32.66	C_2	4.2(f)
4		130.66	32.67	D_1	4.2(g)
4		131.80	32.95	D_3	4.2(h)
4		132.07	33.02	D_4	4.4(b)

B	form	E	E/B	G	figure
1		34.58	34.58	D_4	4.1(b)
2		65.58	32.79	D_8	4.3(a)
3		100.28	33.43	D_{12}	4.3(b)
3		97.97	32.66	D_2	4.3(c)
3		98.32	32.77	D_1	4.3(d)
3		98.71	32.90	D_3	4.4(c)
4		137.97	34.49	D_{16}	4.3(e)
4		129.94	32.49	D_2	4.3(f)
4		130.28	32.57	C_1	4.3(g)
4		131.61	32.90	D_1	4.3(h)
4		131.13	32.78	D_4	4.3(i)
4		130.61	32.65	C_2	4.3(j)
4		131.81	32.95	D_4	4.4(d)
4		135.94	33.98	D_4	4.4(e)

This is not a surprise due to the standard potential giving the same result as shown in [23]. If we look at some of the results for higher N, the solutions are very difficult to find as they tend to want to relax to the line solution instead. Due to this we did not actually find solutions for  ,  and  .

The two key forms of solution discussed above continues for various N and B. Some of these other solutions and energies can be seen in appendix A of this chapter. There are however several caveats to the general forms discussed above.

4.3.3 Caveats to the Standard Solutions

The first caveat is the formation of hole like structures, which can be seen in figure 4.4. These hole solutions form higher energy local minima, that break the predicted

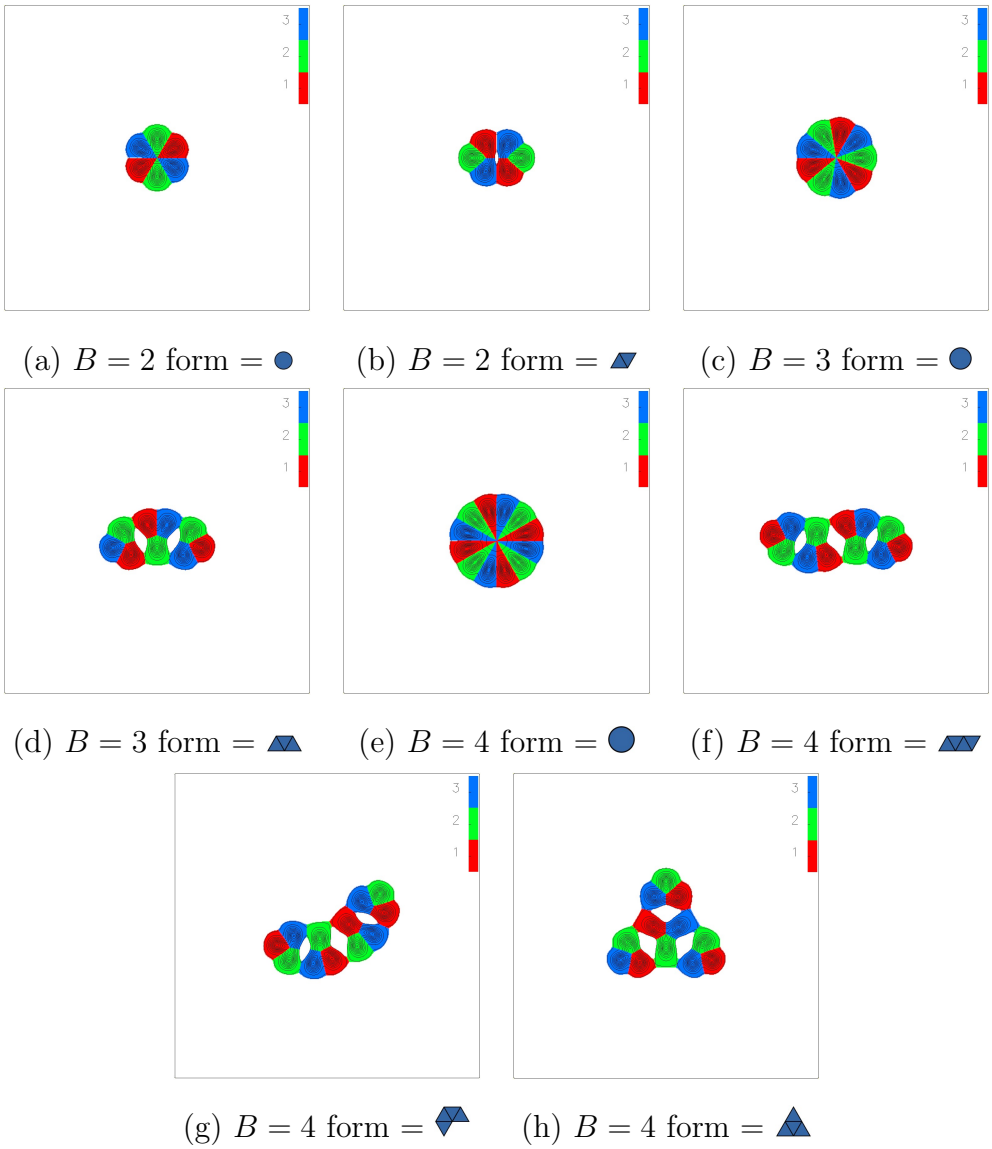

(a) $B = 2$ form = (b) $B = 2$ form = (c) $B = 3$ form =

(d) $B = 3$ form = (e) $B = 4$ form = (f) $B = 4$ form =

(g) $B = 4$ form = (h) $B = 4$ form =

Figure 4.2: Energy density plots of the multi-soliton solutions for $N = 3$ and $B \leq 4$ (colour is based on the segment in which the point lies in the target space).

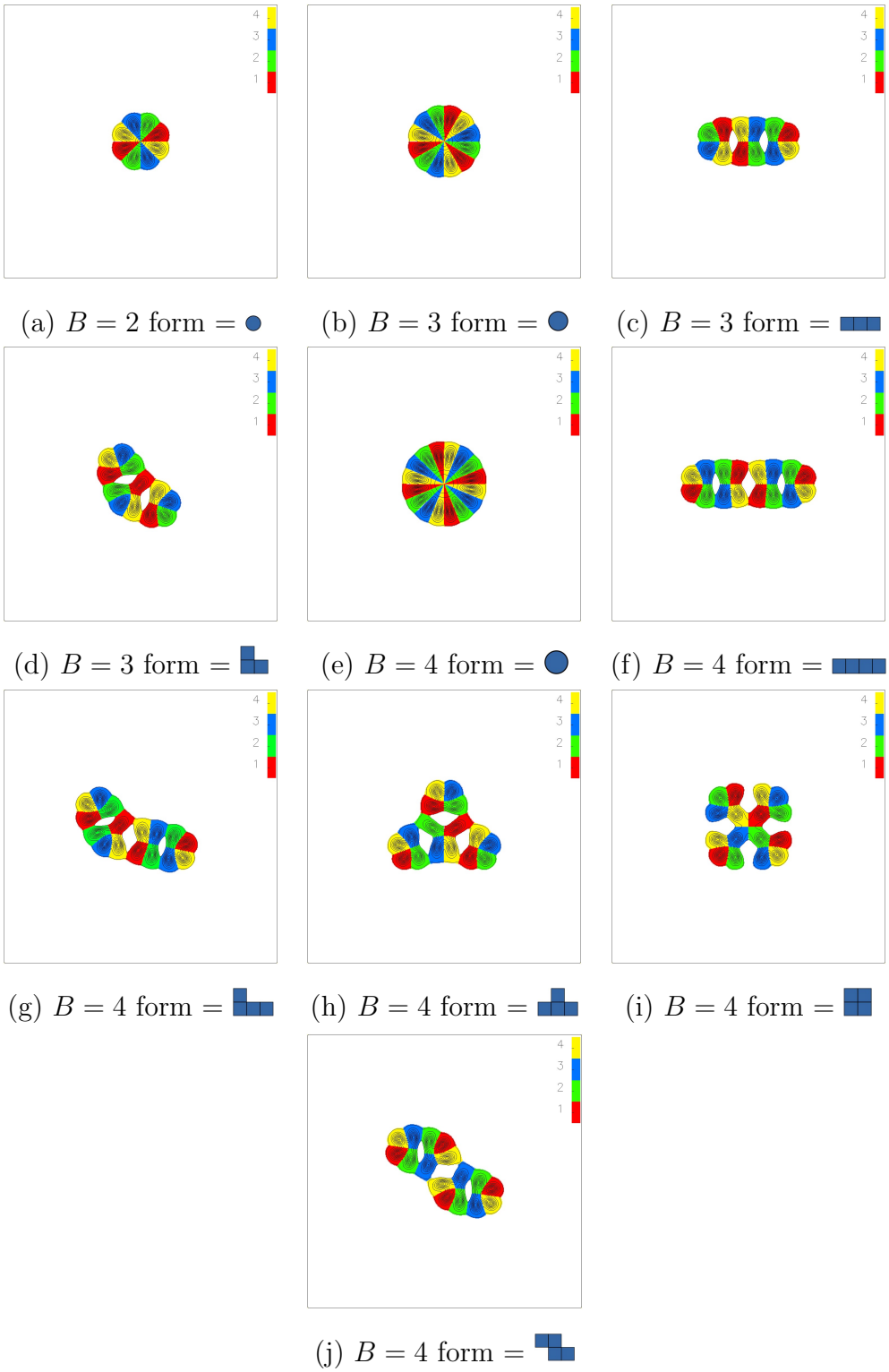

(a) $B = 2$ form = (b) $B = 3$ form = (c) $B = 3$ form =

(d) $B = 3$ form = (e) $B = 4$ form = (f) $B = 4$ form =

(g) $B = 4$ form = (h) $B = 4$ form = (i) $B = 4$ form =

(j) $B = 4$ form =

Figure 4.3: Energy density plots of the multi-soliton solutions for $N = 4$ and $B \leq 4$ (colour is based on the segment in which the point lies in the target space).

polyform structure. There is normally only one unique hole solution for each combination of $N \geq 3$ and $B \geq 3$. The solitons have a relative spatial rotation such that the edge contributing to the hole contains alternating colours, as shown in figure 4.4(a,b,c,d,f,h,j). However if $2B \mod N = 0$, we find that additional hole solutions form, with colours going sequentially round the hole as seen in 4.4(e,g,i,k,l). This can only occur for $2B \mod N = 0$ while retaining the required symmetry to stabalise the hole. Also as N increases, there is no reason why more or less partons can't be contributed to the hole per soliton, as seen in 4.4(l). Note that the standard hole solutions have significantly higher energies than that of the polyform solutions for the given B, while the second hole solutions have higher energies still.

The second caveat is the angle deformations of the $N \geq 4$ polyforms. If we consider figure 4.3(d), we can see that instead of forming a perfect angle of $\pi/2$, as we might expect for the  shape, the angle is obtuse. This is due to the derivative terms trying to force the phase to change smoothly. This means that segments of the target space next to each other, want to be positioned next to each other spatially. Hence non-neighbouring segments will repel each other as with  in figure 4.3(d) and  in figure 4.3(g), where green and yellow lie in non-neighbouring segments. This also adds weight to our proposal that the line solutions are the global minima, as this bending pulls the shapes out into more linear structures. The most prominent examples of this can be seen for $N \geq 5$, for example  in figure 4.7(e) and  in figure 4.8(f). This all stems from the partons themselves being able to move and hence bunch up in the soliton. So our solutions start to look further and further removed from this polyform structure even though they follow the simple rules outlined.

The final caveat occurs with $N = 5, 6$ only and is denoted  . This additional solution is similar to two warped maximally symmetric $B = 2$ solitons joined in a line, as seen in figures 4.7(m) and 4.8(o). They are of similar energy to the line solution suggesting that as we increase our value for N, the lower energy solution does appear to form line structures but not necessarily of standard single solitons.

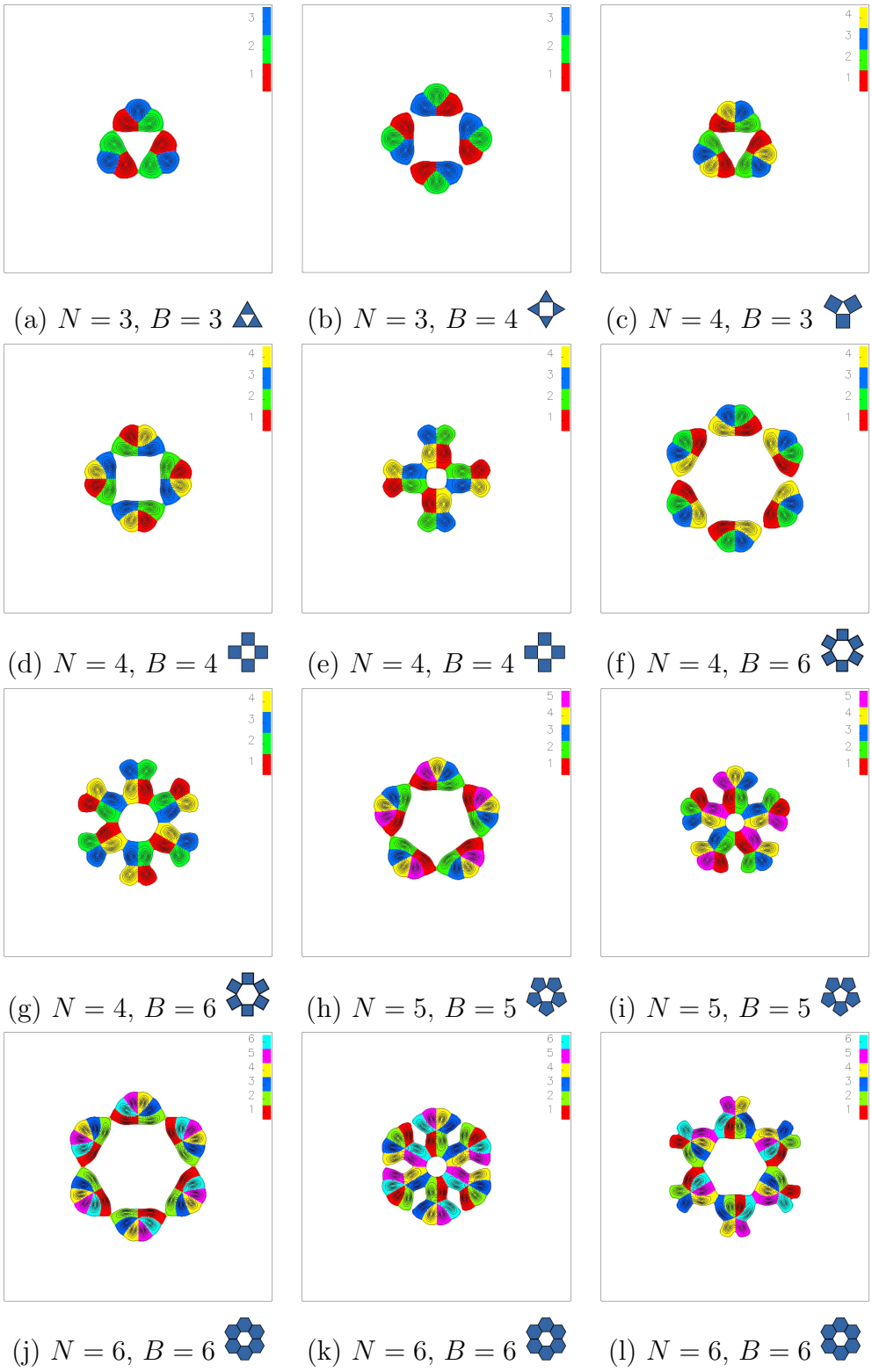

(a) $N = 3$, $B = 3$ (b) $N = 3$, $B = 4$ (c) $N = 4$, $B = 3$

(d) $N = 4$, $B = 4$ (e) $N = 4$, $B = 4$ (f) $N = 4$, $B = 6$

(g) $N = 4$, $B = 6$ (h) $N = 5$, $B = 5$ (i) $N = 5$, $B = 5$

(j) $N = 6$, $B = 6$ (k) $N = 6$, $B = 6$ (l) $N = 6$, $B = 6$

Figure 4.4: Energy density plots detailing the various hole caveats to the predicted polyform structure.

4.4 Dynamics

The goal of this section is to study the scattering of the various soliton solutions and draw parallels between our results and those of the standard planar Skyrme model [25]. Simulations were performed using a fourth order Runge-Kutta method. These were done on a grid of 751x751 grid points with $\Delta x = 0.04$ and $\Delta t = 0.01$. Our boundary again was fixed to be the vacuum and we included a suitable damping term at the boundary to remove any kinetic energy emitted. For each simulation we will indicate the initial relative spatial rotations denoted ψ_0 and positions denoted (x_0, y_0) of each soliton. We are working in the centre of mass frame, for example for $B = 2$ the velocities of the solitons are equal and opposite.

One notional aspect of these scatterings is what we can class as a soliton escaping to infinity. The natural position to take is if the soliton escapes to a point such that the boundary starts to have a significant damping effect on the velocity of the soliton. By slowly moving a soliton we estimate this to be at a distance 5 from the boundary. Hence if a soliton escapes to this line we will class it as having escaped to infinity for all intents and purposes.

4.4.1 $B = 2$ scattering

As one might expect, when given zero velocity the two solitons will attempt to align themselves into the attractive channel. Hence if aligned with $\psi_0 = \pi$ the solitons will remain in the attractive channel. However, unlike the standard potential there are additional terms beyond leading order, which cause the solitons to evolve such that they aligned face to face. This only has a significant effect at short range, as shown in figure 4.9 in Appendix B.

We are now interested in the head-on collision in the attractive channel with various initial velocities. We place the Skyrmions at $(6.0, 0)$ and $(-6.0, 0)$, using a range of velocities $0.1 \leq v \leq 0.6$.

As the solitons collide, they initially form the maximally symmetric solution seen in the $B = 2$ static case. They then emerge at $\pi/2$ to their initial direction of motion. This is the same as with the standard potential however what differs is the

scattering process itself. As the two solitons collide we can consider the scattering in terms of individual partons. The derivative terms in the energy mean that they evolve in such a way as to minimise the phase difference. Due to this, like colours can in fact overlap, however different colours will have a natural separation, based upon how far away their segments are in the target space.

Using the above we can predict what will occur in scattering processes, for example in a head-on collision in the attractive channel there are three situations that can occur, based upon the colour of the partons involved in the interaction.

- *like colours* - These partons will cross over each other and scatter at an angle bisecting the incident angles. So for two incident like colours with opposite velocities they will scatter at $\pi/2$.

- *sequential colours* - These partons want to lie next to each other, but cannot overlap, leading to the partons approaching each other and then stopping. As they are now the optimal distance apart they will bond together. Assuming the pair of sequential partons can then move off with enough other partons to form an integer charge soliton they will do so. Otherwise they will return to the original soliton they were a part of.

- *non-sequential colours* - These partons do not want to lie next to each other due to a sharper change in phase. Hence they have a larger natural distance and will stop before they approach each other. They will follow the path of the sequential partons they are already bound to when scattering.

So scattering processes are determined by the like and sequential colours that meet. If we look at the scattering shown in figure 4.5 we see first the two sets of sequential colours coming together and stopping as predicted. The green partons continue to move, first forming the $B = 2$ maximally symmetric solution and then continuing on to overlap and scatter at $\pi/2$. As the sequential colours are currently close enough to be bonded with either of the sequential colours next to it, it is the path of the green partons that will determine which pairs will form the single solitons. Hence the green partons bond with one of the other bonded pairs to form a complete soliton, thus scattering at $\pi/2$.

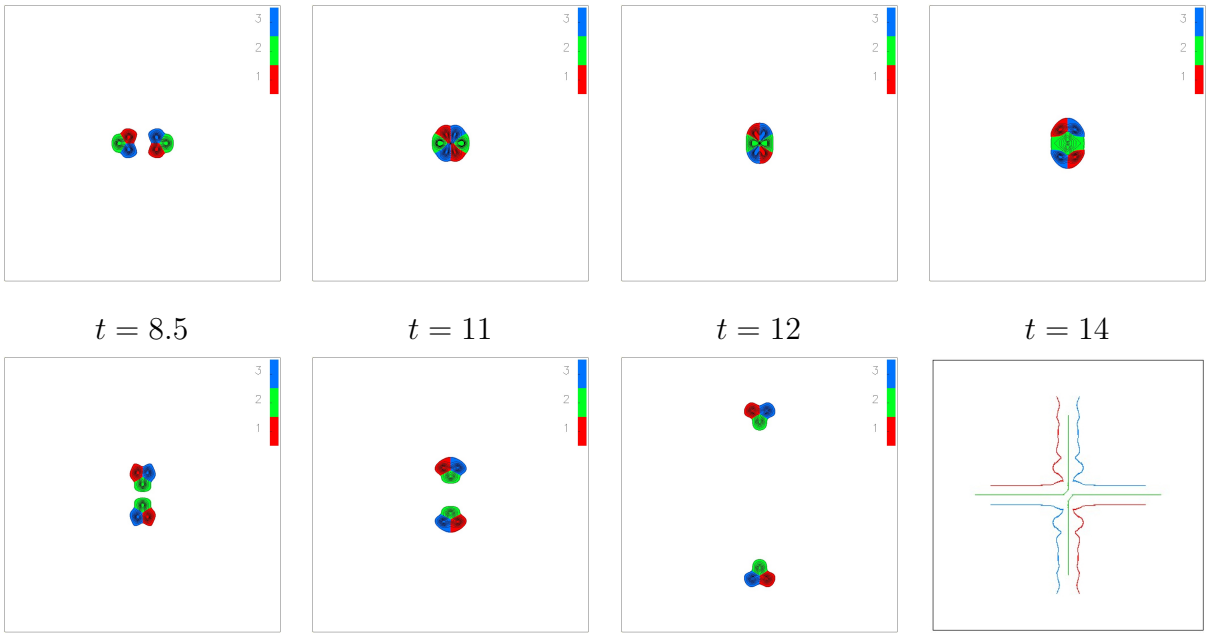

Figure 4.5: Energy density plots at various times during the scattering of two $N = 3$ single solitons each with speed 0.4 and with relative spatial rotation of π

If we now look at the scattering process in figure 4.6 we see only sequential colours meeting. These bond together to form two solitons from different partons.

In our model we observe a large quantity of kinetic radiation emitted when this intermediate state of the maximally symmetric solution is formed. This radiation significantly reduces the energy from the colliding solitons meaning the escape velocity (v_e) of the process is quite high (for the processes we looked at a range of about 0.3 to 0.5 was measured). It is also dependent upon the orientation of the solitons in the initial conditions. If we consider the case $v < v_e$, after the collision the attractive forces of the solitons pulls them so they re-collide. The form of this second collision is the time reversal of the original collision however with a smaller velocity. It is also accompanied by the emission of kinetic radiation, and this process will continue until the solitons don't have the kinetic energy to escape the intermediate state of the maximally symmetric solution. The solitons are no longer distinct, and the motion looks more like the excitation of the 2-soliton solution.

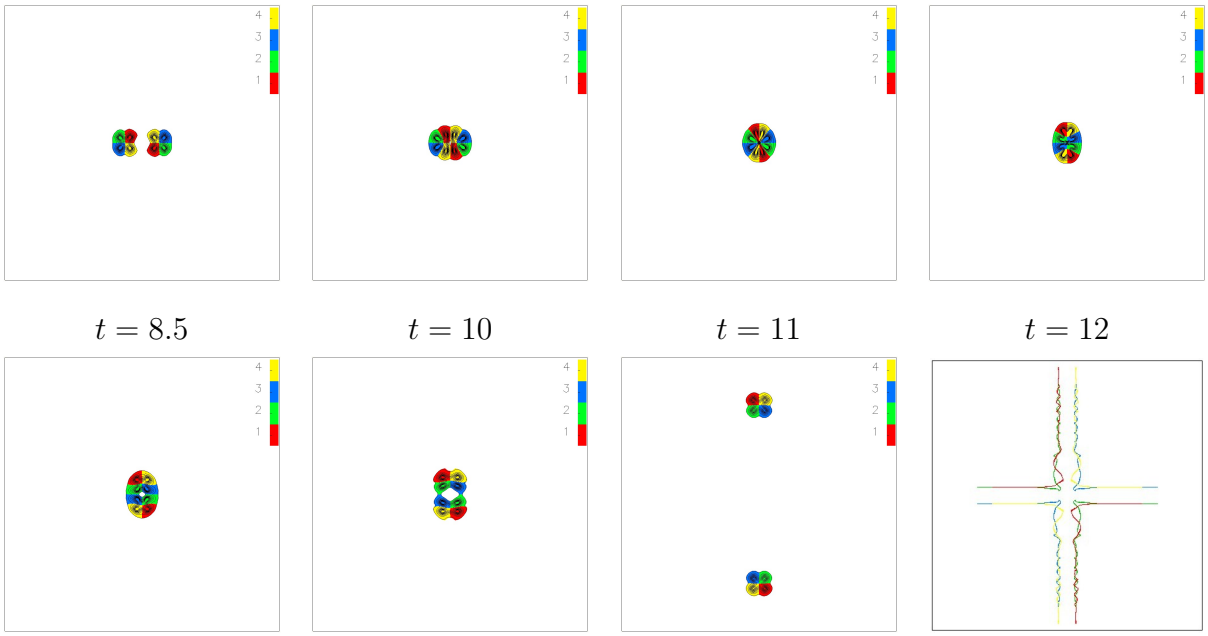

Figure 4.6: Energy density plots at various times during the scattering of two $N = 4$ single solitons each with speed 0.4 and with relative spatial rotation of π

4.4.2 $B \geq 3$ scattering

For more than two solitons the scattering processes are a little more complicated but can still be broken down into these simple parton-parton scattering structures discussed above. If we look at the scattering of $N = 3$ $B = 3$ in figure 4.10, we see that it continues to follow the simple rules outlined in the previous subsection. The initial partons meet in the centre scattering at $\frac{2\pi}{3}$, (bisecting the angle of approach relative to each other). The other partons then bond with their neighbour as they sit next to each other in the target space and are dragged off with the blue partons emitted from the centre. Note that a point first scattering is possible, as the attractive asymptotic contribution from edges cancels. This pattern continues for higher values of N and B.

4.5 Conclusions

The broken potential breaks the global symmetry to the dihedral group D_N. This results in a single soliton composed of N topologically confined partons represented

by different colors. We have also extended previous work to demonstrate that multi-soliton solutions take the form of polyforms for all values of N. An interesting extension to this would be to consider the soliton lattice formed by tiling these solutions. This was done by Jäykkä *et al.* [31] for $N = 3$ and as expected the cell was found to be the single soliton which was then tessellated in a cell similar to the standard planar Skyrme model. For those N-gons that tessellate (e.g. $N = 4$ or 6) this is likely to produce similar results as the $N = 3$ results, but with some differences due to the corner caveats discussed in section 3.3. Some clues are given in the solutions  and  in figures 4.3(i) and 4.8(m) respectively. For those solutions that don't tessellate, the solution is expected to be more complicated.

The dynamics of the model was also shown to be classically dependent upon the number of colours N. Each scattering process can be understood by considering the separate behaviour of the partons themselves. Additionally we see that the short range forces differ from the standard model, as it is energetically favourable for edges to be aligned.

The natural extension to this paper is the analogue in the full (3+1)-dimensional Skyrme model. The idea of being able to consider a scattering process by looking at the constituent makeup of the soliton, should transfer to the full model. However if an analogous symmetry breaking potential is constructed in the Skyrme model, we have the physical consequence that isospin symmetry is broken. It is not clear what the physical consequences of this would be.

4.6 Appendix A: Static Solitons for $N = 5, 6$

This section contains the static solutions along with their energies for $N = 5, 6$ upto $B = 4$. These results further confirm our predictions but also introduce some interesting caveats which are covered in the caveats section of the paper. Note that the  solution was not obtained, although we still expect this solution to exist. It was very similar to the  caveat in 4.7(m) meaning it was difficult to pick out initial conditions that would relax to the desired solution rather than this lower energy caveat form

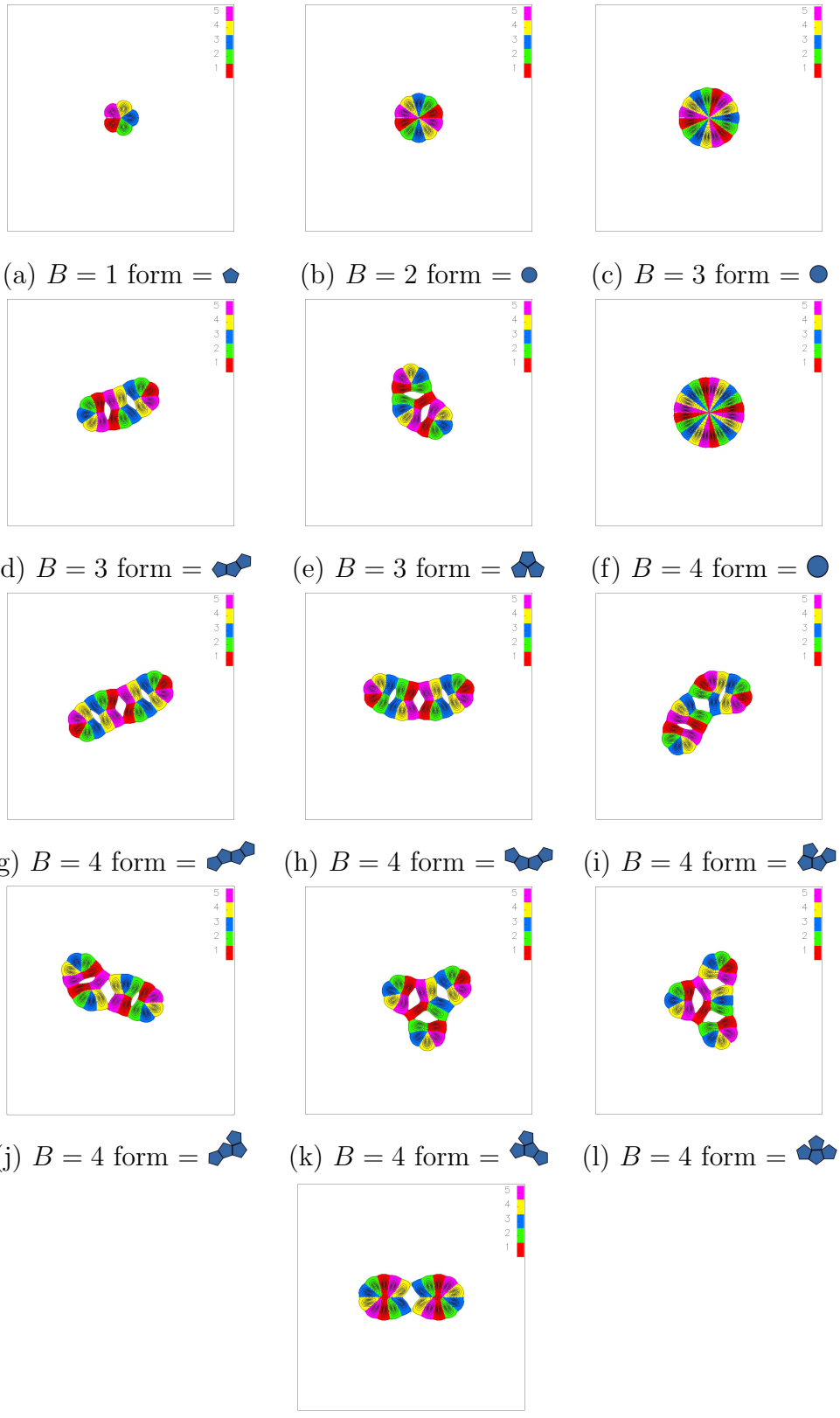

(a) $B = 1$ form = (b) $B = 2$ form = (c) $B = 3$ form =

(d) $B = 3$ form = (e) $B = 3$ form = (f) $B = 4$ form =

(g) $B = 4$ form = (h) $B = 4$ form = (i) $B = 4$ form =

(j) $B = 4$ form = (k) $B = 4$ form = (l) $B = 4$ form =

(m) $B = 4$ form =

Figure 4.7: Energy density plots of the multi-soliton solutions for $N = 5$ and $B \leq 4$ (colouring is based on the segment in which the point lies in the target space).

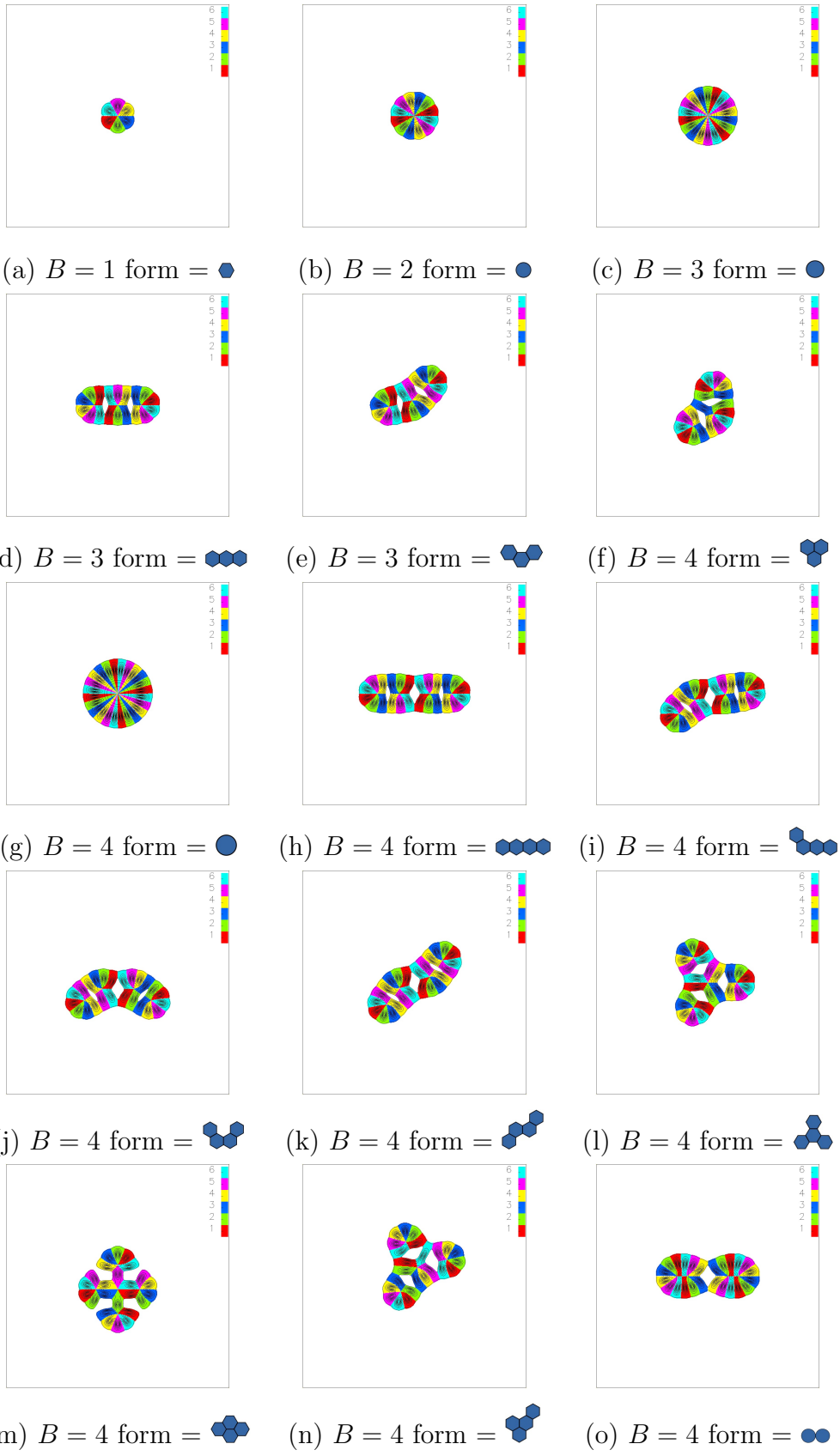

(a) $B = 1$ form = (b) $B = 2$ form = (c) $B = 3$ form =

(d) $B = 3$ form = (e) $B = 3$ form = (f) $B = 4$ form =

(g) $B = 4$ form = (h) $B = 4$ form = (i) $B = 4$ form =

(j) $B = 4$ form = (k) $B = 4$ form = (l) $B = 4$ form =

(m) $B = 4$ form = (n) $B = 4$ form = (o) $B = 4$ form =

Figure 4.8: Energy density plots of the multi-soliton solutions for $N = 6$ and $B \leq 4$ (colouring is based on the segment in which the point lies in the target space).

Table 4.2: The energy for soliton solutions and their symmetry group G for $B \leq 4$ and (left) $N = 5$ (right) $N = 6$.

B	form	E	E/B	G	figure
1		34.41	34.41	D_5	4.7(a)
2		65.19	32.59	D_{10}	4.7(b)
3		99.23	33.23	D_{15}	4.7(c)
3		97.68	32.56	C_1	4.7(d)
3		98.14	32.71	C_1	4.7(e)
4		137.20	34.30	D_{20}	4.7(f)
4		129.62	32.40	D_2	4.7(g)
4		129.61	32.40	C_1	4.7(h)
4		130.69	32.67	C_1	4.7(i)
4		130.06	32.52	C_1	4.7(j)
4		131.11	32.78	C_1	4.7(k)
4		131.50	32.87	C_1	4.7(l)
4		129.65	32.41	D_1	4.7(m)

B	form	E	E/B	G	figure
1		34.26	34.26	D_6	4.8(a)
2		64.88	32.44	D_{12}	4.8(b)
3		99.23	33.08	D_{18}	4.8(c)
3		97.32	32.44	D_2	4.8(d)
3		97.47	32.49	D_1	4.8(e)
3		97.98	32.66	D_3	4.8(f)
4		136.60	34.15	D_{24}	4.8(g)
4		129.11	32.28	D_2	4.8(h)
4		129.26	32.32	C_1	4.8(i)
4		129.41	32.35	D_1	4.8(j)
4		129.41	32.35	D_2	4.8(k)
4		130.58	32.64	D_3	4.8(l)
4		130.79	32.70	D_2	4.8(m)
4		130.85	32.71	D_1	4.8(n)
4		129.09	32.27	D_1	4.8(o)

4.7 Appendix B: Additional Scatterings

In this section we present a few additional scatterings that demonstrate that the simple rules outlined in the scattering section apply to more complicated systems. Figure 4.9 demonstrates how the broken potential introduces additional terms making edges wanting to come together. Hence the solitons rotate into the maximally attractive channel before they scatter, then continuing to rotate after the scattering while preserving the symmetry of the system.

In figure 4.10 we see and example of scattering for a higher value of B, specifically $B = 3$. This demonstrates that the standard rules still apply for a higher number of solitons. The like colours scattering in the centre, bisecting the angles on which they approached. With colours linked to neighbouring segments in the target space then bonding together.

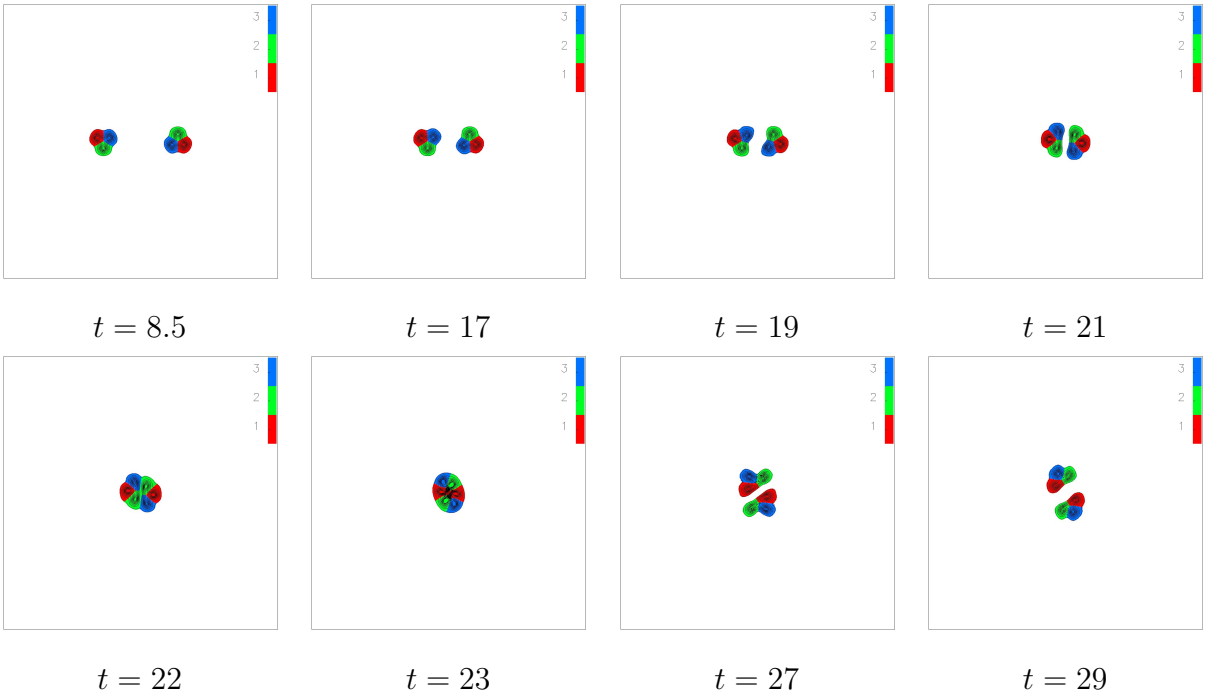

Figure 4.9: Energy density plots at various times during the scattering of two $N = 3$ single solitons each with speed 0.4 and with relative spatial rotation of π. The solitons' edges however, are not aligned.

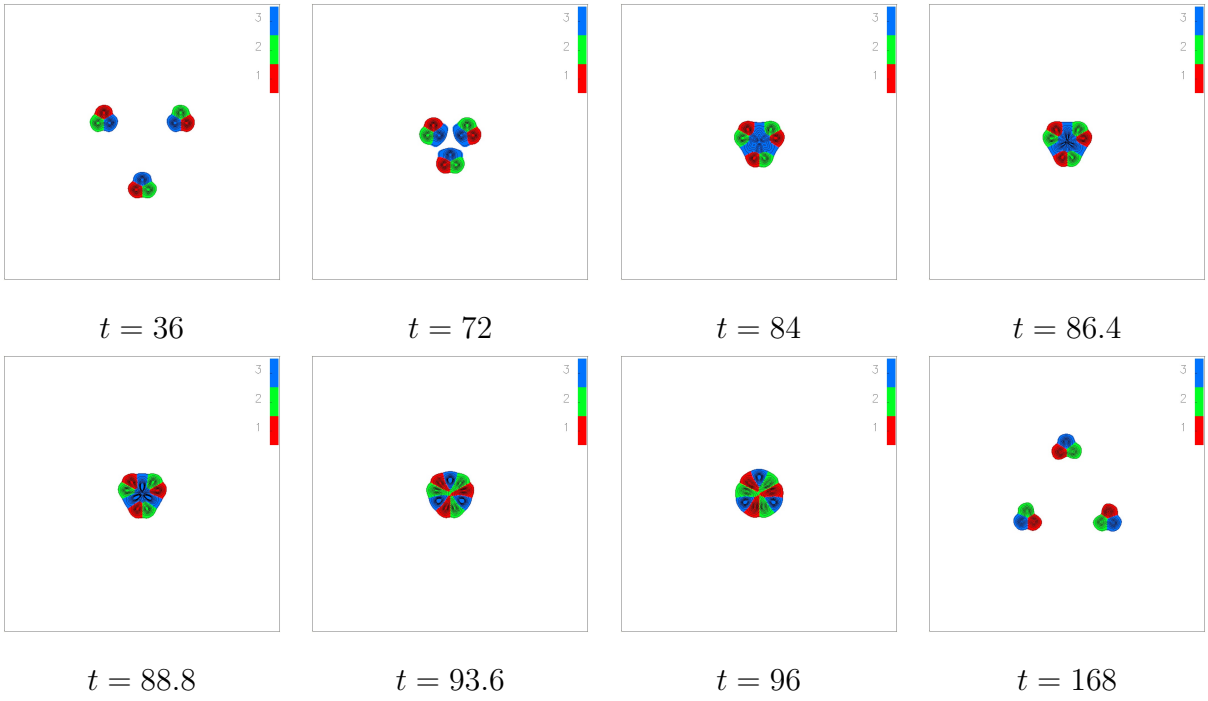

Figure 4.10: Energy density plots at various times during the scattering of three $N = 3$ single solitons each with speed 0.3 and with relative spatial rotation of $\frac{2\pi}{3}$.

Part III

(3+1) Skyrme Model

Chapter 5

$SU(2)$ Skyrme Model

5.1 Introduction

This chapter constitutes a brief introduction to the $(3+1)$ $SU(2)$ Skyrme model, and as thus isn't original work, but a rewording of the well known and familiar details of the model. For a more in-depth look at the Skyrme model see [5].

The Skyrme model [13] is a (3+1)-dimensional nonlinear theory of pions, that admits topological soliton solutions, called Skyrmions. It was first proposed by T.H.R. Skyrme as a modification of the sigma model, with the aim of describing baryon physics. At the time the quantum tools were not available to really utilise the model. However it was revived by Balachandran et al. [33, 34] and Witten [35], and demonstrated some similar properties to those observed during experiment.

The model has now been well studied [5] with solutions calculated for a large range of topological charges [36]. It has been obtained from quantum chromodynamics (QCD) [35, 37], and more recently from holographic QCD, as a low-energy effective theory in the large colour limit [38].

5.2 The Model

The Skyrme field $U(t, \boldsymbol{x})$ in three spatial dimensions is defined as the map,

$$U : \mathbb{R}^3 \to S^3. \tag{5.2.1}$$

As S^3 is the group manifold of $SU(2)$ we take $U(t, \boldsymbol{x})$ to be an $SU(2)$-valued scalar. Theories with alternate groups have been studied, such as considering the more general $SU(N_f)$ where N_f is the number of flavours of quark. The $SU(2)$ case, models up and down quarks and is the most physical for modelling nuclear physics, due to it only being weakly broken in nature. The energy of the theory is given by the functional,

$$E = \frac{1}{12\pi^2}\int \left\{ -\frac{1}{2}Tr\left(R_i R^i\right) - \frac{1}{16}Tr\left(\left[R_i, R_j\right]\left[R^i, R^j\right]\right) + m^2 V(U) \right\} d^3x, \quad (5.2.2)$$

where $R_i = (\partial_i U)\, U^\dagger$ is the right $su(2)$ valued current. Note that this equation has had the parameters preceding the first two terms scaled out. This may not at first glance look similar to the planar model considered in the previous section. However we can rewrite the energy (5.2.2) in terms of the pions fields using the $SU(2)$ nature of $U = \sigma + i\boldsymbol{\pi}\cdot\boldsymbol{\tau}$, where $\boldsymbol{\tau}$ is the triplet of Pauli matrices, $\boldsymbol{\pi} = (\pi_1, \pi_2, \pi_3)$ the triplet of pion fields and the sigma field σ is some real number. The $SU(2)$ nature of the field is then represented using the relation $\sigma^2 + \boldsymbol{\pi}\cdot\boldsymbol{\pi} = 1$.

The vacua of the energy are given by any constant U. Hence, due to finite energy requirements, the field on the boundary must be constant and without loss of generality can be chosen to be $\lim_{|\boldsymbol{x}|\to\infty} U(t, \boldsymbol{x}) = 1_2$ or alternatively $\boldsymbol{\pi} = \mathbf{0}$, $\sigma = 1$. This allows us to compactify the physical space $\mathbb{R}^3 \cup \{\infty\} = S^3$ giving the degree of the map U to take values in the homotopy group $B \in \pi_3(S^3) \equiv \mathbb{Z}$. Hence the maps can be indexed using an integer topological charge, which can be written in integral form using the pull back of the standard area form on S^3,

$$B = -\frac{1}{24\pi^2}\int \epsilon_{ijk} Tr\left(R_i R_j R_k\right) d^3\boldsymbol{x}. \quad (5.2.3)$$

We will, somewhat suggestively, also refer to the topological charge B from here on out as the baryon number.

The energy (5.2.2) has the symmetry group $(SU(2)\times SU(2))/\mathbb{Z}_2 \sim SO(4)$ which is a chiral symmetry that is spontaneously broken by our choice of boundary conditions to an $SO(3)$ symmetry that acts as

$$U \to \mathcal{O}U\mathcal{O}^{\dagger}, \qquad \mathcal{O} \in SU(2). \tag{5.2.4}$$

In terms of the pion fields this provides a rotation $\boldsymbol{\pi} \to M\boldsymbol{\pi}$, where $M_{ij} = \frac{1}{2}Tr\left(\tau_i \mathcal{O} \tau_j \mathcal{O}^{\dagger}\right)$ is an $SO(3)$ matrix.

This symmetry can be broken further by an appropriate choice of mass term V, which is considered in a later chapter. For this section however we consider the standard pion mass term,

$$V(U) = Tr\left(1 - U\right). \tag{5.2.5}$$

It is easy to see that this leads to the pions having a tree-level mass m. One of the key differences between the full 3-dimensional Skyrme model and the planar model is the existence of stable static solutions with massless pions ($m = 0$). This can be seen by considering a spatial rescaling $\boldsymbol{x} \to \mu\boldsymbol{x}$ of the energy functional (5.2.2) to obtain,

$$e\left(\mu\right) = \frac{1}{\mu}E_2 + \mu E_4 + \frac{1}{\mu^3}E_0. \tag{5.2.6}$$

As discussed in the first chapter, Derrick's theorem requires the theory to have two terms that scale in the opposite way to each other, to admit stable solutions. The first two terms of the energy functional scale oppositely, meaning that the mass term can be set to zero while admitting stable soliton solutions. This leads to the pions being interpreted as the Goldstone bosons of the spontaneously broken chiral symmetry discussed above.

By applying the Cauchy-Schwarz inequality to the energy functional we can obtain the Bogomolny bound given as,

$$E \geq 12\pi^2 \left|B\right|. \tag{5.2.7}$$

Previously in the baby Skyrme model we suggested that the Bogomolny bound was unattainable due to the mass term. Here the mass term is not required, however the bound is still unattainable. This is because to saturate this bound (for non-trivial configurations) all the eigenvalues of the strain tensor must have modulus 1 for all

of space. Note that it is possible to attain the bound if the Skyrmions are embedded onto a 3-sphere of unit-radius.

5.3 $B = 1$ Hedgehog

As with the planar model, due to symmetric criticality, the charge one solution retains the maximal $SO(3)$ global symmetry of the system. This solution is known as the hedgehog ansatz and can be written exactly using the ansatz,

$$U(\boldsymbol{x}) = exp\{if(r)\,\hat{\boldsymbol{x}}\cdot\boldsymbol{\tau}\} \tag{5.3.8}$$

$$\boldsymbol{\pi} = \sin f(r)\,\hat{\boldsymbol{x}}, \quad \sigma = \cos f(r) \tag{5.3.9}$$

where $f(r)$ is a profile function that monotonically decreases, with the boundary conditions $f(0) = \pi$ and $f(\infty) = 0$, that must be found numerically.

If we substitute this solution into the energy functional (5.2.2) we get the following radial energy,

$$E = \frac{1}{3\pi}\int_0^\infty \left(r^2 f'^2 + 2\left(f'^2+1\right)\sin^2 f + \frac{\sin^4 f}{r^2} + 2m^2 r^2\left(1-\cos f\right)\right) dr. \tag{5.3.10}$$

The profile function $f(r)$ can then be found by minimising the above energy using some simple gradient flow method. The solution for a few various values for m is given in figure 5.1(a). If we linearise the equation of motion that results from varying equation (5.3.10), we can study the asymptotics of the profile f, showing it decays exponentially,

$$f \sim \frac{A_e}{r}e^{-mr}. \tag{5.3.11}$$

Note that in the massless limit this asymptotic decay becomes algebraic $f \sim A_a r^{-2}$.

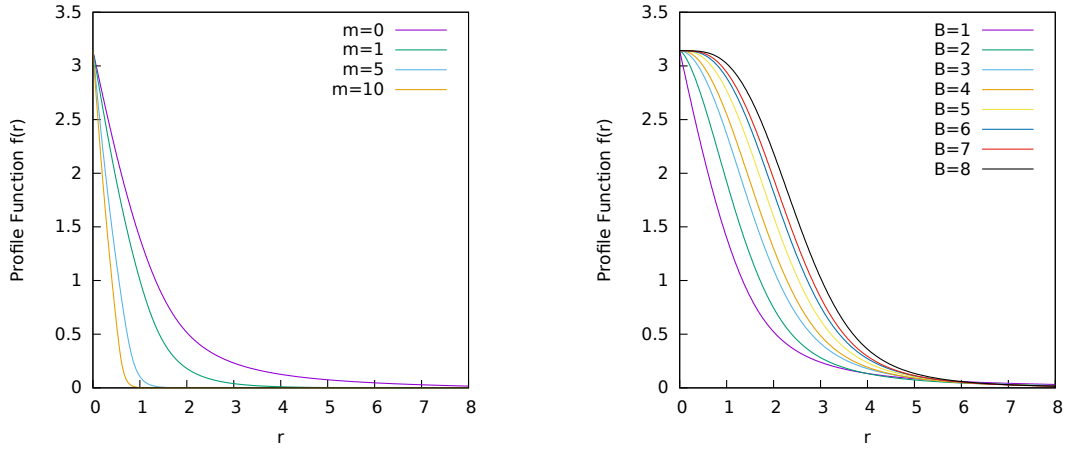

(a) $B = 1$, $m = 0 - 10$ (b) $B = 1 - 8$, $m = 0$

Figure 5.1: Profile functions $f(r)$ for the rational map approximation. The left image contains the solutions for the $B = 1$ hedgehog ansatz, for various values of the mass parameter m. The right graph shows the profile functions that minimise the rational map ansatz energy, for various values of charge and $m = 0$.

5.4 Higher Charge Solutions $(B > 1)$

Th static solutions with higher Baryon number, are not as simple as the planar model from the previous part. Luckily there are a few approximations that allow predictions of minimal energy results, or at least initial conditions to the process of energy minimisation, that can be used to find the true minimal energy solutions.

The first approximation is the product ansatz, which allows the combination of the field solutions for lower baryon numbers to be combined into a single field,

$$U = U_1 U_2. \tag{5.4.12}$$

This ansatz holds up well assuming that the solitons are well separated with respect to their size. The resulting baryon number of the configuration is the sum of the combined fields $B = B_1 + B_2$. This approximation does not give good approximations for minimal energy solutions, however it does give good initial conditions that can be evolved, to find static or dynamic solutions and will be used throughout this section.

There are two other approximations that will prove useful in this thesis. Firstly the rational map approximation is an extremely accurate approximation for shell like solutions, which is discussed in detail in the following section. The final approximation is modelling Skyrmions by computing the holonomy of $SU(2)$ Yang-Mills instantons in $\mathbb{R}^4$ along lines parallel to the time axis [39].

$$U(\boldsymbol{x}) = \pm\mathcal{P}e^{\int_{-\infty}^{\infty} A_4(\boldsymbol{x},x_4)\,dx_4}, \tag{5.4.13}$$

where $\mathcal{P}$ represents path ordering. As these are not limited to shell-like configurations, this produces a more general method over the rational map ansatz, however it can only generate the correct algebraic decay for massless pions. It has been demonstrated for example, that there exists an instanton on $\mathbb{T}^4$ whose holonomy gives an approximation of the Skyrme crystal [40]. We will not discuss this method in detail here, but the approximation does give a handy result in predicting the form of the profile function of a charge 1 Skyrmion without a mass term,

$$f(r) = \pi\left(1 - \frac{r}{\sqrt{\lambda^2 + r^2}}\right). \tag{5.4.14}$$

Note that the λ parameter is due to the conformal symmetry of the instantons and must be found numerically.

5.5 Rational Map Ansatz

For the standard massive and massless pion theories, the minimal energy solutions take highly symmetric forms. These can be approximated using the rational map ansatz, which approximates the angular dependence of the solution to be a rational map between Riemann spheres [41]. This reduces the theory to solving an ODE and numerically finding a profile function. The field approximation is given to be,

$$U(r,z) = exp\left[\frac{if(r)}{1+|R|^2}\begin{pmatrix} 1-|R|^2 & 2\bar{R} \\ 2R & |R|^2-1 \end{pmatrix}\right] \tag{5.5.15}$$

where $z = e^{i\phi}\tan\left(\frac{\theta}{2}\right)$ is the Riemann sphere coordinate and $R(z)$ is a degree B rational map between Riemann spheres. Substituting this ansatz into the energy

(5.2.2), we get the following radial equation,

$$E = \frac{1}{3\pi}\int \left(r^2 f'^2 + 2B\left(f'^2+1\right)\sin^2 f + \mathcal{I}\frac{\sin^4 f}{r^2} + 2m^2 r^2\left(1-\cos f\right)\right) dr \quad (5.5.16)$$

where

$$\mathcal{I} = \frac{1}{4\pi}\int \left(\frac{1+|z|^2}{1+|R|^2}\left|\frac{dR}{dz}\right|\right)^4 \frac{2i dz d\bar{z}}{\left(1+|z|^2\right)^2}. \quad (5.5.17)$$

$\mathcal{I}$ is an integral to be minimised by the choice of rational map $R(z)$. The minimal values of $\mathcal{I}$ and the associated rational maps were found in [36] for a range of values of B. The isospin symmetry of the pion fields can now be represented by performing an $SU(2)$ Mobius transformation of the rational map,

$$R(z) \to \frac{\alpha R(z) + \beta}{-\bar{\beta}R(z) + \bar{\alpha}} \quad (5.5.18)$$

where $|\alpha|^2 + |\beta|^2 = 1$.

The rational map ansatz is highly accurate at giving the global minimum to the energy for massless solutions, giving an approximation about 1% above the correct value. These approximations are highly symmetric and tend to have polyhedral symmetries in a shell like form. When mass is introduced into the model, the ansatz breaks down for higher values of charge.

5.6 Higher Charge Solutions

The minimal energy solutions for the massless theory can be seen in figure 5.2. These solutions take the form of highly symmetric shell like solutions as predicted by the rational map ansatz. The energies and symmetry groups are given in table 5.1.

While we have considered only the massless solutions here, the addition of a mass term has little effect on solutions of low Baryon number, which continue to form shell like structures. However for larger charge solutions, a mass term starts to favour minimal energy solutions formed of finite chunks of a Skyrme crystal [42–44]. Namely a lattice with cubic symmetry that can be interpreted as multiple $B = 4$ solutions joined together.

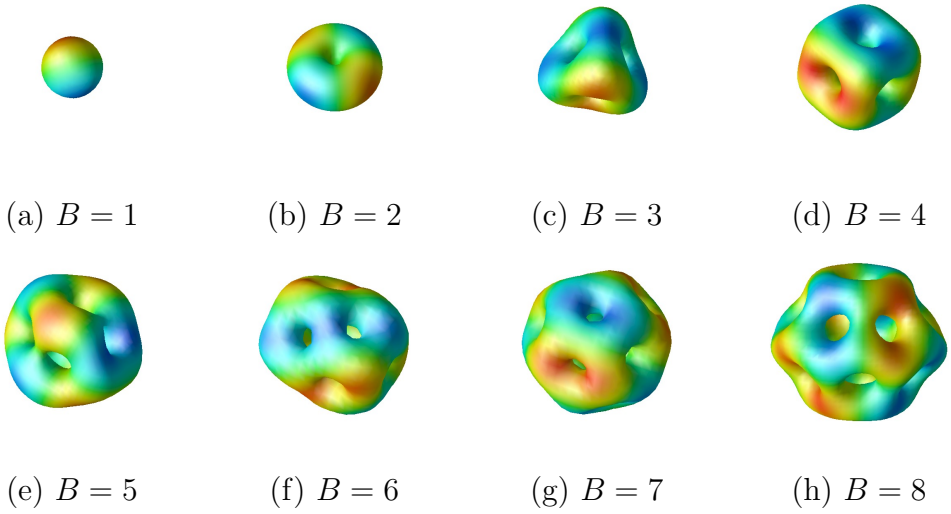

(a) $B = 1$ (b) $B = 2$ (c) $B = 3$ (d) $B = 4$

(e) $B = 5$ (f) $B = 6$ (g) $B = 7$ (h) $B = 8$

Figure 5.2: Energy density isosurface plots of the minimal energy solutions for the Skyrme model, with massless pions $m = 0$. Each isosurface is plotted using the same value and the same sized grid. The surfaces are coloured by the π_2 field. Each solution retains the symmetry of the rational map that minimises the value of $\mathcal{I}$ in equation (5.5.17).

B	G	$\mathcal{I}$	E_R/B	E/B	figure
1	$O(3)$	1.0	1.232	1.2322	5.2(a)
2	$D_{\infty h}$	5.8	1.208	1.1791	5.2(b)
3	T_d	13.6	1.184	1.1462	5.2(c)
4	O_h	20.7	1.137	1.1201	5.2(d)
5	D_{2d}	35.8	1.147	1.1172	5.2(e)
6	D_{4d}	50.8	1.137	1.1079	5.2(f)
7	Y_h	60.9	1.107	1.0947	5.2(g)
8	D_{6d}	85.6	1.118	1.0960	5.2(h)

Table 5.1: Table of energies normalised by the topological charge E/B for the minimal energy solutions for charges $B = 1 - 8$. Also included is the normalised energy of the rational map ansatz E_R/B (for the rational map that minimises the value of $\mathcal{I}$ which is also included). The symmetry of the solutions is also given G, for both the rational map approximation and minimal energy solution.

5.7 Dynamics

Scattering of single solitons for the Skryme model is somewhat similar to the planar version of the model. We can calculate the interaction energy for two well separated Skyrmions using the asymptotic form of the tail for a charge 1 hedgehog solution. The interaction energy can then be found by assuming the Skyrmion fields act as a pair of dipole triplets (though a more rigorous method is needed to show this assumption gives the correct form) [45],

$$E_{int} = -\frac{A^2}{3\pi}\left(1-\cos\psi\right)\frac{1-3\left(\hat{\boldsymbol{X}}\cdot\hat{\boldsymbol{n}}\right)^2}{|\boldsymbol{X}|^3}, \tag{5.7.19}$$

where $\boldsymbol{X}$ is a relative position vector of one of the dipoles from the other and ψ the relative rotation around the axis $\hat{\boldsymbol{n}}$. The maximally attractive channel then corresponds to setting $\hat{\boldsymbol{X}}\cdot\hat{\boldsymbol{n}}=0$ and $\psi=\pi$. Effectively this means the solitons are rotated by π around an axis orthogonal to the line connecting the centres of the solitons. This process can be seen in figure 5.3, where two single solitons are in the attractive channel. The solitons scatter at an angle π, conserving the momentum of the system. As the isosurfaces move through each other they form the familiar toroidal $B=2$ minimal energy configuration with $O(2)\times\mathbb{Z}_2$ symmetry. They are emitted again in the maximally attractive channel and assuming their velocity isn't large enough to escape the interaction, they will scatter again. As they move through the lower energy configuration they emit kinetic energy each time, hence they will continuously scatter emitting energy, until they settle down to the minimal energy $B=2$ toroidal configuration seen in figure 5.2 (b).

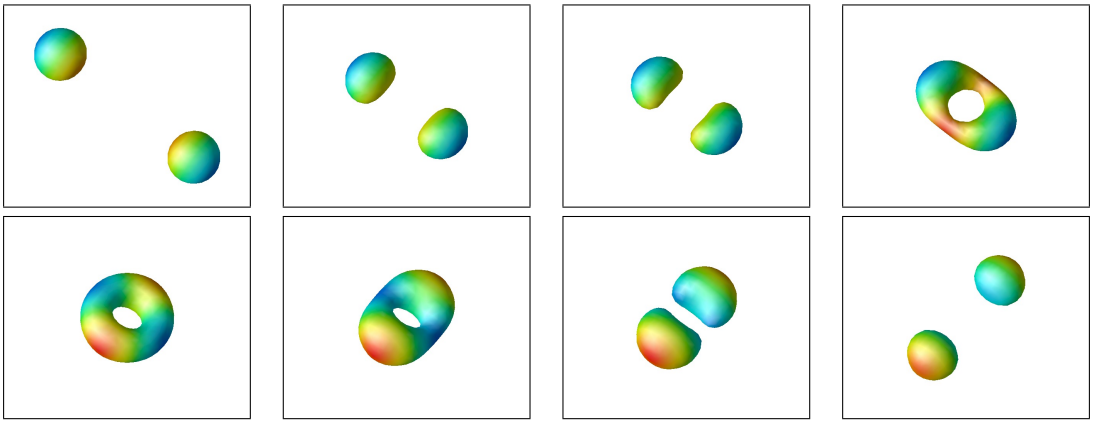

Figure 5.3: Energy density isosurface plot of the scattering of two Skyrmions in the attractive channel (rotated by π around an axis orthogonal to the straight line connecting the soliton centres). They scatter at an angle $\pi/2$ transitioning through the familiar toroidal minimal energy $B = 2$ solution. The plot is coloured by the π_2 field.

Chapter 6

Skyrmion Formation

6.1 Introduction

In this chapter we numerically simulate the formation of $(3+1)$-dimensional $SU(2)$ Skyrmions from domain wall collisions. This is taken from the second part of the paper [4]. It has previously been suggested that Skyrmion, anti-Skyrmion pairs can be produced from the interaction of two domain walls. We confirm this and demonstrate that the process can be improved in terms of reliability by using multiple colliding domain walls.

Normally domain walls will annihilate, however if they interact in such a way as to produce the correct winding in the target space, then soliton anti-soliton pairs can be formed. This was shown for baby Skyrmions in chapter 3 and we will show that for the full Skyrme model a similar process exists, that works in a similar fashion to the ideas presented in chapter 3. In the $(3+1)$ full Skyrme model, there is an additional field and dimension over the previously discussed baby Skyrme model, which is needed to wind correctly, with the domain walls forming a spherical object in the physical space.

There is a large amount of increased interest in how solitons can be formed, especially cosmological models which include phase transitions in the early universe [10].

We consider the alternate mass term as,

$$V(U) = \left(1 - \sigma^2\right) \tag{6.1.1}$$

Where the sigma term is a scalar component of U that can be extracted from the original $SU(2)$ formulation by writing $U = \sigma + i\boldsymbol{\pi} \cdot \boldsymbol{\tau}$, where $\boldsymbol{\tau}$ is the triplet of Pauli matrices, $\boldsymbol{\pi} = (\pi_1, \pi_2, \pi_3)$ the triplet of pion fields and the sigma field σ is some real number that can be found using the requirement that $\sigma^2 + \boldsymbol{\pi} \cdot \boldsymbol{\pi} = 1$. We have imposed this mass term to give us two vacua, noted as $U_\pm = \pm 1_2$. For finite energy we again require $\lim_{|\boldsymbol{x}|\to\infty} U = U_\pm$. This choice of mass term then allows domain walls to exist as energy configurations, arising from the interpolation between the two vacua sates, namely $U_\pm$.

6.2 Skyrmion Formation Examples

Simulations of the nonlinear time-dependent PDE that follows from the variation of (5.2.2) were performed using a fourth order Runge-Kutta method on a grid of 101x101x101 grid points. We used Neumann boundary conditions (the spatial derivative normal to the boundary vanishes), which again allows the domain walls to move unhindered. We first simulate the proposed formation method of two incident domain walls. The initial conditions have to be more constrained than in the planar case and can be seen in figure 6.1. The addition of an extra field as well as an additional dimension, makes producing the correct winding quite challenging. The formation process can be observed in figure 6.2.

Note that as with the results in chapter 3 we are modelling a small area of a larger system and hence we observe a change in the topological charge. This would not occur in a true physical system as the winding here would be counteracted by some counter winding elsewhere in the system. However this simulation does demonstrate that it is possible (though requires a little more fine tuning), to produce Skyrmions from domain wall collisions in a similar fashion to the baby Skyrme model in chapter 3.

We now present a similar solution as the planar case, with multiple incident domain walls. Due to the additional difficulties in producing the correct winding, we have

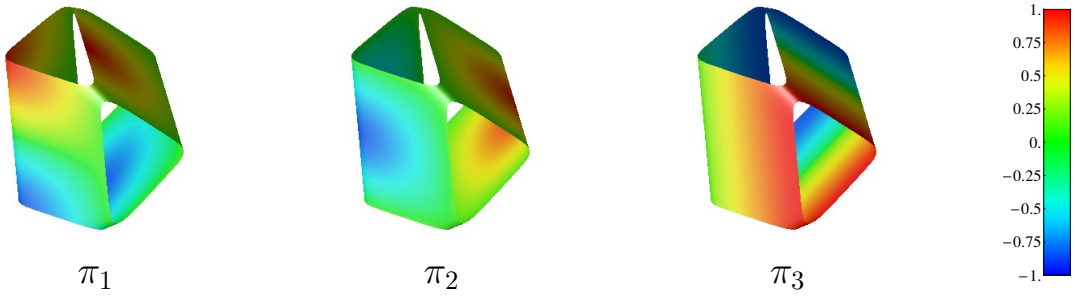

π_1 π_2 π_3

Figure 6.1: Initial conditions of two domain walls meeting, used to form a single soliton for the full $SU(2)$ Skyrme model, isosurface of $\sigma = 0$ with colours based on the value of π_1, π_2, π_3 respectively. The final panel shows the colourbar for the values each colour represents for the respective pion field.

used 6 domain walls, to produce the required affect, which can be seen in figure 6.3. This should be attainable using a fewer number of domain walls however the simulations are challenging to set up (partly this is due to the field not being able to change in the corner of the simulation with our chosen boundary conditions).

Finally, a $(3 + 1)$ domain wall system is extremely difficult to simulate. However the results should follow a similar form to the results presented for the $(2 + 1)$ dimensional system. The main difference is the increased difficulty in forming the correct conditions for the correct winding of all 3 fields. Though the increased computing power needed due to the additional spatial dimension is also somewhat restrictive.

6.3 Conclusions

We have demonstrated two situations in which Skyrmion solutions can be produced by domain wall interactions in the $(3 + 1)$-dimensional $SU(2)$ Skyrme model. We also demonstrated that using more than 2 domain walls, decreases the required constraints on the system for formation to occur. We haven't modelled the interactions of domain wall networks for 3 spatial dimensions, unlike the 2 dimensional case. It is likely that similar processes exist, but in a 3 dimensional analogue. It would be interesting to study a domain wall system in 3 dimensions, though numerically

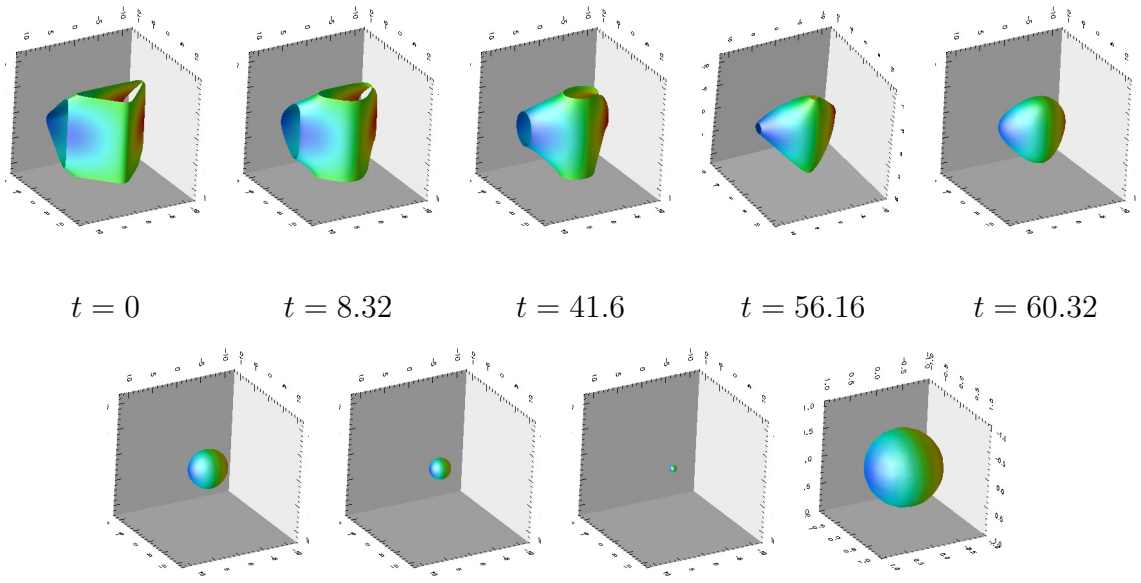

Figure 6.2: Simulation of two domain walls meeting to form a single soliton. The initial conditions (given in figure 6.1) are highly constrained. The plot is an isosurface of $\sigma = 0$ with colours based on the value of π_1 (colours match the colour bar in figure 6.1). The final panel is the resulting stable Skyrmion blown up so it is visible, the configuration matches the previous panel.

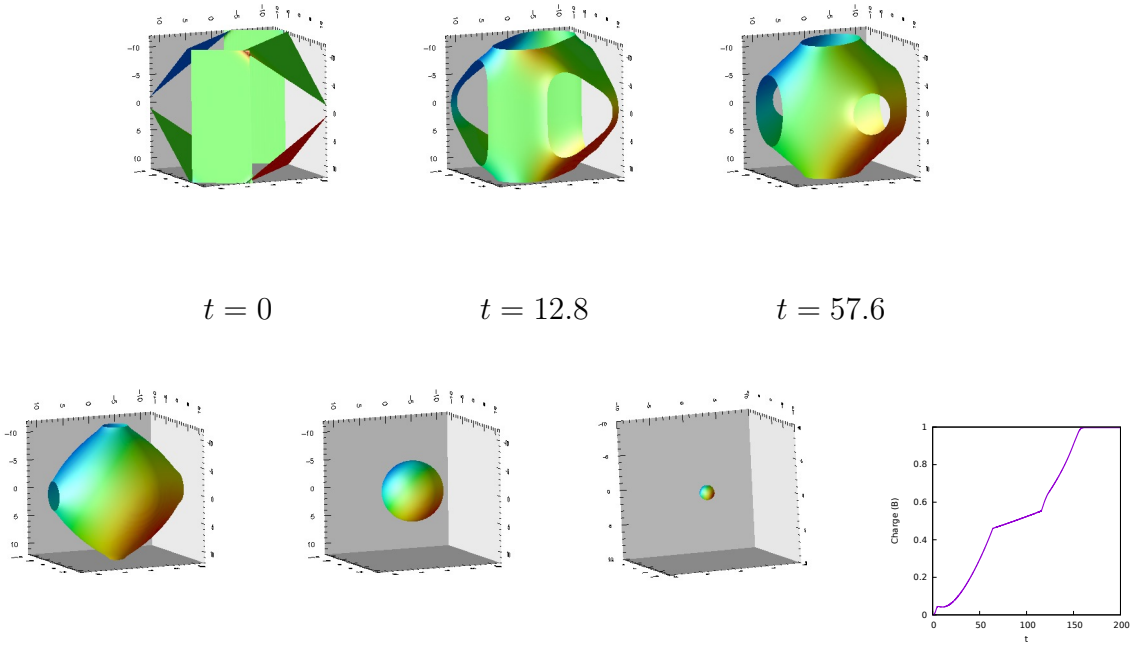

Figure 6.3: Isosurface plot for $\sigma = 0$ demonstrating 6 domain walls forming a single Skyrmion, coloured by the value of π_1. The topological charge is given in the final panel.

speaking it presents a number of challenges. Another interesting question to ask is, could Skyrmions be created by early phase transitions in the universe. Also might there be detectable features that winding may leave from such a process.

Chapter 7

Broken Skyrmions

7.1 Introduction

The Skyrme model has been obtained from quantum chromodynamics (QCD) [35, 37], and then more recently from holographic QCD, as a low-energy effective theory in the large colour limit [38]. The number of colours, N, appears only in the Skyrme model as a coefficient of the Wess-Zumino-Witten term. While this has an effect on the quantisation of Skyrmions, at the classical level it has no affect on the solutions and does not contribute to the energy.

Due to this it was proposed that a classical colour dependence could be introduced through the symmetry of the potential term. This was demonstrated for a 2-dimensional analogue by breaking the symmetry to the dihedral group D_N. This was considered for $N = 3$ static solutions [31] and later both statics and dynamics for both $N = 3$ and higher values of N [1]. In this chapter we present 3 possible potential terms that are similar to this 2-dimensional analogue. For the $(3 + 1)$-dimensional Skyrme model there is a subtlety, in that altering the potential term in such a way breaks the isospin invariance of the model. For a significant mass term, this will have a large affect on the form of the solutions.

The first potential we consider is a continuous deviation from the standard potential term, allowing the change in breaking the symmetries to be considered. The second potential is the Skyrme version of the 2-dimensional symmetry breaking term with symmetry groups D_N. Finally we propose some potentials that break the sym-

metry to polyhedral symmetry groups rather than the 2-dimensional dihedral groups from the 2nd potential.

7.2 Isospin Breaking

We will first try to consider how breaking the isospin invariance of the energy (8.2.2) will affect the form of the solitons. Some work has been done on this in [46], where a single pion field was given a mass $V = \pi_3^2$ and a 6^{th}-order in derivatives term was also included. This resulted in the single Skyrmion being able to be considered as two local positions of fractional winding.

We will consider the potential,

$$V = 2\left(\pi_1^2 + \pi_2^2 + \beta\pi_3^2\right), \tag{7.2.1}$$

where $\beta \geq 0$. This potential can be split into three regions:

- $\beta = 1$ - Gives the standard potential term $2\left(1 - \sigma^2\right)$, which retains the isospin invariance.
- $1 > \beta > 0$ - Breaks isospin symmetry giving the two fields π_1, π_2 as having a higher mass than the π_3 field. $\beta = 0$ gives π_3 as a massless field.
- $\beta > 1$ - Breaks isospin symmetry with the π_3 field being more massive than both π_1 and π_2. This is somewhat similar to the potential considered in [46], however we consider no sextic term.

For $\beta \neq 1$ this potential term breaks the $O\left(3\right)$ symmetry of the energy functional to an $O\left(2\right)$ symmetry, with two possible vacua for the model $\sigma = \pm 1$ (note this differs again with the model in [46] which has an $O(2)$ symmetry to it's vacua structure).

If we substitute the potential into the energy (8.2.2) and separate the radial terms, we can assume the energy is approximated by the rational map and a correction term,

$$E = \frac{1}{3\pi}\int\left(r^2 f'^2 + 2N\left(f'^2+1\right)\sin^2 f + \mathcal{I}\frac{\sin^4 f}{r^2} + 2m^2 r^2\left(1-\cos f\right)\right)dr$$
$$- \frac{m^2\left(1-\beta\right)}{6\pi^2}\int \pi_3^2 d^3x \tag{7.2.2}$$
$$= E_{standard} + E_{correction}. \tag{7.2.3}$$

If we assume the form of solutions will be similar to the rational map ansatz we can use the above functional to consider how deviating the value of β away from 1 will affect the solution. Namely we must consider how the field configuration will change due to minimising the correction term. One subtlety is that we must consider the optimal isorotation of the standard rational maps, as we have broken the invariance.

Numerical results were found using a fully dynamical 4^{th} order Runge-Kutta method, with 2^{nd} order finite difference approximations for the derivatives on a grid of 151x151x151 grid points throughout this chapter (unless stated otherwise).

7.2.1 $B = 1$

For charge $B = 1$, the standard rational map is $R = z$, which gives the familiar radial solution known as the hedgehog ansatz. This gives the standard pion fields to be

$$\sigma = \cos f(r), \quad \boldsymbol{\pi} = \sin f(r)\hat{\boldsymbol{x}}. \tag{7.2.4}$$

The pion field π_3 changes in one direction, interpolating from 0 at the origin back to 0 on the boundary. Note that an optimal isorotation is not needed, as it is equivalent to a spatial rotation for this ansatz.

The principle of symmetric criticality suggests that the charge 1 solutions should retain the maximal symmetry from both the energy functional and the space within which it is embedded. For $\beta = 1$ this leads us to the familiar hedgehog ansatz and a radial solution with $O(3)$ symmetry. For $\beta \neq 1$ this leads to a solution with $O(2)$ symmetry (likely to be easily attainable by simulating the evolution of the hedgehog ansatz).

Considering the correction term, it appears that as β is increased, the value of the field π_3 begins to dominate over the derivative of the field. Hence as β increases we should see the field π_3 changing quicker and thus the scale in this direction decreasing. Hence we expect the solution to be warped in the directions of the changing field π_3 decreasing the size in that direction but with increasing localisation of charge about the maximal values of the field $\pi_3 = \pm 1$.

Decreasing the value of β does the exact opposite, favouring the other two fields π_2 and π_3 with the scale increasing in the π_3 direction.

The numerical solutions can be seen in figure 7.1, this shows the solution being stretched/squashed in the direction of the field π_3 and hence agrees with the prediction layed out in the previous paragraph. One can see a plot of the field π_3 on a cross-section in the y-z plane in figure 7.2. A linear plot of the field π_3 in the z-direction is plotted in figure 7.3.

If we consider the profile of π_3 in the z-direction (maximal direction) we see the points of maximal value for the field decreasing in distance from the origin (not a surprise from the decreasing scale). The interpolation around these points increases its derivative as the mass term dominates. If we were to take the limit of this as $\beta \to \infty$ this would suggest that the maximal values lie at the origin with the field interpolating around it infinitely thin. This would suggest that the field has been reduced to a point at the origin but would also give the model to now act like the Skyrme-Faddeev model in that we have effectively performed a dimensional reduction of the target space.

7.2.2 $B = 2$

For charge $B = 2$, the standard rational map is $R = z^2$, giving a toroidal solution. There are two optimal isospin orientations to the rational map, depending upon whether β is greater or less than 1, given by

$$R(z) = \begin{cases} z^2 & \beta < 1 \\ \frac{iz^2+1}{-iz^2+1} & \beta > 1 \end{cases} \tag{7.2.5}$$

The standard solution is toroidal with the π_1, π_2 pion fields alternating around

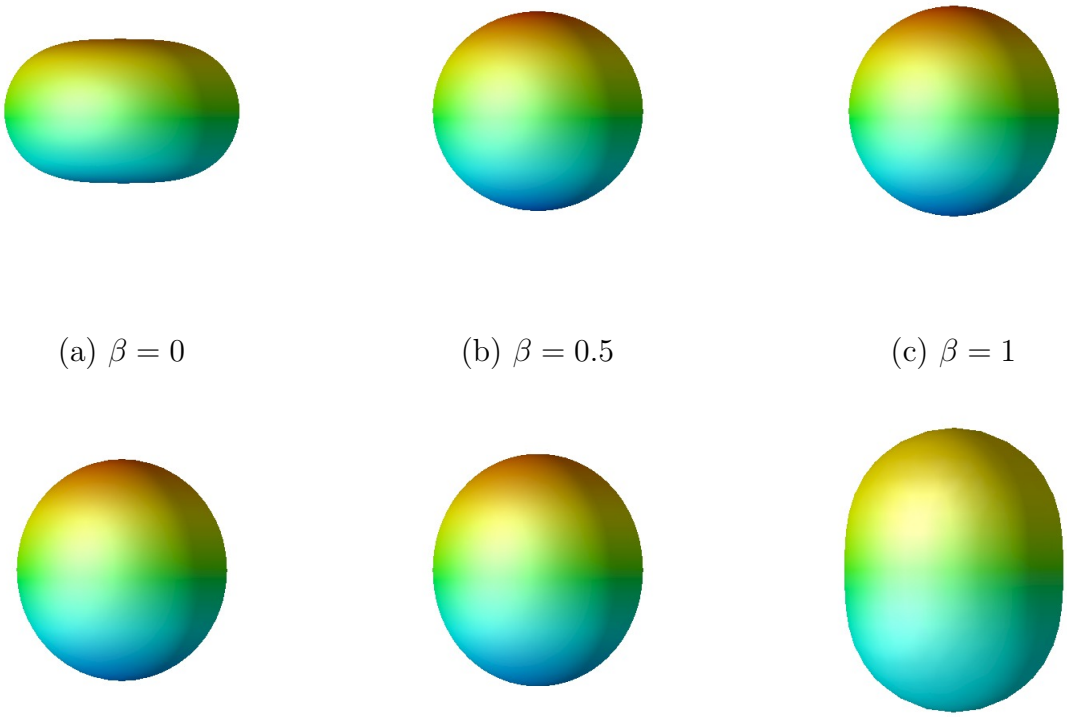

(a) $\beta = 0$ (b) $\beta = 0.5$ (c) $\beta = 1$

(a) $\beta = 1.5$ (b) $\beta = 2$ (c) $\beta = 5$

Figure 7.1: Energy isosurfaces of the shell like solutions with mass term (7.2.1) and parameters $m = 10$ for $B = 1$ with various values for β. The images are coloured based on the value of π_3. The solutions are being stretched/squashed in the direction of the changing field π_3. The numerical simulations were performed on a grid of size 151x151x151.

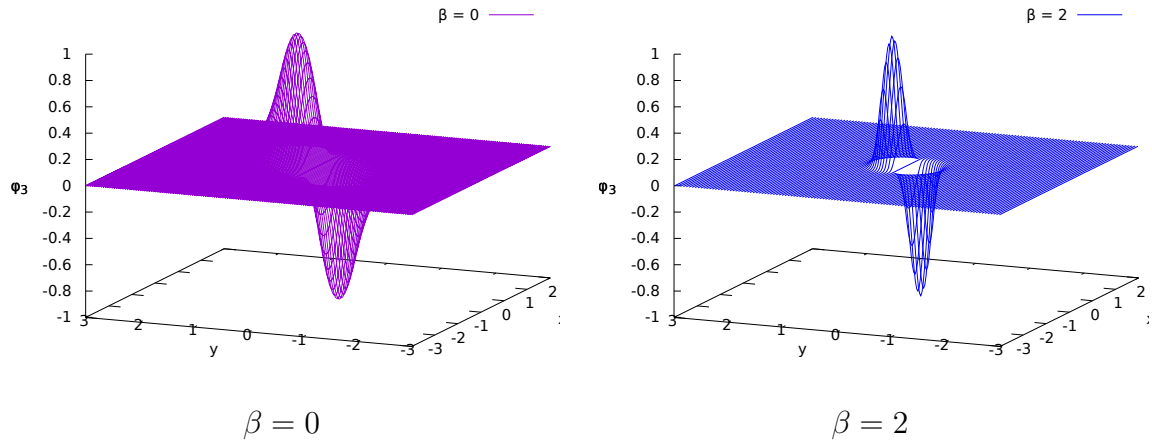

$\beta = 0$ $\beta = 2$

Figure 7.2: Plot of the field π_3 on a cross-section in the y-z plane, for two values of β. The field is becoming more localised around the values $\pi_3 = \pm 1$ for increasing β.

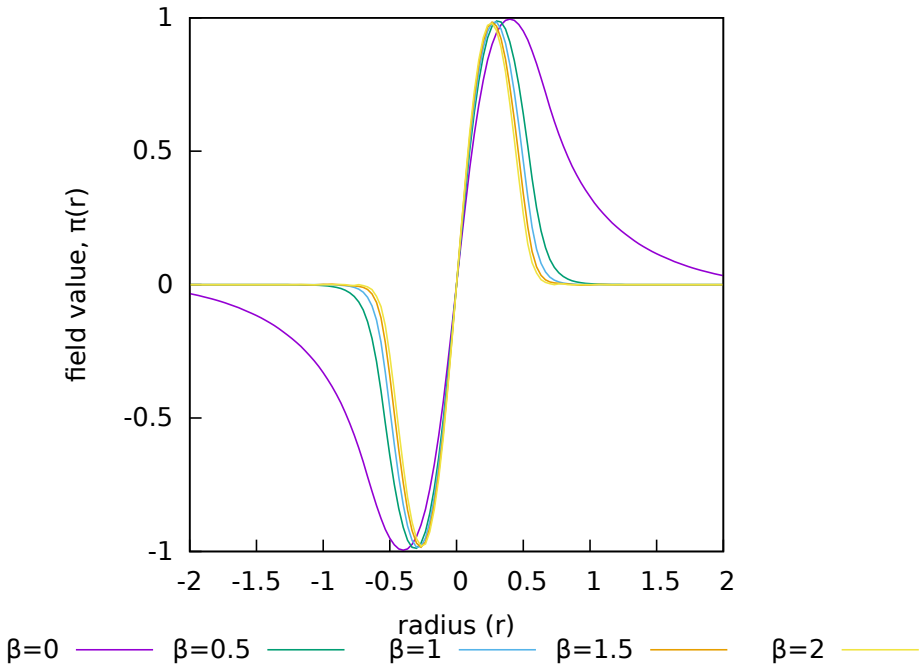

Figure 7.3: Plot of the field π_3 in the z-direction (the maximal direction for the field in the ansatz used (10.3.1)). Shows the field becoming more localised around the values $\pi_3 = \pm 1$ as β increases.

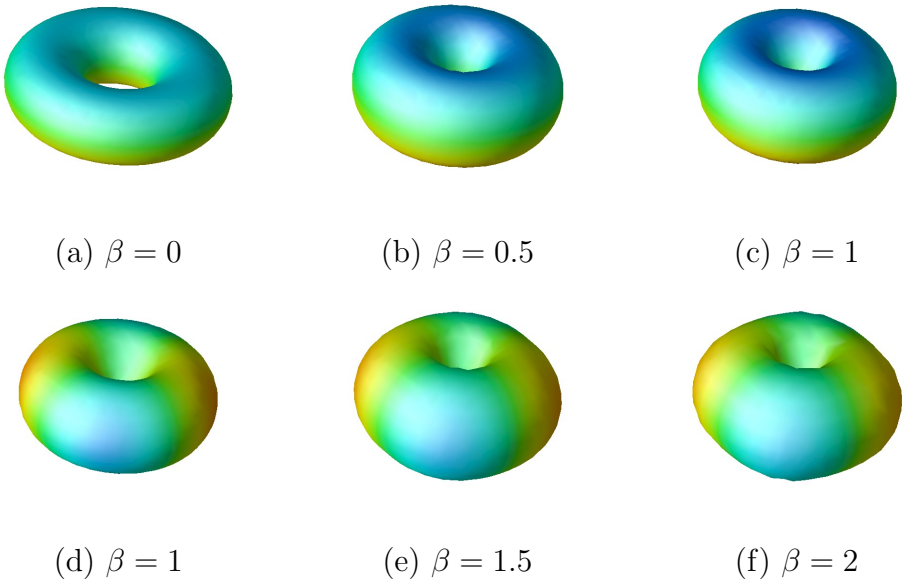

(a) $\beta = 0$ (b) $\beta = 0.5$ (c) $\beta = 1$

(d) $\beta = 1$ (e) $\beta = 1.5$ (f) $\beta = 2$

Figure 7.4: Energy isosurfaces of the shell like solutions with $m = 10$ for $B = 2$ with various values for β. The images are coloured based on the value of π_3. Note $\beta = 1$ is repeated for two different (though energetically equivalent) isorotations.

the loop of the torus, which traverses the target space twice for each physical period. The π_3 field alternates around the tube that forms the torus loop. The other rational map for $\beta > 1$ simply rotates the π_2 and π_3 fields such that the π_3 field now alternates around the loop of the torus.

Considering the correction term, the fields will no longer oscillate equally around the loop. The fields with a higher mass will want to spend a shorter time on their higher values, changing slower as they move through the smaller values, with the other field compensating accordingly and hence doing the opposite. It will also cause the charge to collate around the maximal values of the massive field.

The full field numerical solutions are presented in figure 7.4. Here we see that the optimal isorotation flips after $\beta = 1$ as predicted. We also observe a localisation of charge around the $\pi_3 = \pm 1$ points occurring for $\beta > 1$.

7.2.3 $B = 3$

For charge $B = 3$ the standard rational map has tetrahedral symmetry and is given by

$$R(z) = \frac{\sqrt{3}az^2 - 1}{z\left(z^2 - \sqrt{3}a\right)}, \tag{7.2.6}$$

with $a = \pm i$. It isn't clear what the optimal isorotation would be here and in fact it transpires that the rational map itself is isospin invariant. For the full field dynamics however we get some peculiar results. The tetrahedral form of the solutions starts to unwrap.

To explain this we take a short aside. An alternate rational map for the $B = 3$ solution is $R(z) = z^3$ which gives a toroidal solution, similar to the one discussed in the previous $B = 2$ section, but the torus circles the target space 3 times as it loops round in the physical space. This has a higher value for $\mathcal{I}$ and hence doesn't give the minimal energy rational map, however we can understand how this higher energy rational map can be deformed into the minimal energy tetrahedral map.

The $R(z) = z^3$ solution is much longer and hence more malleable than the $R(z) = z^2$ solution. We can use this by noting that similar points along the torus want to overlap to lower the energy of the soliton. We can link some of these points together giving the tetrahedral solution. Hence we can think of the $B = 3$ rational map as a single loop linked at certain points.

The effect of the broken isospin symmetry is to increase the charge density around certain points along the torus. However the lower mass fields want to have larger scale and tends to orient itself so it changes along the axis of the torus. Hence at some of the links, the lower mass field pushes the two points away from each other, forming a torus with the larger scale field alternating along the axis as predicted (though likely with a warped torus). This can be seen by comparing the full numerical results for increasing β in figure 7.5. Hence for $\beta = 0$, we suggest that the solution transitions from the traditional rational map form (7.2.6) for $m = 0$ to the toroidal form $R(z) = z^3$ for $m \to \infty$.

7.2.4 $B = 4$

The charge 4 solutions are fundamentally important in any model, as it tends to appear as the fundamental building block of massive solutions. Solutions that take the form of chunks of the crystal lattice are formed of multiple charge 4 Skyrmions,

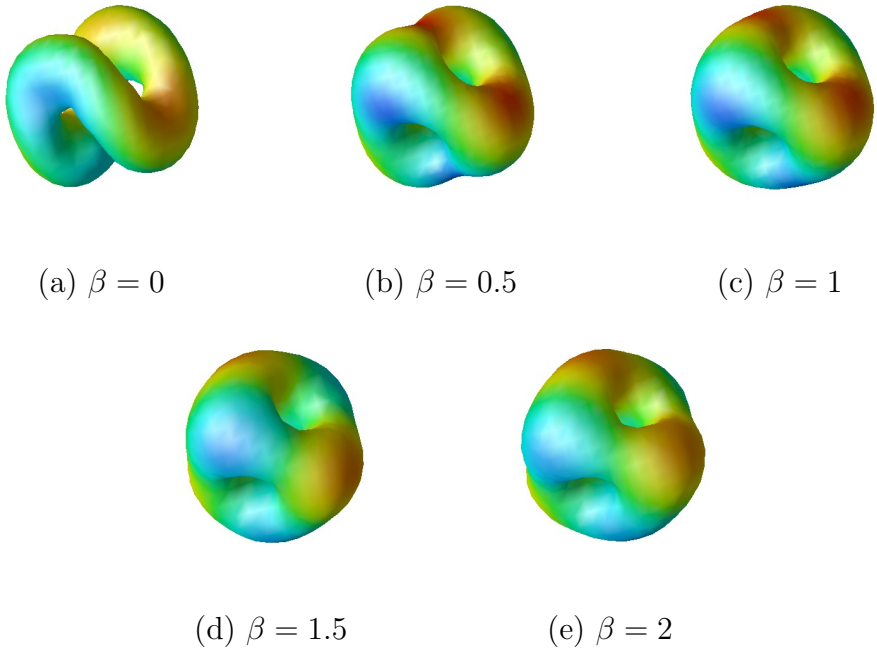

(a) $\beta = 0$ (b) $\beta = 0.5$ (c) $\beta = 1$

(d) $\beta = 1.5$ (e) $\beta = 2$

Figure 7.5: Energy isosurfaces of the shell like solutions with $m = 10$ for $B = 3$ with various values for β. The images are coloured based on the value of π_3.

in the form of a cubic lattice. It is the cubic symmetry that gives the charge 4 solution it's stability. The solution can also be considered as the combination of 2 charge 2 solitons stacked.

The minimal energy configurations resulting from full field theory simulations can be observed in figure 7.6. For low values of β the π_3 field wants more room to oscillate, hence the optimal isorotation alternates π_3 along the length of the solution which is stretched. Once $\beta > 1$ the field alters round one face, with the charge distribution localising around the maximal values as β increases.

7.2.5 $B > 4$

If we now consider all charges $B \leq 8$, we see a pattern emerging. This pattern prioritises the tori structure of solutions. The solutions for $\beta = 0$ are shown in figure 7.7, demonstrating this tori structure. If we consider the shell like solutions to be formed from a number of tori that contribute discrete amounts of topological charge each. These tori can then decrease their energy by linking at similar points.

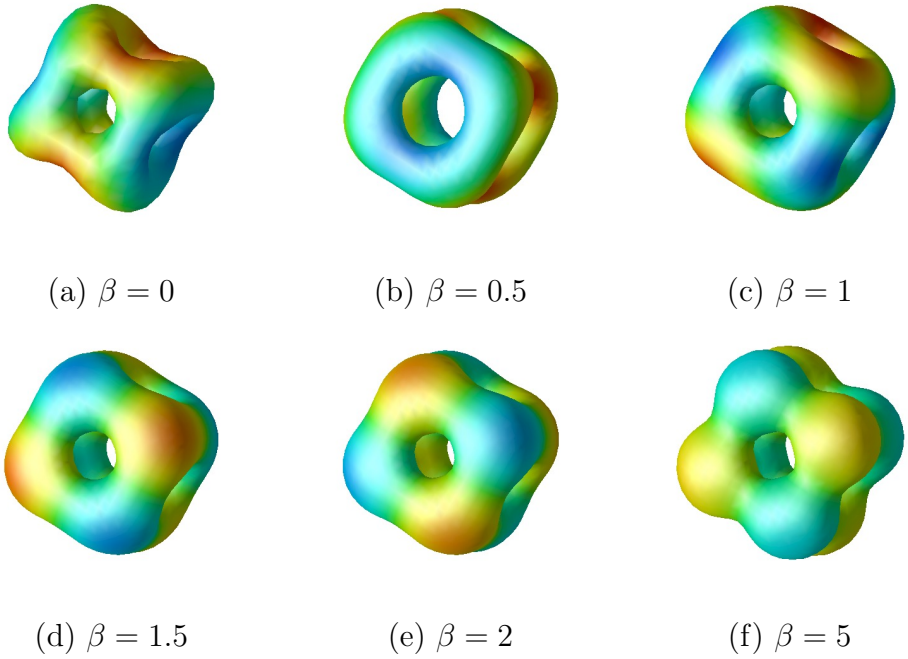

(a) $\beta = 0$ (b) $\beta = 0.5$ (c) $\beta = 1$

(d) $\beta = 1.5$ (e) $\beta = 2$ (f) $\beta = 5$

Figure 7.6: Energy isosurfaces of the shell like solutions with $m = 10$ for $B = 4$ with various values for β. The images are coloured based on the value of π_3.

There are two types of linking:

- *Self interacting* - Links between similar points on the same torus.
- *Interacting* - Links between similar points on multiple tori.

Within these categories the links can be subdivided again into

- *Head on* - The strands of the tori are linked together.
- *Stacked* - The tori are stacked one on top of the other as in the $B = 6$ solution.

If a self interacting link is head on, then it is merely forming a longer chain or splitting into smaller components. By breaking the isospin symmetry we have affected the stacked links. $B = 5$ has unwound and reduced the solution to its 5-ring structure. The charge 6 is shown to be formed from 3 $B = 2$ rings. In 7 the ring structure has been emphasised, but the head on links haven't been broken, forming a charge 3 torus intersected by 2 charge 2 tori. Finally the charge 8 minimal energy form is a 4-ring within two 2-rings.

We would predict that the shell like solutions for higher charges should continue to take this interacting ring form. It may seem peculiar that we say shell-like, but the solutions have retained their shell like structure. What may have changed however, is the shape of the shell.

The standard solutions for the Skyrme model can be thought of as similar to spheres with baby Skyrme like fields embedded on them [47]. If we extend this idea to the results presented here the sphere has been slightly stretched for certain solutions. If we consider $B = 6$ for example, the π_3 field alternates through the tori pushing them apart and hence stretching the surface over which the shell is formed. For other solutions, for example $B = 5$ the π_3 field pushes parts of the torus apart, however any distortion to the shell surface seems to be even in all directions or negligible, unlike the $B = 6$ solution.

7.3 Broken Potential

We now consider a potential that will break the global symmetry to the dihedral group D_N,

$$V = \left|1 - (\pi_1 + i\pi_2)^N\right|^2 (1 - \sigma)\,, \tag{7.3.1}$$

where $N \geq 2$ is an integer. We shall refer to this as the model with N colours. This is the 3-dimensional analogue of the potential proposed for the planar Skyrme model in [31] and expanded upon in [1]. The global symmetry is broken to the dihedral group D_N, generated by the rotation $(\pi_1 + i\pi_2) \to (\pi_1 + i\pi_2)\, e^{i2\pi/N}$ and the reflection $(\sigma, \pi_1, \pi_2, \pi_3) \to (\sigma, \pi_1, -\pi_2, \pi_3)$. This potential gives us $N + 1$ vacua on the 3-sphere. The vacuum at the north pole $U = 1_2$ will be chosen to be the vacuum at spatial infinity, with the remaining vacua occurring on an equatorial circle where $(\pi_1 + i\pi_2)^N = 1$.

Naturally we are most interested in $N = 3$ so as to model Baryon physics. The numerical solutions were obtained using a time dependent 4th-order Runge-Kutta method, cutting the kinetic energy whenever the potential increased.

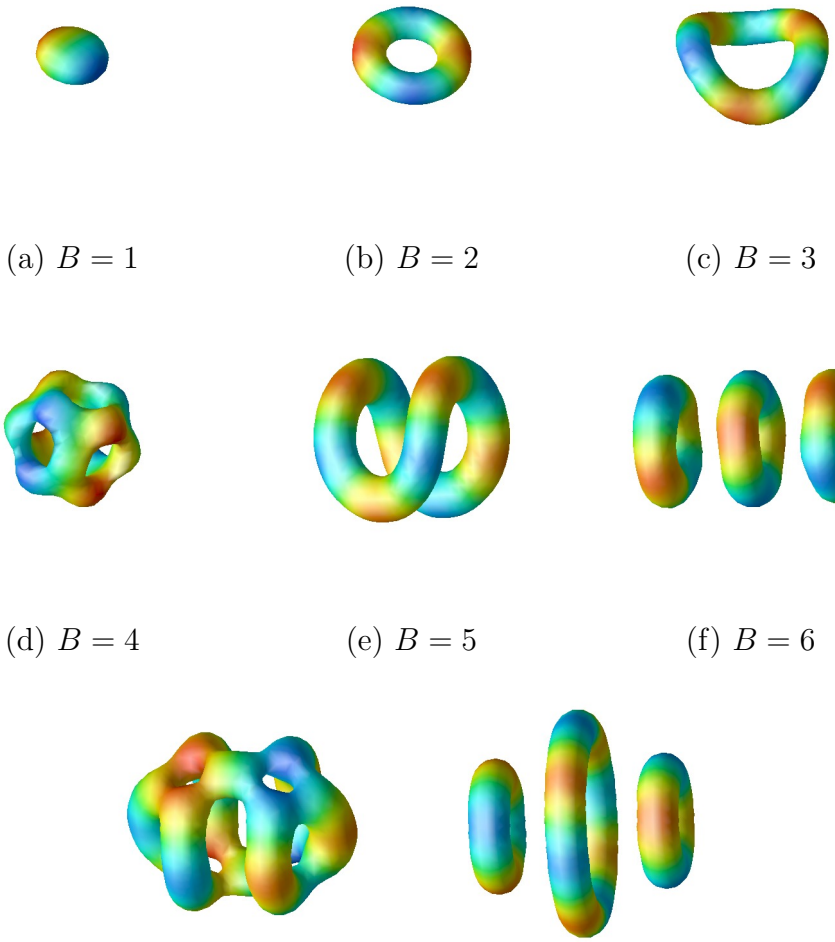

(a) $B = 1$ (b) $B = 2$ (c) $B = 3$

(d) $B = 4$ (e) $B = 5$ (f) $B = 6$

(g) $B = 7$ (h) $B = 8$

Figure 7.7: Energy isosurfaces of the shell like solutions with $m = 10$ and $\beta = 0$ for $B = 1 - 8$. The images are coloured based on the value of π_1. The simulation was performed on a grid of 151x151x151 points.

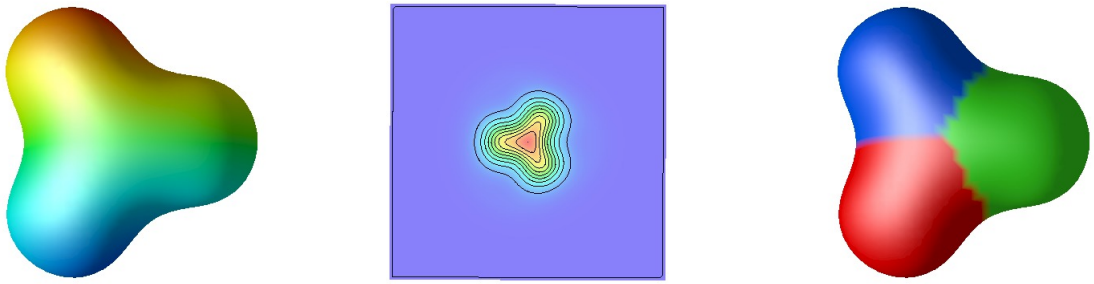

(a) π_1 (b) energy density (c) $\tan^{-1}(\pi_2/\pi_1)$

Figure 7.8: Plots for the minimal energy $B = 1$ solution (a) isosurface coloured based on the π_2 field. (b) a contour plot of the energy density on a cross-section with normal the z-axis (c) the same energy isosurface as (a), but coloured based upon $\tan^{-1}(\pi_2/\pi_1)$, or the segment of the target space.

7.3.1 Numerical Results

The solutions for $B = 1$ can be seen in figure 7.8, where we have plotted an isosurface of the resulting minimal energy solution as well as a planar cross-section. The cross-section (by choosing the plane on which the D_3 symmetry acts) gives a solution that is qualitatively similar to the minimal energy solutions for the broken baby Skyrmions model. We have also included an isosurface solution, coloured by the segment of the target space the point maps to (used for the remainder of the section). The target space is split into N sections using the value of the phase $\tan^{-1}(\pi_2/\pi_1)$. The boundaries are given by the radial line running through the N equatorial vacua, each segment is assigned a different colour in order to differentiate them.

The higher charge minimal energy solutions are presented in figure 7.9 with the solutions for $N = 4$ also supplied in figure 7.10. The minimal energy solutions can be interpreted easiest using the idea of modelling Skyrmions as baby Skyrmions embedded on a shell-like surface. In this model this result is particularly obvious, with the multi-soliton result being formed by shells of tiled polyforms, given by the broken baby Skyrme model. This can also be interpreted as single broken Skyrmions linked at the edges of their planar shape. This is the natural extension to the results

in chapter 4. Note that the way the single solitons cover the shells is different for $N = 3$ and $N = 4$.

It would appear that any local minima is likely to attempt to close the surface on which the planar polyforms are tiled. It would be interesting to consider if there is the multitude of local minima results consisting of tiling the polyforms together into a kind of "net" for the resulting shell.

7.4 Polyhedral Broken Skyrmions

Here the Broken potential above has been extended to polyhedral symmetries. The two symmetries considered here are tetrahedral (T) and octahedral (O). While for the dihedral potential the $N = 3$ case is the most interesting, there is still a place for higher values. Of course there is no longer any reason for the constituent partons to then conform to the limited dihedral symmetry of the previous potential. Hence the most obvious extension to this would be to consider potentials with polyhedral symmetries. The results, shown figures 7.11 and 7.12, are somewhat similar to the dihedral results, but with different symmetries to the constituent partons. The potentials used were,

$$V_T = \pi_1\pi_2\pi_3\left(1-\sigma\right), \tag{7.4.1}$$

$$V_O = \pi_1^2\pi_2^2\pi_3^2\left(1-\sigma\right). \tag{7.4.2}$$

7.5 Conclusions

We have considered breaking the isospin symmetry of the $SU(2)$ Skyrme model. The first potential we considered gave one of the fields an alternate pion mass, which lead to the tori structure of the model being promoted. This may be useful for considering the spin-orbit coupling, as one of the problems for orbiting a soliton configuration is the route that the orbiting soliton can take. The route must alternate the fields around a circle in the target space just as the constituent tori do.

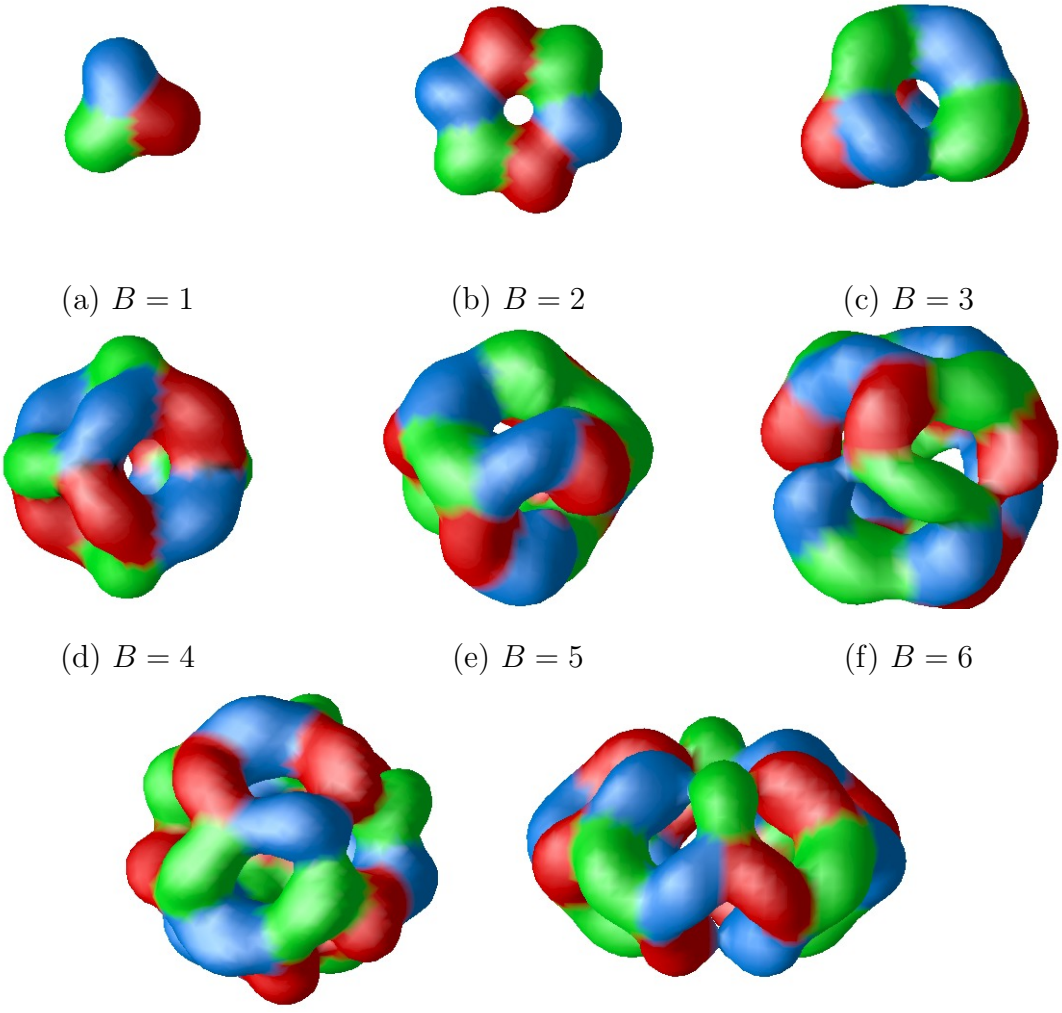

(a) $B = 1$ (b) $B = 2$ (c) $B = 3$

(d) $B = 4$ (e) $B = 5$ (f) $B = 6$

(g) $B = 7$ (h) $B = 8$

Figure 7.9: Energy isosurfaces of the shell like solutions for broken Skyrmions with $m = 10$ and $N = 3$ for $B = 1 - 8$. The images are coloured based on the segment of the target space.

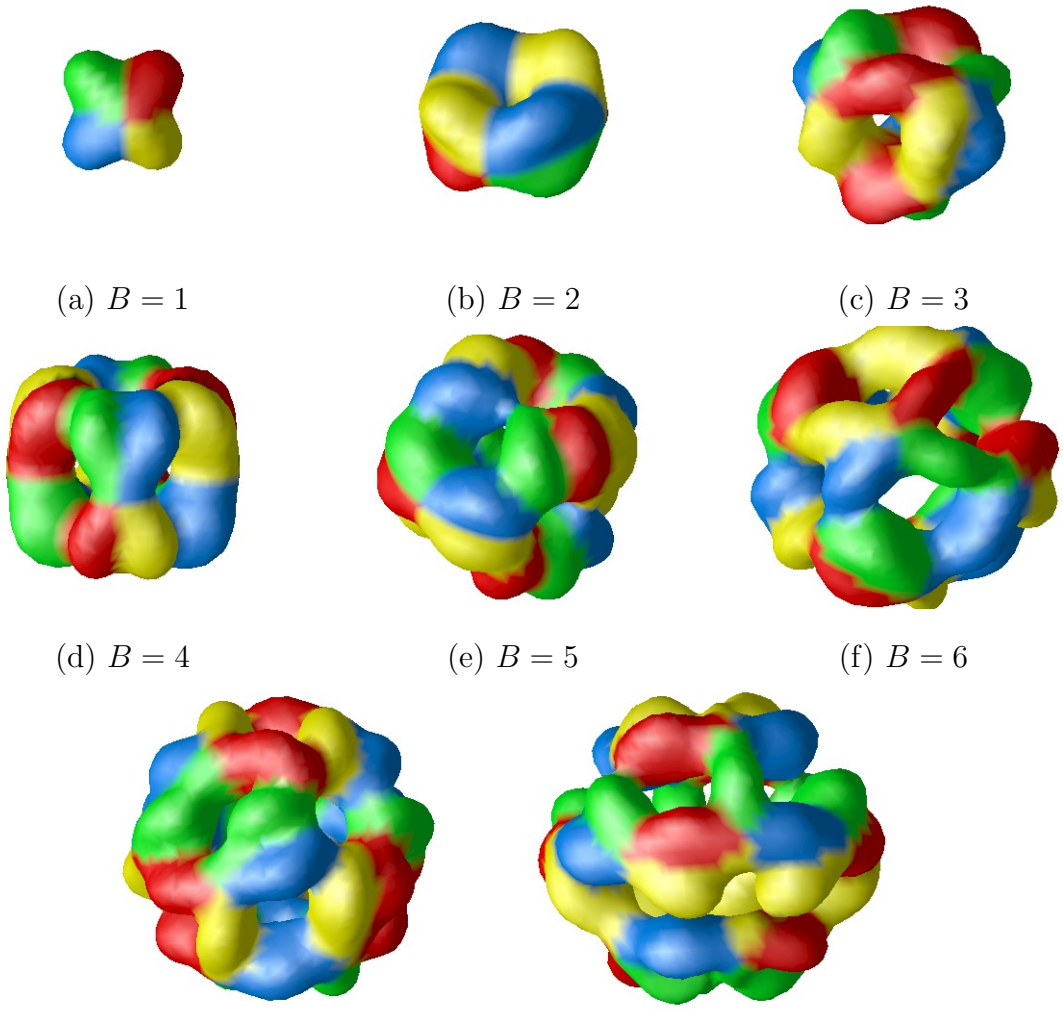

(a) $B = 1$ (b) $B = 2$ (c) $B = 3$

(d) $B = 4$ (e) $B = 5$ (f) $B = 6$

(g) $B = 7$ (h) $B = 8$

Figure 7.10: Energy isosurfaces of the shell like solutions for broken Skyrmions with $m = 10$ and $N = 4$ for $B = 1 - 8$. The images are coloured based on the segment of the target space.

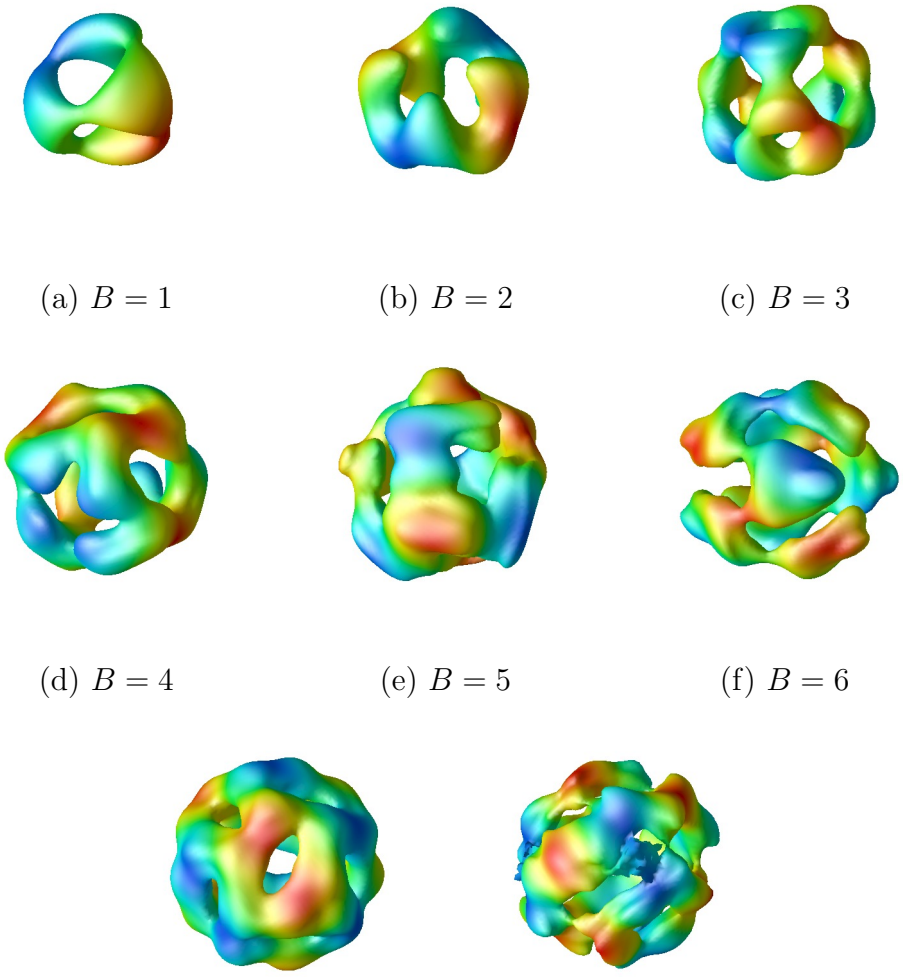

(a) $B = 1$ (b) $B = 2$ (c) $B = 3$

(d) $B = 4$ (e) $B = 5$ (f) $B = 6$

(g) $B = 7$ (h) $B = 8$

Figure 7.11: Energy isosurfaces of the shell like solutions with $m = 10$ for $B = 1 - 8$. The images are coloured based on the value of π_3. Has the mass term with tetrahedral symmetry

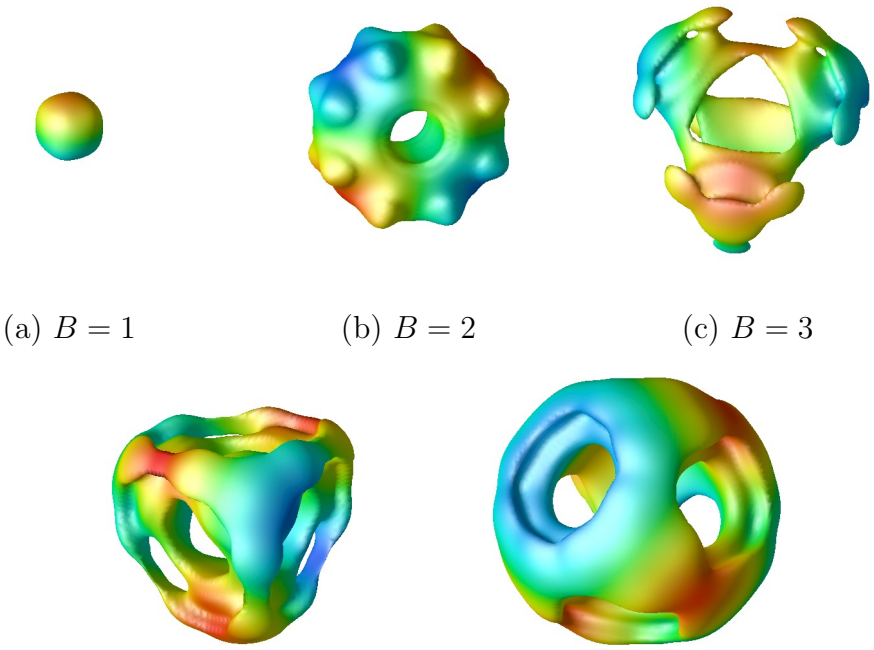

(a) $B = 1$ (b) $B = 2$ (c) $B = 3$

(d) $B = 3$ (different isosurface) (e) $B = 4$

Figure 7.12: Energy isosurfaces of the shell like solutions with $m = 10$ for $B = 1 - 4$. The images are coloured based on the value of π_3. Has the mass term with octahedral symmetry

Another aspect that was touched upon was the possibility of relating the broken models to hopfions in the Skyrme-Faddeev model. The introduction of a large disparity in the fields masses starts to favour ring like structures. It would be interesting to consider if some knotted forms could be introduced that became locally stable in some limit of the model. This may allow the introduction of a pseudo-hopf charge, that while not a true topological charge could identify certain locally stable solutions, with properties similar to the solutions of the Skyrme-Faddeev model.

We also considered some potentials with discrete symmetries in the form of the dihedral broken potential for various numbers of partons N and some polyhedral symmetries. This gave the expected results, in that single solitons took the form of N topologically confined partons, arranged in the symmetry selected for the potential. The higher charge solutions acted as the 3-dimensional extension to the broken baby Skyrmion model, namely single solitons placed about a shell-like structure, meeting at the edges of the polyform shape of the single solitons. These results suggest some obvious extensions for further work. Firstly it would be interesting to see if there is a multitude of local minima results, each corresponding to an alternate tiling of the 2D polyform into a net, that can then be formed into a shell solution. This may be easiest to consider by actually modelling the broken Skyrme results as broken baby Skyrmions embedded in S^2. Also the long range inter-soliton forces could be considered for general smooth potentials. This process has been performed for the planar model, but the introduction of an additional dimension introduces extra complications.

Finally it would be interesting to consider what the form of the lattice would be for these broken potentials. It is not clear what form this may take, unlike the planar model, where the tessellation of polyforms extends nicely to a lattice. The shell-like structure of solutions should break down for higher charges for broken Skyrmions, possibly leading to a more exotic form for the lattice solution.

Part IV

Hyperbolic and AdS space

Chapter 8

Hyperbolic Skyrmions

8.1 Introduction

In this section we will look at the $(3+1)$ $SU(2)$ Skyrme model embedded in Hyperbolic 3-space $\mathbb{H}^3_\kappa$ with general negative curvature $-\kappa^2$. The work is taken from the preprint [2] which has been submitted for publication.

The addition of a mass term has little effect on solutions of low baryon number in the Skyrme model, which continue to form shell like structures. However for larger charge solutions, a mass term starts to favour minimal energy solutions formed of finite chunks of a Skyrme crystal [42, 48, 49].

It has been demonstrated that there is a surprising similarity between Skyrmions with massive pions in Euclidean space and the massless case in hyperbolic space [50]. The cited paper also outlines a method for constructing Skyrmions with massive pions from instanton holonomies, by first modelling a hyperbolic Skyrmion by taking holonomies along particular circles in $\mathbb{R}^4$ [51] and applying a mapping relating hyperbolic curvature and Euclidean mass to produce the Euclidean Skyrmion [50].

This posits that there could be a geometrical underpinning to the standard mass term, traditionally used in the Skyrme model. This suggests that understanding Skyrmions in hyperbolic space and the affect that curvature has, may shed some light on Skyrmions with massive pions in Euclidean space. Most notably there are certain properties for Skyrmion solutions in Euclidean space, that only occur once the mass term is turned on, or exceeds a certain threshold. Namely, the formation of crystal

chunk solutions, as the global minimum, for higher charge systems that exceed the threshold mass. If some similar behaviour were to be observed for massless solutions in hyperbolic space, it would support this geometric link. In fact, it will be demonstrated that the map linking the curvature of hyperbolic Skyrmions with massive Euclidean solutions, can be used to predict the global minimum solution.

We will also examine the dynamics of Skyrmions in hyperbolic space, demonstrating that they scatter along geodesics, with maximally attractive channels corresponding to a relative rotation through an angle π, about an axis orthogonal to the connecting geodesic.

8.2 The Model

The Lagrangian density for an $SU(2)$ valued Skyrme field $U(t, \boldsymbol{x})$ is given by,

$$\mathcal{L} = -\frac{1}{2}Tr\left(R_\mu R^\mu\right) + \frac{1}{16}Tr\left(\left[R_\mu, R_\nu\right]\left[R^\mu, R^\nu\right]\right) - m_\pi^2 Tr\left(U - 1_2\right) \tag{8.2.1}$$

The associated energy for a static Skyrme field $U(\boldsymbol{x})$ defined on a general Riemannian manifold M with metric $ds^2 = g_{ij}dx^i dx^j$ is

$$E = \frac{1}{12\pi^2}\int\left\{-\frac{1}{2}Tr\left(R_i R^i\right) - \frac{1}{16}Tr\left(\left[R_i, R_j\right]\left[R^i, R^j\right]\right) + m^2 Tr\left(1 - U\right)\right\}\sqrt{g}d^3x \tag{8.2.2}$$

where g is the determinant of the metric. Note that both of the above expressions have the parameters preceding the first two terms scaled out.

Much work has been done on the solutions to this equation for Euclidean space $M = \mathbb{R}^3$ upto topological charge 108 [36, 49]. However we are interested in considering Skyrmion solutions in hyperbolic 3-space $M = \mathbb{H}^3_\kappa$, which is the space with constant negative curvature $-\kappa^2$. The metric of $\mathbb{H}^3_\kappa$ takes the form,

$$ds^2\left(\mathbb{H}^3_\kappa\right) = d\rho^2 + \frac{\sinh^2\left(\kappa\rho\right)}{\kappa^2}\left(d\theta^2 + \sin^2\theta d\phi^2\right), \tag{8.2.3}$$

where ρ is the hyperbolic radius. If we take the limit of zero curvature, we recover the Euclidean metric, with the hyperbolic radius equal to the standard Euclidean radius $\rho = r$. We will also make use of the standard Poincare ball model for

displaying results. This can be obtained from the above metric by a simple radial transformation $\rho = \frac{2\tanh^{-1}(\kappa R)}{\kappa}$, to give the following metric,

$$ds^2\left(\mathbb{H}^3_\kappa\right) = \frac{4\left(dR^2 + R^2\left(d\theta^2 + \sin^2\theta d\phi^2\right)\right)}{\left(1-\kappa^2R^2\right)^2}. \tag{8.2.4}$$

Hence our space can be modelled by a sphere with a boundary at infinite hyperbolic radius given by $R = \frac{1}{\kappa}$ (though our plots will always be scaled to an equivalent size).

The vacua for the massless theory is any constant U, however the inclusion of the mass term $m > 0$ gives the unique vacuum to be $U = 1_2$. We will impose the boundary condition $U \to 1_2$ as $\rho \to \infty$, which is required for finite energy. This gives us a map $U : \mathbb{H}^3_\kappa \cup \{\infty\} = S^3 \to S^3$, and hence a topological charge as an element of the 3rd homotopy group, equivalent to an integer $B \in \pi_3(S^3) = \mathbb{Z}$,

$$B = -\frac{1}{24\pi^2}\int \epsilon_{ijk} Tr\left(R_i R_j R_k\right) d^3x. \tag{8.2.5}$$

8.3 Approximations

There are a few approximations for Skyrmions with massless and massive pions. The rational map approach will be the most useful in this chapter. The angular dependence of the solution is approximated to be a rational map between Riemann spheres [41]. On extension to massive pion solutions, it is found that only shell-like approximations can be closely approximated. While multi-shell like solutions have been modelled in an attempt to form more crystal like solutions [52], they are poor approximations to the full minimal energy solutions. They can be useful for initial conditions in numerical simulations however.

8.3.1 B=1

In Euclidean and hyperbolic space the single Skyrmion solution can be reduced to solving an ODE, using the hedgehog ansatz. This is known as a hedgehog solution due to its radial nature, as can be seen in figure 8.1. The field is given to be

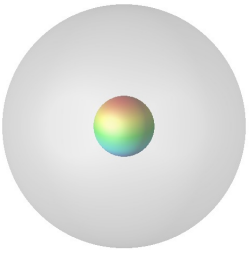

(a) energydensity plot

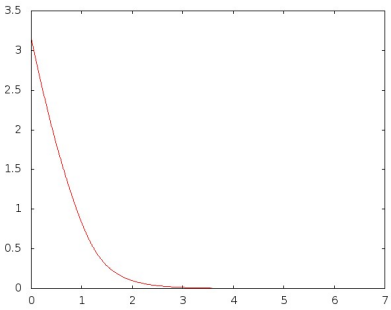

(b) profile function $f(\rho)$ ($\kappa = 1$,$m = 0$)

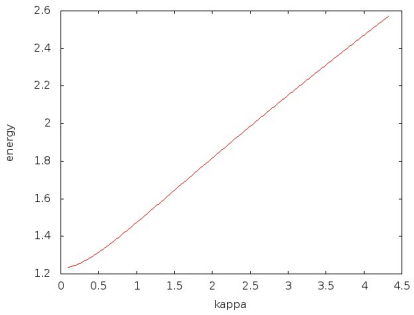

(c) energy for increasing curvature ($m = 0$)

Figure 8.1: $B = 1$ static hedgehog solution, (a) energy density plot in Poincaré ball, where the grey shaded region represents the boundary of hyperbolic space, (b) profile function $f(\rho)$ for $\kappa = 1$, $m = 0$, (c) energy for increasing curvature, for $m = 0$.

$$U = \exp\left(if\left(\rho\right)\hat{\boldsymbol{x}}\cdot\boldsymbol{\tau}\right), \tag{8.3.1}$$

where $\hat{\boldsymbol{x}} = (\sin\theta\cos\phi, \sin\theta\sin\phi, \cos\theta)$ is the unit vector in Cartesian coordinates, $f(\rho)$ is a monotonically decreasing radial profile function with boundary conditions $f(0) = \pi$ and $f(\infty) = 0$. Substituting this into the energy in (8.2.2) we get a radial energy of the form,

$$E = \frac{1}{3\pi}\int\left(f'^2\frac{\sinh^2\kappa\rho}{\kappa^2} + 2\left(f'^2+1\right)\sin^2 f + \frac{\kappa^2\sin^4 f}{\sinh^2\kappa\rho} + 2m^2\frac{\sinh^2\kappa\rho}{\kappa^2}\left(1-\cos f\right)\right)d\rho \tag{8.3.2}$$

The profile function $f(\rho)$ can then be found by minimising the above energy and is also shown in figure 8.1 for $\kappa = 1$,$m = 0$. This yields a function with an exponential asymptotic decay for $m = 0$,

$$f \sim Ae^{-2\kappa\rho}. \tag{8.3.3}$$

This takes a similar form to that of massive Euclidean Skyrmions ($\kappa = 0$) $f \sim \frac{A}{r}e^{-mr}$, but dependent on the curvature rather than the mass of the theory. This suggest a relation between curvature and mass. In fact it is found that if the correct

curvature is selected, one can produce an extremely similar profile function for any Skyrmion with massive pions in Euclidean space. See [50] to observe the graph showing the relation between κ and m.

8.3.2 Shell-like multisolitons

Shell-like solutions can be well approximated by the rational map ansatz. In hyperbolic space this takes the following form,

$$U(\rho, z) = exp\left[\frac{if(\rho)}{1+|R|^2}\begin{pmatrix} 1-|R|^2 & 2\bar{R} \\ 2R & |R|^2-1 \end{pmatrix}\right] \tag{8.3.4}$$

where $z = e^{i\phi}\tan\left(\frac{\theta}{2}\right)$ is the Riemann sphere coordinate and $R(z)$ is a degree B rational map between Riemann spheres. Substituting this ansatz into (8.2.2) we get the following radial energy,

$$E = \frac{1}{3\pi}\int\left(f'^2\frac{\sinh^2(\kappa\rho)}{\kappa^2} + 2B\left(f'^2+1\right)\sin^2 f + \mathcal{I}\frac{\kappa^2\sin^4 f}{\sinh^2(\kappa\rho)} + 2m^2\frac{\sinh^2(\kappa\rho)}{\kappa^2}(1-\cos f)\right)d\rho, \tag{8.3.5}$$

where

$$\mathcal{I} = \frac{1}{4\pi}\int\left(\frac{1+|z|^2}{1+|R|^2}\left|\frac{dR}{dz}\right|\right)^4\frac{2idzd\bar{z}}{\left(1+|z|^2\right)^2}. \tag{8.3.6}$$

$\mathcal{I}$ is an integral to be minimised by the choice of rational map $R(z)$. Note that $\mathcal{I}$ is independent of κ and hence the values match those in Euclidean space. The minimal values of $\mathcal{I}$ and the associated rational maps can be found in [36] for a range of values of B. Note that the earlier hedgehog ansatz is recovered for $B = 1$, where $R = z$ is the minimising map, with $\mathcal{I} = 1$ and (8.3.5) reduces to (8.3.2).

This approximation will be used in various ways to form initial conditions for the numerical computations presented later. We will also investigate how curvature affects the accuracy of the approximation.

8.4 Static Solutions

8.4.1 Shell-like Static Solutions

The static equations that follow from the variation of (8.2.2) were solved using a time dependent 4th-order Runga-Kutta method to evolve the time-dependant equations of motion that follow from the relativistic Lagrangian (8.2.1), cutting the kinetic energy whenever the potential increased. The grid was modelled using the Poincaré ball model of radius κ^{-1} on a cubic grid with $(201)^3$ grid points and lattice spacing (for the standard $\kappa = 1$) $\Delta x = 0.005$. Spatial derivatives have been approximated using a 4th-order finite difference method. We must fix the boundary at $R = \kappa^{-1}$ to be the vacuum at spatial infinity $U_\infty = \mathbf{1}_2$, to ensure finite energy. For all our simulations the topological charge, when computed numerically, gives an integer value to five significant figures, indicating the accuracy of the results.

Two forms of initial condition were considered. The rational map ansatz shown in (8.3.4) and the product ansatz $U(\boldsymbol{x}) = U_1(\boldsymbol{x})\, U_2(\boldsymbol{x})$, which was used to place lower charge solitons at various well separated positions about the grid.

The first eight shell-like static solutions for $\kappa = 1, m = 0$ can be seen in figure 8.2. These solutions take a similar form to the Euclidean solutions of the same charge, with a few subtle differences. The faces of the polyhedron now appear to take the form of geodesic surfaces (a surface that contains curves belonging to the set of geodesics within the global space). Additionally, translating the solutions about the grid alters the apparent shape and means that lines of symmetry fall along geodesics of the space. This can be seen in more detail in the analysis of the $B = 8$ solution in figure 8.5. The crystal chunk solution clearly demonstrates a bowing of the line connecting the two $B = 4$ solitons, this line is found to be a geodesic of the space.

If we look at the energies displayed in table 8.1 we can see the expected trend in energies for increasing charge. We also observe how the energy of a given charge solution scales with curvature in figure 8.3.

We now compare the approximation from the rational map ansatz to the minimal energy solution for topological charges $B = 1$ to 8. The results for $B = 2$ can be observed in figure 8.4. We note that the rational map gives a very good approx-

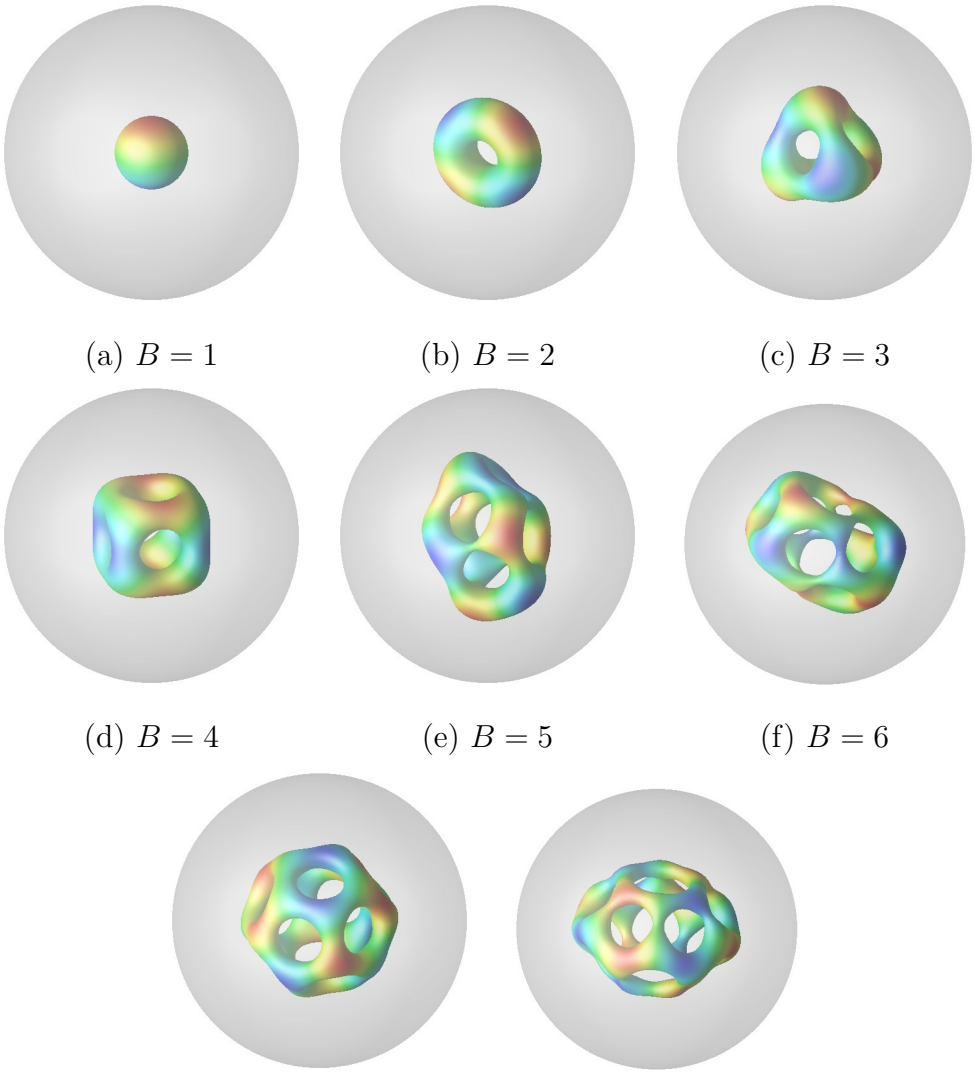

(a) $B = 1$ (b) $B = 2$ (c) $B = 3$

(d) $B = 4$ (e) $B = 5$ (f) $B = 6$

(g) $B = 7$ (h) $B = 8$

Figure 8.2: Energy isosurfaces of the shell like solutions with $\kappa = 1, m = 0$ for $B = 1 - 8$. The images are coloured based on the value of π_2 and the grey sphere represents the boundary of space in the Poincare ball model.

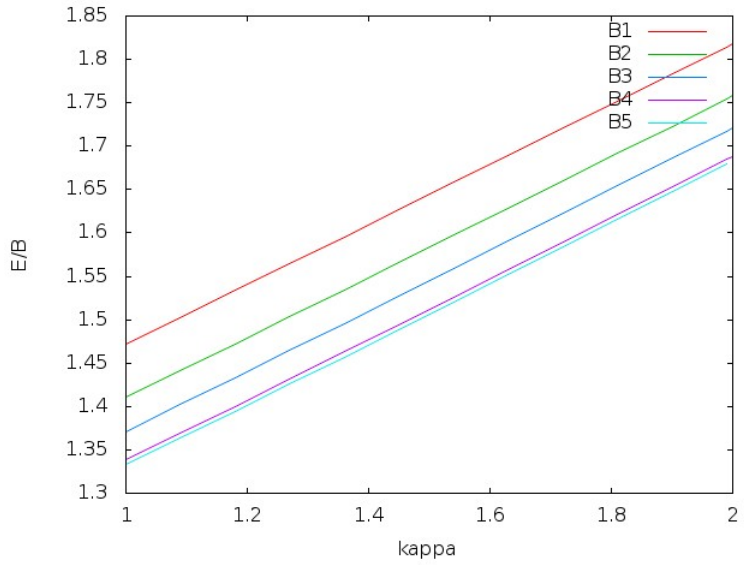

Figure 8.3: A plot of the energy for charge $B = 1 - 5$ shell like solutions against κ

imation up to $B = 4$. The fraction E_R/E, where E_R is the energy of the rational map approximation and E is the full numerical minimal energy, seems to stay relatively constant throughout an increase in curvature. We can't say if this trend will definitely continue, however if it does, then the rational maps will remain a good approximation for all values of curvature, as long as the solutions are shell-like, but the rational map approximation breaks down if the solutions begin to become non shell-like.

8.4.2 Crystal chunk Solutions

For the crystal chunk solutions we will consider a couple of cases, the $B = 8$ and 32 solutions. In Euclidean space we find that the $B = 8$ solution needs a relatively high mass for the crystal chunk solution to become the global minimum. This massive solution can be considered to be two $B = 4$ Skyrmions, joined along an axis perpendicular to a face of the shape. They have relative rotation of $\frac{\pi}{2}$ around the axis joining the two solitons.

In figure 8.5 we observe that both the crystal chunk and shell-like solutions are attainable in hyperbolic space with $\kappa = 1$. However, it appears that the crystal solution is the global minimum for all non-zero curvatures considered. Note that

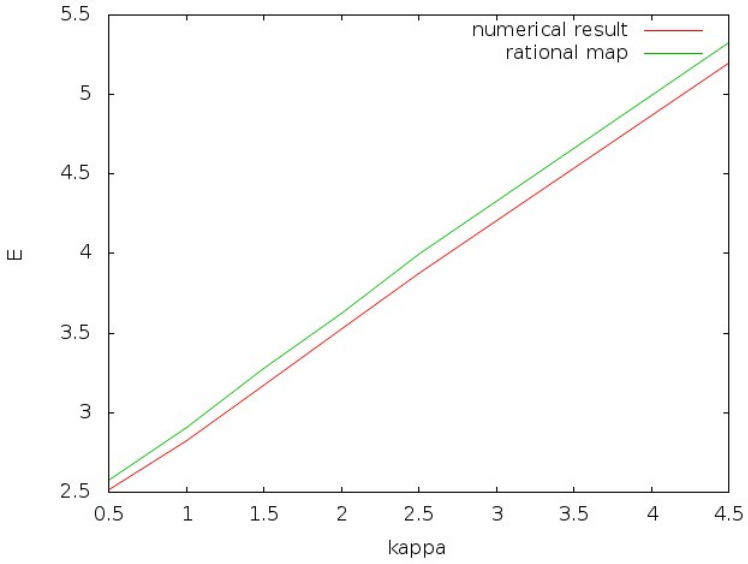

Figure 8.4: The numerical result of the energy compared to the rational map approximation for $B = 2$, for various value of κ. If one considers the percentage of the approximation that the numerical result takes, it remains roughly constant within our numerical error.

Table 8.1: The energy for soliton solutions (E) and rational map ansatz (E_R) with $\kappa = 1, m = 0$

B	E	E/B	E_R	E_R/B	% difference	figure
1	1.47	1.47	1.47	1.47	0	8.2(a)
2	2.82	1.41	2.90	1.45	2.9	8.2(b)
3	4.11	1.37	4.27	1.42	3.9	8.2(c)
4	5.36	1.34	5.46	1.36	1.9	8.2(d)
5	6.66	1.33	6.89	1.38	3.4	8.2(e)
6	7.84	1.31	8.20	1.37	4.6	8.2(f)
7	9.14	1.31	9.29	1.33	1.6	8.2(g)
8	10.29	1.29	10.73	1.34	3.9	8.2(h)

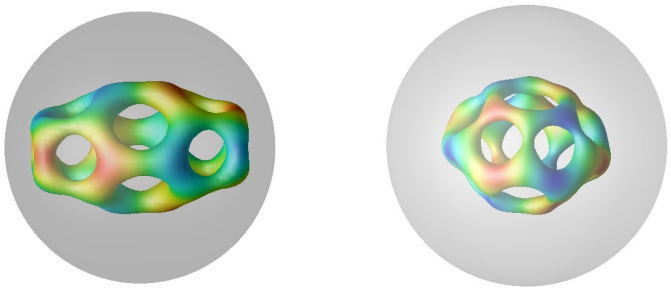

(a) cyrstal-chunk solution (b) shell-like solution

Figure 8.5: $B = 8$ static solution, (a) energy density plot of the crystal chunk solution with $\kappa = 1$, $m = 0$, (b) energy density plot of the shell-like solution with $\kappa = 1$, $m = 0$

the energies of the two solutions get very close and could be within numerical error of each other. The $B = 8$ crystal chunk solution is the lowest charge crystal solution and hence the energy difference might not be discernible with our accuracy. It is possible that the non-shell like solution does in fact become the minimal energy solution, for higher values of the curvature. We will consider a higher charge solution where the energy difference will be more discernible. Also, if the crystal chunk solutions act as with increasing the mass term in Euclidean space, we may find that the crystal chunk solution would become the minimal energy solution for a lower curvature.

The $B = 32$ crystal chunk solution, displayed in figure 8.6(b-c), has a far lower energy than that of the shell like solution in figure 8.6(a) for even low values of κ. This is also the case for a small mass term in the Euclidean model. Hence we have demonstrated that not only are the profile functions related for Skyrmions with massive pions in Euclidean space and with massless pions in hyperbolic space, but the energetically favourable form of solution is also similar.

8.5 Dynamics

The solutions to the time-dependant equations of motion that follow from (8.2.1) were again found using a time dependent 4th-order Runga-Kutta method. The grid

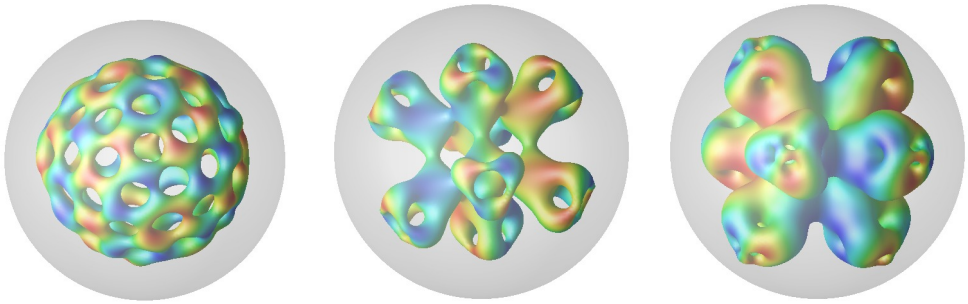

(a) $B = 32$ (b) $B = 32$ (c) $B = 32$

Figure 8.6: Energy density plots of the multi-soliton solution for $B = 32$ for various isosurface values, coloured based on π_2 value for (a) shell like solution with energy 40.43, (b-c) crystal chunk solution with energy 38.22.

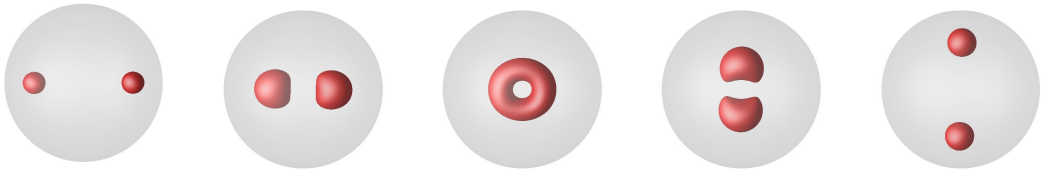

Figure 8.7: Scattering along a geodesic through the origin, with zero initial velocity, with solitons in the attractive channel (relative rotation of π around a line perpendicular to the diagonal).

was modelled using the Poincaré ball model of radius 1 (fixing $\kappa = 1$) on a cubic grid with $(201)^3$ grid point, hence the lattice spacing $\Delta x = 0.005$. Spatial derivatives have been approximated using a 4th-order finite difference method. The product ansatz was used for well separated single charge solitons.

The simplest situation to consider is scattering along a geodesic that passes through the centre of the space, as seen in figure 8.7. This gives a straight geodesic, with a clear parallel to Euclidean space and hence an obvious attractive channel (rotate relative by π around an axis perpendicular to the connecting straight line). The scattering process then proceeds as expected with the solitons scattering at $\pi/2$.

Due to hyperbolic translations (elements of the isometry group of hyperbolic space) one would expect in general, single Skyrmions to follow geodesics until they scatter. After scattering, the emerging Skyrmions will follow alternate geodesics,

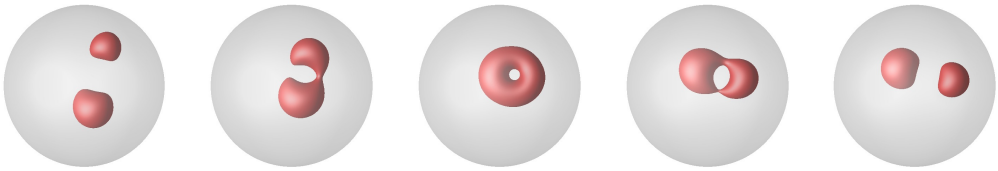

Figure 8.8: Scattering along a curved geodesic, with zero initial velocity, in the attractive channel (relative rotation of π around a line perpendicular to the geodesic).

oriented to the incident paths by a rotation of π around an orthogonal axis. The maximal channel will be a rotation of one of the solitons relative to the other by π around an orthogonal axis to the tangent of the connecting geodesic. On scattering, the Skyrmions should merge to form the standard $B = 2$ solution, oriented to lie in the incident plane, however it may appear deformed due to the curvature of the space. The results presented here confirm these expectations and can be observed in figure 8.8.

8.6 Conclusions

We have found both static and dynamic solutions for hyperbolic Skyrmions of various curvature. The static solutions have been related to massive solutions in Euclidean space, by making use of the relation shown in [50]. It has been demonstrated that the link between curvature in hyperbolic space and mass in Euclidean space extends to full solutions of various topological charge, allowing predictions to be made for the type of solution that will occur in the two models.

We have supplied evidence that suggests the rational map approximation is a good approximation for increasing curvature. It seems to retain its accuracy regardless of the curvature considered. This would suggest that we can model Skyrmion solutions in the infinite curvature limit, by using their respective rational maps. This is analogous to the hyperbolic monopole case, where solutions for infinite curvature become rational maps [53]. It would be interesting to see if there were some interesting limit in which it produces exact solutions, that in some way corresponds to hyperbolic monopoles.

The dynamics of various soliton initial conditions have also been studied. The

attractive channel was shown to be a relative rotation by π around an axis orthogonal to the connecting geodesic.

It would be interesting to consider the form of a soliton crystal in hyperbolic space, due to the interesting symmetries and tilings that can be formed from various polyhedron. It would be sensible to start with the 2-dimensional analogue, due to the difficulty of the task. Some similar work has been done with 2-dimensional vortices in the hyperbolic plane, concentrating on the tiling with Schläfi symbol $\{8, 8\}$ [54].

Chapter 9

Hyperbolic Baby Skyrmions

9.1 Introduction

In this chapter we consider the Baby Skyrme model in $(2+1)$ dimensions with the background of hyperbolic 2-space $\mathbb{H}^2$, the work in this chapter is intended to appear in a paper and is in progress. It may seem peculiar to consider the planar model when we have already found many results for the full Skyrme model in $\mathbb{H}^3$. However our main interest is in considering Skyrme crystals, or tessellating configurations, which we didn't find any results for in the full model. We have done some work on these in $\mathbb{R}^2$ in part 2, but hyperbolic space brings many more complications that will be discussed later.

9.2 The Model

The baby Skyrme model on a general 2-dimensional manifold M with metric $ds^2 = g_{ij}dx^i dx^j$ has the familiar static energy,

$$E = \int \left(\frac{1}{2}\partial_i \boldsymbol{\phi} \cdot \partial^i \boldsymbol{\phi} + \frac{k^2}{4} \left(\partial_i \boldsymbol{\phi} \times \partial_j \boldsymbol{\phi}\right) \cdot \left(\partial^i \boldsymbol{\phi} \times \partial^j \boldsymbol{\phi}\right) + m^2 \left(1 - \phi_3\right) \right) \sqrt{g}\, \mathrm{d}^2\mathbf{x}. \tag{9.2.1}$$

Note, for this chapter we have used the latin letter k for the coefficient of the Skyrme term. The standard is to use the greek letter κ, however this could be

confusing, as this was previously used as the Gaussian curvature of hyperbolic space. The metric we are interested in for this section is the hyperbolic metric, presented here in the Poincare model,

$$ds^2 = 4\frac{dx^2 + dy^2}{\left(1 - r^2\right)^2}, \tag{9.2.2}$$

where $r = \sqrt{x^2 + y^2}$ and gives a space with constant negative curvature -1. The Poincare model is the optimal model for presenting our results as it is easiest to observe symmetries and tessellations of the space. The space is visualised on a unit disc embedded in flat space, with the boundary $r = 1$ representing the boundary at infinity of the space, where every point has infinite distance from all others. The geodesic distance between two arbitrary points in the space $\boldsymbol{x}$ and $\boldsymbol{y}$ is given by,

$$d\left(\boldsymbol{x}, \boldsymbol{y}\right) = \cosh^{-1}\left(1 + \frac{2\left|\boldsymbol{x} - \boldsymbol{y}\right|^2}{\left(1 - \left|\boldsymbol{x}\right|^2\right)\left(1 - \left|\boldsymbol{y}\right|^2\right)}\right) \tag{9.2.3}$$

Employing the standard boundary conditions allows the space to be compactified as before $\phi : \mathbb{H}^2 \cup \{\infty\} \equiv S^2 \to S^2$. Which is classified using the 2nd homotopy group $\pi_2\left(S^2\right) = \mathbb{Z}$ giving the same degree for the map,

$$B = -\frac{1}{4\pi}\int \boldsymbol{\phi} \cdot \left(\partial_1 \boldsymbol{\phi} \times \partial_2 \boldsymbol{\phi}\right) \mathrm{d}^2\mathbf{x}. \tag{9.2.4}$$

9.3 Static Solutions

The equations that follow from the variation of (9.2.1) were solved using a 4th-order time dependant Runga-Kutta method, setting the time derivative to zero should the potential energy increase. The simulations were performed on a square grid of 501x501 points in the Poincare disc model of hyperbolic space (excluding any exterior points). We fix the boundary value of the field to be the vacuum to ensure finite energy $\lim_{r\to 1} \boldsymbol{\phi} = (0, 0, 1)$. For all the simulations in this section, the topological charge when calculated numerically was correct to 5 significant figures, indicating the accuracy of the results.

The standard radial ansatz can be applied, along with the product ansatz, to produce the initial conditions that were then reduced to the correct minimal energy

B	G	E	$E/(4\pi B)$	figure	B	G	E	$E/(4\pi B)$	figure
1	$O(2)$	15.4242	1.2282	9.1(a)	5	$O(2)$	74.0266	1.1782	9.1(j)
2	$O(2)$	29.1661	1.1605	9.1(b)	5	D_2	72.4888	1.1537	9.1(k)
3	$O(2)$	43.7579	1.1607	9.1(c)	5	D_5	74.3211	1.1829	9.1(l)
3	D_2	43.7086	1.1594	9.1(d)	5	D_4	74.0118	1.1779	9.1(m)
3	D_3	45.3664	1.2034	9.1(e)	6	D_2	86.8854	1.1524	9.1(n)
4	$O(2)$	58.7614	1.1690	9.1(f)	6	D_3	87.0277	1.1542	9.1(o)
4	D_2	58.0680	1.1552	9.1(g)	6	D_6	87.7212	1.1634	9.1(p)
4	D_4	58.9719	1.1732	9.1(h)	12	D_2	173.436	1.1501	9.3(a)
4	D_3	58.7157	1.1681	9.1(i)	12	D_{12}	174.865	1.1596	9.3(b)

Table 9.1: The energy for both minimal and local energy minima soliton solutions with their respective symmetry groups G, for parameters $k = 0.1, m = 1$. The solutions can be seen in figure 9.1.

configurations. A selection of the solutions are shown in figure 9.1, for parameters $k = 0.1$ and $m = 1$, which were selected for ease of plotting. Here we see that the solutions follow the form of those in flat space, with the radial form giving the minimal energy for both $B = 1$ and $B = 2$ and then for higher charges the form becomes that of chains alternating their phases by π. One caveat to this is that the chains follow geodesics of the space, namely the arcs of circles that meet the boundary at an angle of $\pi/2$.

9.4 Hyperbolic Tesselations

To study planar Skyrmion crystals we need to produce periodic boundary conditions on a unit cell, that is then used to cover the space as a tessellation. In Euclidean space this is somewhat trivial as shown in part 2 as we can use a rectangular unit cell and vary the length to find the optimal unit cell. This is due to the relatively few uniform polygons that can tessellate the space, as well as the the isometry of the space under a rescaling of the fundamental cell. In hyperbolic space, tessellations are somewhat more complex, due to the infinite number of possible tilings.

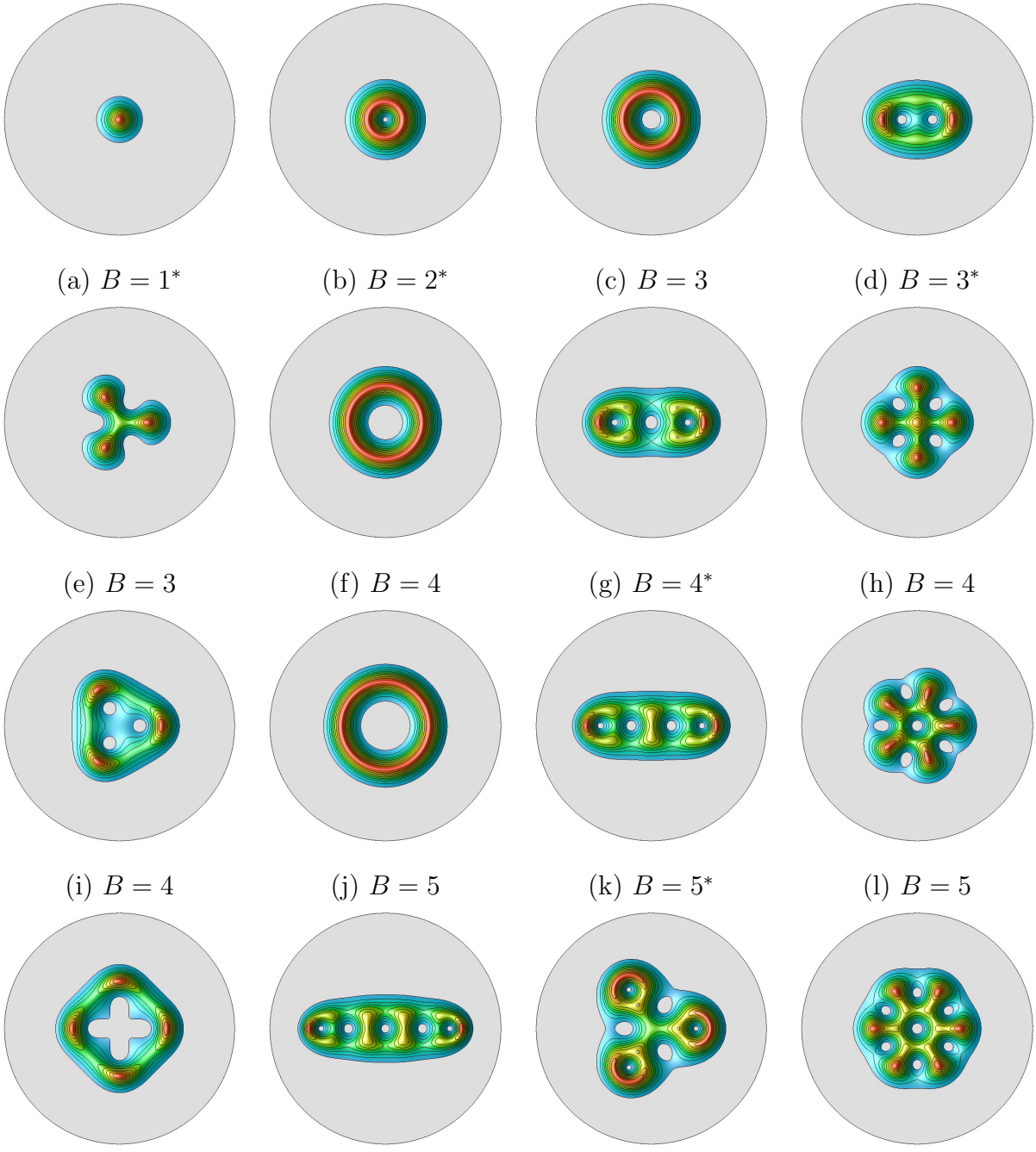

(a) $B = 1^*$ (b) $B = 2^*$ (c) $B = 3$ (d) $B = 3^*$

(e) $B = 3$ (f) $B = 4$ (g) $B = 4^*$ (h) $B = 4$

(i) $B = 4$ (j) $B = 5$ (k) $B = 5^*$ (l) $B = 5$

(m) $B = 5$ (n) $B = 6^*$ (o) $B = 6$ (p) $B = 6$

Figure 9.1: Energy density contour plots for charges $B \leq 6$ with parameters $k = 0.1$ $m = 1$. Minimal energy solutions are indicated using a * while all the energies values are given in table 9.1.

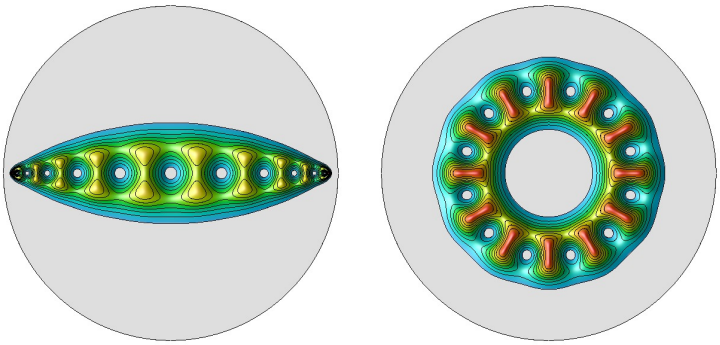

(a) $B = 12$ (b) $B = 12$

Figure 9.2: Energy density contour plots for charge $B = 12$ with parameters $k = 0.1$ $m = 1$. The left image is a plot of the chain solution and the right plot shows the ring solution with the phase of solitons alternating by π for both. The energies are given in table 9.1.

The curvature of hyperbolic space leads to the angles of polygons within the space being deformed compared to their Euclidean counterparts. A variable number of polygons can meet at a single vertex (without overlapping) dependant on the size of the polygon. This is described using the Gauss-Bonnet theorem for a hyperbolic polygon P,

$$Area(P) = (n-2)\,\pi - n\alpha, \tag{9.4.1}$$

where α is the internal angle and n the number of vertices.

Regular hyperbolic tessellations are defined using their Schlafli symbol $\{p, q\}$, where p is the number of sides of the fundamental polygon and q the number of polygons that meet at any vertex. The requirement for these polygons to then tessellate the space is for the angles at each vertex to sum to 2π, which corresponds to,

$$q\,(p-2) > 2p \tag{9.4.2}$$

with the unique area of the fundamental polygon being given as,

$$A_{\{p,q\}} = \pi\left(p - 2 - \frac{2p}{q}\right). \tag{9.4.3}$$

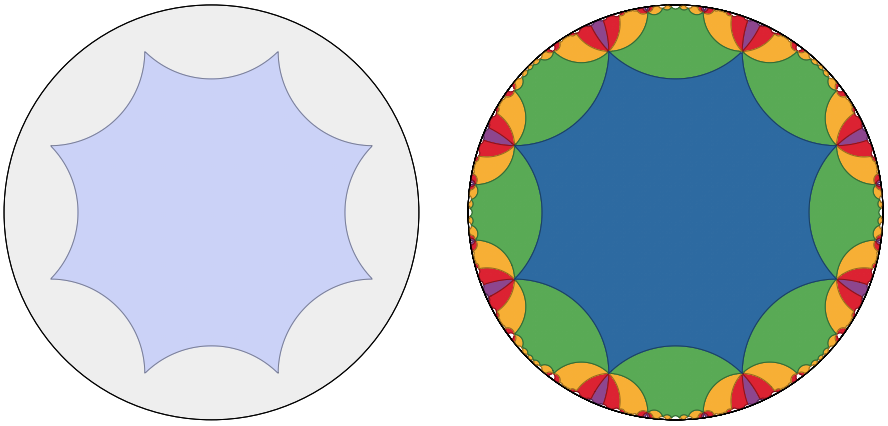

(a) $\{8,8\}$ (b) $\{8,8\}$

Figure 9.3: Plots of the Bolza surface or Schlaffi symbol $\{8,8\}$, the left plot shows the fundamental cell and the right the tessellation of the Poincare disk with the cell. For the tessellation, different colours were used for the minimal number of transformations M_k on the fundamental cell required to form that cell (only 4 transformations have been applied).

Tessellations are defined by the quotient of the Poincare disk by the Fuchsian group that corresponds to a particular Schlafi symbol. We will first discuss one of the most symmetric cases, the Bolza surface $\{8,8\}$, which is generated by 8 Mobius transformations M_k defined as,

$$M_k(z) = \frac{z + Le^{\frac{k\pi}{4}i}}{Le^{-\frac{k\pi}{4}i}z + 1} \tag{9.4.4}$$

where we have assumed our fundamental cell has its centre at the origin and L is the Euclidean distance to the centres of the neighbouring polygons. The value k is periodic, with the inverse of each element given by $M_{k+4} = M_k^{-1}$.

We now define our fundamental cell P by a Voronoi partitioning of the space,

$$P = \left\{ \boldsymbol{x} \in \mathbb{H}^2 \,|\, d(\boldsymbol{x}, \mathbf{0}) \leq d\left(\boldsymbol{x}, M_k\left(\mathbf{0}\right)\right), k = 0, ..., 7 \right\}. \tag{9.4.5}$$

9.4.1 Numerical Results

The numerical results for the fundamental cell haven't been found yet. This is due to a number of complications in considering this model, most of which stem from

the complex boundary conditions that must be imposed.

It is fairly clear that the simulations should be run using the coordinates (ρ, θ) where $\rho = \tanh^{-1}(r)$ is the hyperbolic radius. This gives a sphere of infinite radius (however this isn't an issue as we are considering finite sized unit cells only). This keeps distances from blowing up when attempting to simulate the boundary conditions.

It is unclear what one should expect from the hyperbolic tiling. There are two key issues:

- Symmetry - Unlike in flat space there is an infinite number of polygons that can tessellate hyperbolic space. In contrast the hexagonal symmetry that arises in flat space, is one of only a handful of regular tessellating polygons.

- Non-continuous fundamental cell - In flat space we can change the fundamental cells length continuously, however the area of our cell has distinct finite values it can take in hyperbolic space, as a consequence of the Gauss-Bonnet theorem. This might suggest that as the scale of the theory is altered that the form of both the fundamental cell and tesselation may undergo discrete phase transitions.

9.5 Conclusion

We have found some solutions for charges $B = 1 - 6$ of the hyperbolic baby Skyrme model. This suggests the low charge results follow the same pattern as presented for the baby Skyrme model in part 2. Additionally the chain solutions no longer follow straight lines, but the geodesics of the space. It would be interesting to consider the higher charge solutions for this space, as well as the affect curvature has.

The main reason we wanted to investigate planar Skyrmions in hyperbolic space, was to study the crystal lattice for infinite charge solutions. While the results are not completed, some interesting questions were raised. Namely the from of the tessellation of the space (and hence Schlafi symbol) could undergo discrete phase transitions with the scale of the theory.

Naturally the aim is to complete the study of the full numerical solutions for the tessellations of the space for various scales. Additionally considering the effect of extending the ideas presented to the full $SU(2)$ Skyrme model would be interesting.

Chapter 10

Baby Skyrmions in AdS_3

10.1 Introduction

This chapter is based on a paper written with Matthew Elliott-Ripley [3]. The Skyrme model has been derived from Quantum Chromodynamics (QCD) [35, 37], and then more recently from holographic QCD, as a low-energy effective theory in the large colour limit [38, 55]. In the Sakai-Sugimoto model, Yang-Mills Chern-Simons instantons in a $(4+1)$-dimensional bulk space-time, are demonstrated to be dual to Skyrmions on the boundary. The space-time behaviour of the system in the bulk is AdS like, with a conformal boundary and negative curvature.

In this section we consider baby Skyrmions in AdS_3, which is similar in structure to that of Hyperbolic space, namely constant time slices of AdS_3 give hyperbolic space $\mathbb{H}^2$. We considered Skyrmions in hyperbolic space in chapter 8, where we discussed how Skyrmions with massless pions in hyperbolic space are related to Skyrmions with massive pions in Euclidean space. Additionally, monopoles and monopole walls have been studied in AdS_4 [56,57], in an attempt to introduce static forces between the solitons and produce similar results to the Skyrme model. They were also proposed as holographic models for magnetic superconductors.

Finally Baby Skyrmions have also been considered in low-dimensional models of the Sakai-Sugimoto model in the context of dense QCD [58,59]. These simplified toy models demonstrate phase-transitions, where chains of solitons split into multiple layers as the density is increased. These have been named popcorn transitions, with

the extra layers being found to split into the holographic direction.

In this chapter we are interested in considering a pure AdS_3 background and the resulting baby Skyrmion soliton and multi-soliton solutions. One interesting feature that differentiates this background with the results in flat space, is the curvature of the spacetime. This negative curvature should allow soliton solutions to be stable, even without a pion mass term. Multi-solitons are found to take the form of ring-like structures, with phase transitions that mimick in nature those of the popcorn transitions, but with the splitting occurring in the radial direction. We also consider a point particle approximation and modify it to predict the form of solutions, based upon the method in [60]. This method turns out to be surprisingly good at predicting the popcorn-like phase transitions.

10.2 The Model

The energy of the baby Skyrme model on a general Lorentzian manifold M with metric $ds^2 = g_{\mu\nu}dx^\mu dx^\nu$ is given by

$$E = \int \left(\frac{1}{2}\dot{\boldsymbol{\phi}} \cdot \dot{\boldsymbol{\phi}} + \frac{\kappa^2}{2}(\dot{\boldsymbol{\phi}} \times \partial_i \boldsymbol{\phi}) \cdot (\dot{\boldsymbol{\phi}} \times \partial^i \boldsymbol{\phi}) \right) \sqrt{-g}\, \mathrm{d}^2\mathbf{x} + \int \left(\frac{1}{2}\partial_i \boldsymbol{\phi} \cdot \partial^i \boldsymbol{\phi} + \frac{\kappa^2}{4} (\partial_i \boldsymbol{\phi} \times \partial_j \boldsymbol{\phi}) \cdot \left(\partial^i \boldsymbol{\phi} \times \partial^j \boldsymbol{\phi}\right) + m^2 (1 - \phi_3) \right) \sqrt{-g}\, \mathrm{d}^2\mathbf{x}, \tag{10.2.1}$$

where latin indices run over spatial dimensions ($i = 1, 2$). The field equations that result from varying (10.2.1) are highly non-linear, requiring extensive numerical techniques to solve. We presented plenty of work on the solutions to the field equations that correspond to this Lagrangian for Minkowski space-time $M = \mathbb{R}^{1,2}$ in part 2. However in this chapter we are interested in solving the field equations for $M = AdS_3$. The metric is given by,

$$ds^2 = -\left(\frac{1 + r^2}{1 - r^2}\right)^2 dt^2 + \frac{4L^2}{(1 - r^2)^2} \left(dr^2 + r^2 d\theta^2\right). \tag{10.2.2}$$

L is the AdS radius and is related to the cosmological constant of the model $\Lambda = -1/L^2$ and r is the radial coordinate $r = \sqrt{x^2 + y^2} \in [0, 1)$. It is clear that the

value $r = 1$ corresponds to the boundary of the space, where all points have infinite distance to all others. The Ricci scalar curvature can be calculated as $R = -6/L^2$. In the limit $L \to \infty$ this curvature vanishes and we recover flat space. The space is maximally symmetric and thus shouldn't affect the symmetry of the solutions, due to symmetric criticality.

We find the geodesic distance between two arbitrary points in the space $\boldsymbol{x}$ and $\boldsymbol{y}$ to be,

$$d(\boldsymbol{x}, \boldsymbol{y}) = L \cosh^{-1}\left(1 + \frac{2\left|\boldsymbol{x} - \boldsymbol{y}\right|^2}{\left(1 - \left|\boldsymbol{x}\right|^2\right)\left(1 - \left|\boldsymbol{y}\right|^2\right)}\right) \tag{10.2.3}$$

It is also useful to consider our equations by replacing the radial coordinate in (10.2.2) with the hyperbolic radius $\rho = 2L \tanh^{-1} r$, to give the metric as,

$$ds^2 = -\cosh^2\frac{\rho}{L}dt^2 + d\rho^2 + L^2 \sinh^2\frac{\rho}{L}d\theta^2 \tag{10.2.4}$$

where our radial coordinate now has the range $\rho \in [0, \infty)$ and coincides with the geodesic distance from the origin of the model.

Due to the nature of the AdS space-time, it is not clear how to define a translation as a symmetry of the space. This leads us to rely on the translation derived from the constant time slices of AdS, namely hyperbolic 2-space. A translation that sends the origin to a given point $\boldsymbol{a}$ is given by,

$$\boldsymbol{x} \mapsto \frac{(1 - |\boldsymbol{a}|^2)\boldsymbol{x} + (1 + 2\boldsymbol{x}\cdot\boldsymbol{a} + |\boldsymbol{x}|^2)\boldsymbol{a}}{1 + 2\boldsymbol{x}\cdot\boldsymbol{a} + |\boldsymbol{a}|^2|\boldsymbol{x}|^2}\,. \tag{10.2.5}$$

One may think that due to constant time slices of our metric (10.2.2) giving hyperbolic space, that the solutions to the static energy would match those in hyperbolic space. However this is not the case, due to the warp factor of the metric including an additional term $\sqrt{-g_{tt}} = \frac{(1+r^2)}{(1-r^2)}$. This additional term should lead to energies being lower at the centre of the space allowing us to evade Derrick's theorem [6], which in flat space leads to the requirement of a mass term for the pions in the theory.

For finite energy we require $\boldsymbol{\phi}$ to be a vacuum at spatial infinity, hence it can be viewed as a map from the compactified physical space, $\mathbb{H}^2 \cup \{\infty\} = S^2$, to the

target space S^2. This is equivalent to the flat space model considered in part 2 and hence gives the same integral form for the degree of the map,

$$B = -\frac{1}{4\pi}\int \boldsymbol{\phi}\cdot(\partial_1\boldsymbol{\phi}\times\partial_2\boldsymbol{\phi})\,\mathrm{d}^2\mathbf{x}. \tag{10.2.6}$$

While we have no mass term to pick out the favoured vacuum value on the boundary of the space, we will retain the standard choice of $\boldsymbol{\phi}_\infty = (0,0,1)$, as this will allow easy comparison of results, as well as allowing the mass term to be switched on and off without issue. This leads to the centres of single solitons being interpreted as the antipodal point on the target space $\phi_3 = -1$.

Finally the bogomolny bound doesn't change due to our change of background. This can be seen easily by considering the two inequalities,

$$|\partial_x\boldsymbol{\phi} \pm \boldsymbol{\phi}\times\partial_y\boldsymbol{\phi}|^2 \geq 0\,, \quad \frac{1+r^2}{1-r^2} \geq 1\,, \tag{10.2.7}$$

which give the bound for the energy to be $E \geq 4\pi\,|B|$.

10.3 Radial Solutions

The first solutions we consider are reductions in dimension of the energy to a radial equation. The space, as well as the energy, have $O(2)$ symmetry, due to symmetric criticality this leads us to conclude that the single soliton also retains this symmetry. We also expect the radial solutions to be centred at the origin of the space, due to the warp factor. We write the fields in terms of the standard radial hedgehog ansatz,

$$\boldsymbol{\phi} = (\sin(f(\rho))\cos(B\theta-\chi), \sin(f(\rho))\sin(B\theta-\chi), \cos(f(\rho))), \tag{10.3.1}$$

for polar coordinates ρ and θ, where $f(\rho)$ is a positive monotonically decreasing function. The boundary conditions on $f(\rho)$ are $f(0) = \pi$ and $f(\infty) = 0$. χ gives the isorotation of the soliton, although the energy of a single soliton is invariant to this rotation, the individual fields are not. χ will play an important role in the interaction of solitons with each other, but is ignored at this stage. If we substitute this into the static energy given in (10.2.1), we get the following radial energy,

$$E = \frac{L\pi}{2}\int_0^\infty \sinh\frac{2\rho}{L}\left(f'^2 + \frac{B^2\sin^2 f}{L^2\sinh^2\frac{\rho}{L}}(1+\kappa^2 f'^2) + 2m^2(1-\cos f)\right)d\rho\,. \quad (10.3.2)$$

The profile function $f(\rho)$ can easily be found numerically using a simple gradient flow method, for various values of parameters and charge B. We can numerically investigate the behaviour of the solutions, using the standard definition of the size of a soliton,

$$\mu : f(\mu) = \pi/2. \quad (10.3.3)$$

We simulate the change in size by altering the parameters κ and L for various values of charge B. Working in the massless limit we find that the leading order dependence is $\mu \sim \sqrt{\kappa L}$ for small values of κ/L, however the non-linear effects dominate for large κ/L. On comparing this to the results for flat space in part 2 ($\lim_{L\to\infty}\mu \sim \sqrt{\kappa/m}$), we can interpret this result as the curvature of the AdS_3 space introducing an effective pion mass to the model.

Finally we can consider the asymptotic behaviour of the radial solution decay. Linearising the equations of motion that result from varying the radial energy (10.3.2) gives,

$$L^2\sinh\frac{2\rho}{L}f'' + 2L\cosh\frac{2\rho}{L}f' - \sinh\frac{2\rho}{L}\left(\frac{B^2}{\sinh^2\frac{\rho}{L}} + m^2L^2\right)f = 0\,. \quad (10.3.4)$$

Substituting in the standard values for κ and B and taking the limit $\rho\to\infty$, we can find the asymptotic tail decay to be,

$$f(\rho) \sim e^{-\left(1+\sqrt{1+m^2L^2}\right)\rho/L}\,. \quad (10.3.5)$$

It is particularly interesting to note that the exponential decay of the tail remains for the massless pion limit, unlike the flat space model shown in (2.3.11), which becomes algebraic,

$$\lim_{L\to\infty} f(\rho) \sim \begin{cases} \rho^{-B}, & \text{if } m = 0 \\ \frac{1}{\sqrt{\rho}}e^{-m\rho}, & \text{if } m \neq 0\,. \end{cases} \quad (10.3.6)$$

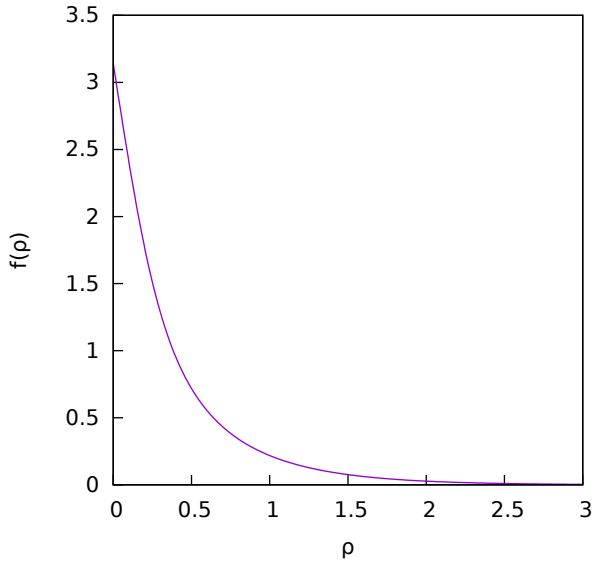

Figure 10.1: Radial profile function $f(\rho)$ centred at the origin for $B = 1$, with $\kappa = 0.1$ and $m = 0$. Found using a gradient flow method.

Note that the limit $L \to \infty$ has to be taken carefully for the radial equations of motion (10.3.4). The similarity between tail decays again suggests a relation between curvature in AdS_3 and the flat space model with massive pions.

We can now minimise (10.3.2) to find the profile function $f(\rho)$. This was performed using a simple gradient flow algorithm, with the result displayed in figure 10.1 for $\kappa = 0.1$ and $m = 0$. Note that the single soliton solution was also modelled using a Runga-Kutta method presented later, shown in figure 10.2. This agreed with the profile function but also allowed us to test moving the ansatz about the space. This resulted in the solution moving back to the centre of the grid to minimise its energy, confirming the suspicion that solutions want to form at the origin. Also note that the solution is indeed stable for massless pions $m = 0$ and Derrick's theorem has been evaded. From these two aspects of our results, it is clear that the space is providing the expected centralizing effect on the solutions.

We find that the radial solutions presented here are the minimal energy solutions for $B = 1 - 3$. This covers a larger range than the flat space model and is likely due to the centralising force of the AdS_3 metric.

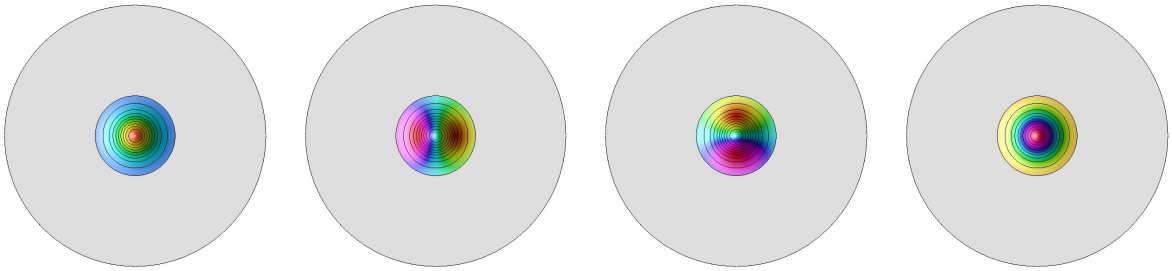

(a) (b) (c) (d)

Figure 10.2: Energy density contour plots for charge $B = 1$ (single soliton solution) for $\kappa = 0.1$ and $m = 0$. The colour scheme is based on the value of a) energy density b) ϕ_1 field c) ϕ_2 field d) ϕ_3 field. Note, a contour plot using charge density produces a similar result.

10.4 Multi-solitons

To find the minimal energy solutions for $B > 3$ we must consider alternate methods. We used an RK4 method to minimise the energy (10.2.1), cutting the kinetic energy if the potential increases. We chose to set $\kappa = 0.1$ and $m = 0$. The solutions are modelled on a square grid with $(501)^2$ grid points and AdS length $L = 1$. The lattice spacing is then given to be $\Delta x = 0.002$ and spatial derivatives are approximated using fourth-order finite difference methods. We have also fixed the boundary of our grid to be the vacuum at spatial infinity $\boldsymbol{\phi}_\infty = (0, 0, 1)$. For all our simulations the topological charge, when computed numerically, gives an integer value to at least five significant figures, indicating the accuracy of the results.

We require an initial approximation for our numerical system from which the system can be relaxed. Consider the field configuration

$$\boldsymbol{\phi} = (\sin(f)\cos(B\theta), \sin(f)\sin(B\theta), \cos(f)), \tag{10.4.1}$$

for polar coordinates r and θ, and where $f(r)$ is a monotonically decreasing function of r. This is equivalent to the radial ansatz with a coordinate change.

To find solutions with lower symmetry, we also considered similar initial conditions but with a symmetry breaking perturbation. Once a pattern was discernible for these lower symmetry forms, we also used a product ansatz for our initial conditions. In other words we placed single solitons about our grid using hyperbolic

translations and then performed our energy minimisation procedure. The minimal energy solutions found for charges $B = 1 - 20$ can be seen in figure 10.4, while the many local minima solutions for charges $B = 1 - 10$ can be found in figures 10.12-10.14 in appendix A, at the end of this chapter. The local minima in appendix A also show the field configurations to give an idea of the relative rotation of well separated solitons. The minimal energies for the charges $B = 1 - 20$ can be found in table 10.1.

For $B = 2$ we observe the lower energy being the radial solution, as with the flat space system. For $B = 3$ however, we find that the radial solution retains the minimal energy, unlike the flat space system. A local energy solution however does exist (fig 10.12 (d)), though it has a significantly higher energy of $E/(4\pi B) = 1.3358$.

The results start to take a more discernible pattern for $B \geq 4$. For $B = 4$ the solution appears to take the form of four single solitons close to each other in a square centred at the origin (fig 10.4 (d)). This pattern continues for charges $B = 5 - 7$, with the solitons positioned in an equally spaced ring forming a regular B-gon, centred at the origin. The relative phase difference (which can be seen in the appendix) between neighbouring solitons is π for even B and $\pi \pm \pi/B$ for odd B.

The $B = 8$ solution has a slight deviation from the standard octagon, as the minimal energy solution has the points on a squashed octagon. A regular octagon solution was found (fig 10.13 (h)), however it has an energy of 1.4543 as opposed to the squashed octagon with the slightly lower energy 1.4541. While this energy difference is very small, a perturbation of the regular octagon will lead to the squashed shape, with most initial conditions leading also to the squashed octagon solution. This leads us to conclude that the regular octagon is a saddle point solution, constrained by symmetric initial conditions. This deformed octagon shape is likely due to the size of the ring causing the solution to be far less stable and indeed we find that $B = 8$ is the final single ring solution for increasing charge.

For charge $B \geq 9$ we observe a transition to multi-layered concentric rings. We denote these multi-layered ring solutions as $\{n_1, n_2, n_3, \ldots\}$, where n_i gives the charge of the i^{th} ring from the origin out. For $9 \leq B \leq 16$ the central layer takes

Table 10.1: The minimal energies for soliton solutions with topological charge $1 \leq B \leq 20$ and parameters $\kappa = 0.1$, $m = 0$.

B	form	E/B	figure	B	form	E/B	figure
1	$\{1\}$	1.2548	10.4(a)	11	$\{2,9\}$	1.5368	10.4(k)
2	$\{2\}$	1.2312	10.4(b)	12	$\{2,10\}$	1.5554	10.4(l)
3	$\{3\}$	1.2878	10.4(c)	13	$\{2,11\}$	1.5788	10.4(m)
4	$\{4\}$	1.3384	10.4(d)	14	$\{2,12\}$	1.6017	10.4(n)
5	$\{5\}$	1.3725	10.4(e)	15	$\{3,12\}$	1.6250	10.4(o)
6	$\{6\}$	1.3886	10.4(f)	16	$\{3,13\}$	1.6481	10.4(p)
7	$\{7\}$	1.4263	10.4(g)	17	$\{4,13\}$	1.6714	10.4(q)
8	$\{8\}$	1.4541	10.4(h)	18	$\{4,14\}$	1.6914	10.4(r)
9	$\{1,8\}$	1.4888	10.4(i)	19	$\{5,14\}$	1.7107	10.4(s)
10	$\{1,9\}$	1.5157	10.4(j)	20	$\{6,14\}$	1.7276	10.4(t)

the form of a slightly deformed radial solution. The symmetry of the deformation matches the symmetry of the outer ring. For $17 \leq B \leq 20$ the inner ring takes a multi-soliton form, whose symmetry is again determined by the outer ring.

If we consider each minimal energy solution as a perturbation on the previous one, we have a choice of rings to which the additional charge can be added. Due to the warp factor, this charge is added to the inner most ring that has the space to expand. This continues until the inner-ring has 8 single solitons at which time there is then enough room to place a single soliton in the centre of the grid, beginning a new ring. It seems natural to assume that this nature would then continue for higher charges.

The transitions from the single ring solution to multi-ring solutions are similar to the popcorn transitions observed in toy models of the Sakai-Sugimoto model [59]. We would expect further transitions to occur for higher charges, but it is numerically challenging to achieve this due to the number of local minima that occur. Due to this it would be useful to have some way of predicting the form of solutions, which is discussed in the following section.

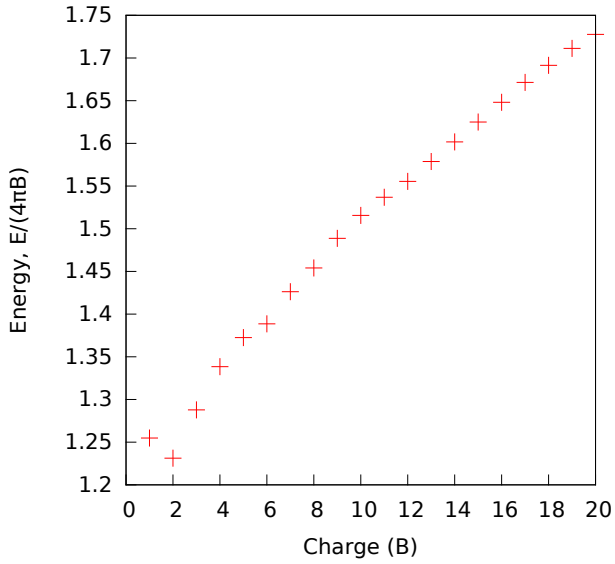

Figure 10.3: Plot of energies for soliton solutions with topological charge $1 \leq B \leq 20$ and parameters $\kappa = 0.1$, $m = 0$.

The energies of the various charge solutions can be seen in table 10.1 and are plotted in figure 10.3. Note that they generally increase with charge. This is not a surprise as the gravitational effect of the AdS metric makes it favourable to be near the centre of the space. As the amount of charge is increased the solitons are forced further from the centre and contribute more energy than a single soliton placed at the centre of the space. The surprising factor of the energy is the fairly smooth form is takes despite the discrete nature of the solutions. This suggests that the gravitational aspect of the metric toward the origin is the dominant effect.

10.5 Point Particle Approximation

The results presented in figure 10.4 are somewhat reminiscent of the ancient maths problem of circle packings within a circle [61]. This fun problem poses the question, what is the minimal radius circle within which I can fit n congruent circles. The optimal configurations tend to present in the form of multi-layered rings. There is a key issue in using this as an approximation for baby Skyrmions in AdS_3, in that the transitions occur far too early, at $n = 7$ and 19 for the first two respectively.

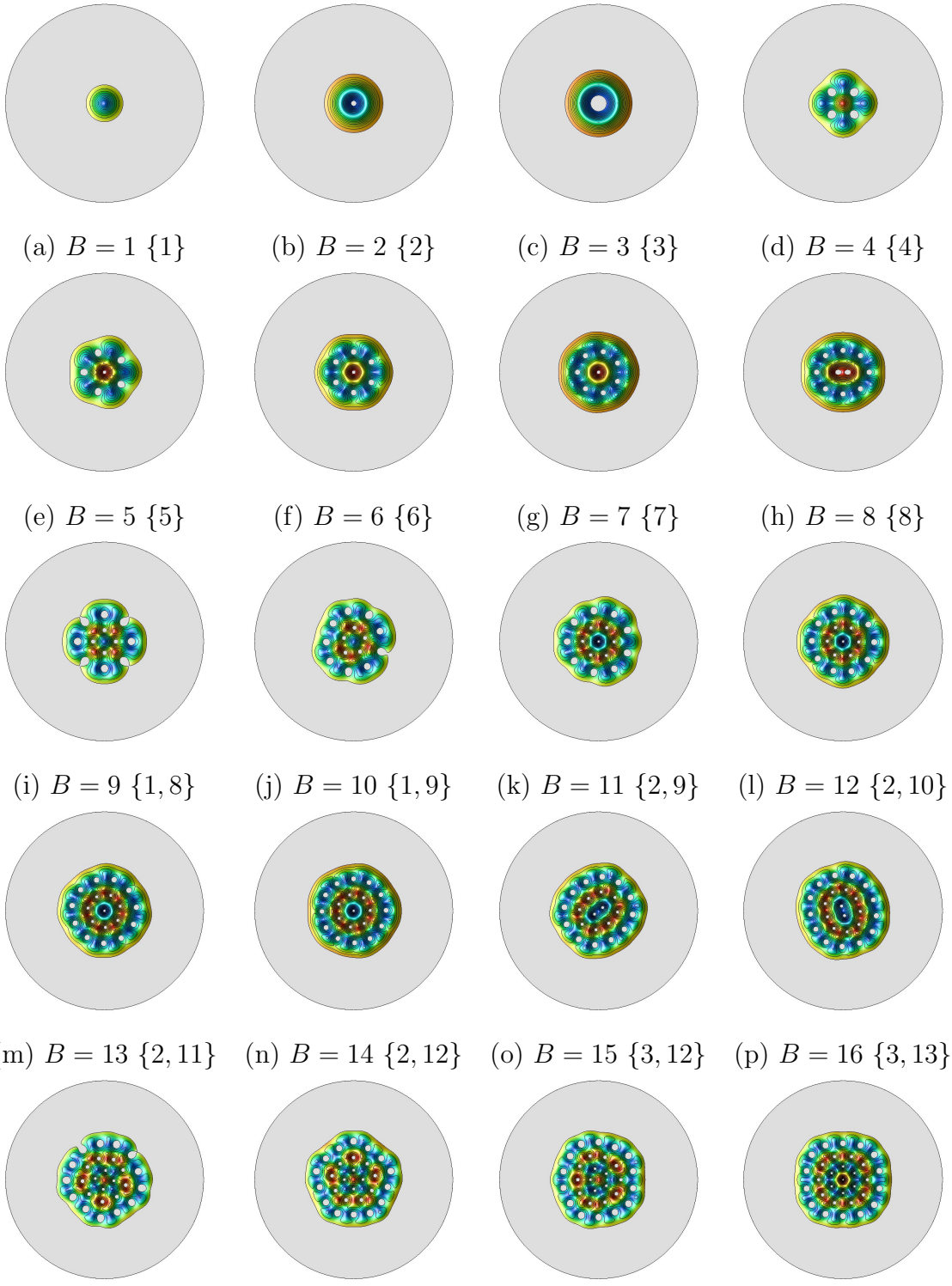

(a) $B = 1$ $\{1\}$ (b) $B = 2$ $\{2\}$ (c) $B = 3$ $\{3\}$ (d) $B = 4$ $\{4\}$

(e) $B = 5$ $\{5\}$ (f) $B = 6$ $\{6\}$ (g) $B = 7$ $\{7\}$ (h) $B = 8$ $\{8\}$

(i) $B = 9$ $\{1, 8\}$ (j) $B = 10$ $\{1, 9\}$ (k) $B = 11$ $\{2, 9\}$ (l) $B = 12$ $\{2, 10\}$

(m) $B = 13$ $\{2, 11\}$ (n) $B = 14$ $\{2, 12\}$ (o) $B = 15$ $\{3, 12\}$ (p) $B = 16$ $\{3, 13\}$

(q) $B = 17$ $\{4, 13\}$ (r) $B = 18$ $\{4, 14\}$ (s) $B = 19$ $\{5, 14\}$ (t) $B = 20$ $\{6, 14\}$

Figure 10.4: Energy density contour plots of the soliton solutions for $B = 1 - 20$, with $\kappa = 0.1$ and $m = 0$. They are coloured by the value of the ϕ_3 field, hence single soliton positions can be identified ($\phi_3 = -1$) as the dark blue points. The ring numbers are included in the form $\{n_1, n_2, n_3, \ldots\}$ where n_i is the number of solitons in the i^{th} ring.

This is likely due to the malleable nature of the baby Skyrmions and their ability to overlap. Simulations were run to consider the problem in the Poincare model and the problem persisted. What the model does suggest is that a point particle approximation could predict the correct qualitative form of the multi-layered ring like solutions, if the non-linear interactions of the solitons could be introduced.

In order to improve the approximation we assume we can split the energy of our solutions into two competing terms:

- Gravitational potential - models the centralising force of the AdS metric in terms of a simple potential term.
- Interaction term - models the non-linear interactions between single solitons that gives an optimal separation for soliton pairs.

If we can approximate the values of these terms for point particles, then we can quickly solve this simplified model to approximate minimal energy solutions for higher charges. In order to achieve this, we will assume that hyperbolic translations of minimal energy solutions, approximate similarly charged constituent parts of multi-soliton configurations. As discussed previously these are not solutions to the equations of motion, due to the additional term in the warp factor breaking this isometry of the space.

10.5.1 Gravitational Potential

To approximate a potential from the AdS_3 metric we can utilise the geodesic equations of motion, integrating to form a potential term. We will assume that our solutions have negligible velocity throughout. This gives the geodesic equations to be,

$$\begin{aligned} t'' &= -\frac{8}{1-r^4}(xx'+yy')t' \,, \\ x'' &= -\frac{x(1+r^2)}{L^2(1-r^2)}(t')^2 + \frac{2x}{1-r^2}(y')^2 - \frac{4x}{1-r^2}x'y' \,, \\ y'' &= -\frac{y(1+r^2)}{L^2(1-r^2)}(t')^2 + \frac{2y}{1-r^2}(x')^2 - \frac{4y}{1-r^2}x'y' \,, \end{aligned} \tag{10.5.1}$$

where primes denote differentiation w.r.t. proper time. Using the assumtion of negligible velocity x', $y' \ll t'$ we can write

$$\ddot{x} = \frac{x''}{(t')^2} - \frac{x't''}{(t')^3} \approx \frac{x''}{(t')^2} \approx -\frac{x(1+r^2)}{L^2(1-r^2)} \equiv -\frac{x}{r}\partial_r\Phi\,, \tag{10.5.2}$$

Integrating this equation gives us the desired potential,

$$\Phi(r) = \int_0^r \frac{R(1+R^2)}{L^2(1-R^2)}\,dR = \frac{A}{L^2}\left[\frac{r^2}{2} + \log\left(r^2-1\right)\right]. \tag{10.5.3}$$

where A is a constant to be numerically fit to the data.

We numerically approximate the gravitational potential by translating a single soliton from the origin radially out towards the boundary of the space, subtracting the original energy of the soliton at the origin. We can then fit our approximation for the gravitational potential (10.5.3) and find a value for the constant A using a least squares fit method to be $A = -62.8$. We choose to fit the data out to the radius $r = 0.6$, as for even large configurations they don't tend to have a radius much beyond this. Additionally the hyperbolic translation choice breaks down the closer to the boundary we get. Finally we did try fitting the data to larger radii, but the results led to incorrect values for transitions for the approximation.

The results of the numerical approximation and least squares fit are presented in figure 10.5 for parameters $\kappa = 0.1$, $L = 1$ and $m = 0$. The accuracy is good to the radius required but diverges for higher radii, this deviation is unlikely to make much difference except for extremely high values of charge.

10.5.2 Interaction Term

In $\mathbb{R}^{2,1}$, the analytic approach to predict the interaction of two solitons as point particles, is to assume only their tails interact. This allows the space to be separated into three regions, one for each soliton (where it dominates) and one for the tail interactions. This approach requires each soliton to be translated to its position and to independently be a solution to the equations of motion. In AdS_3 however this is not the case, as we have been relying on the hyperbolic translation as an approximation, but this is not an isometry of the space. Due to this, we will need to numerically approximate the non-linear interactions and fit some general interaction potential to the data.

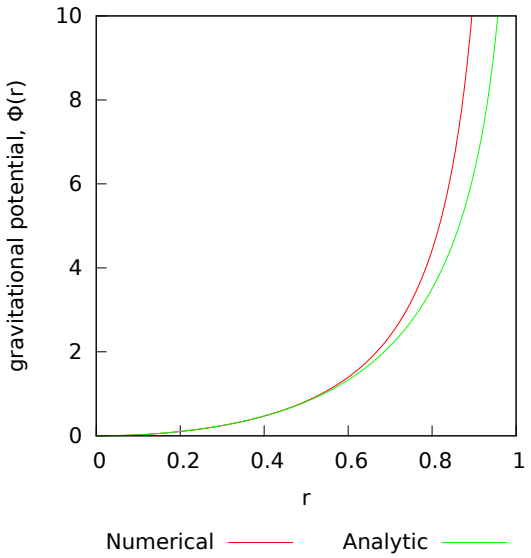

Figure 10.5: Numerical and analytical approximations for the point particle gravitational potential produced by the AdS_3 metric. The analytic approximation is $\Phi(r) = \frac{A}{L^2}\left[r^2/2 + log\left(r^2 - 1\right)\right]$ where $L = 1$, $A = -62.8$ and has been fit to the numerical data. The numerical approximation is the energy for a singe soliton translated about the grid with the minimal energy subtracted off.

We approximate the interaction energy using the product ansatz (as we have assumed the solitons are point particles). We translated the two single solitons to various separations and considered the energy difference from two single solitons, as well as their associated gravitational potentials. Note that the interaction energy will differ based on the phase difference $\chi(\psi_1, \psi_2, \boldsymbol{x}_1, \boldsymbol{x}_2)$, which is measured relative to the connecting geodesic between the two solitons. Figure 10.6 shows this in more detail. We have plotted the results for $\chi = 0$ and π in figure 10.7. The lower curve represents the 'in phase' ($\chi = \pi$) or maximally attractive channel, while the upper curve is the 'out of phase' ($\chi = 0$) or maximally repulsive channel.

We choose to fit the data to the Morse potential, which is the standard intermolecular interaction energy, of the form,

$$U_{Morse}(\rho) = D_e \left(1 - e^{-a(\rho-\rho_e)}\right)^2 \tag{10.5.4}$$

where ρ is the geodesic distance between two points, ρ_e is the position of the minimum of the potential well and hence the equilibrium distance under no other forces, D_e is the depth of the well and a determines the width of the potential.

The drawback of this method is the lack of any phase dependence, though this can be introduced by expanding the expression into two terms and assuming that the energy is its highest for $\chi = 0$ and lowest for $\chi = \pi$, thus we introduce a phase dependant coefficient to give,

$$U_\chi(\rho) = D_e \left(e^{2a(1-\rho/\rho_e)} + 2\cos\chi\, e^{a(1-\rho/\rho_e)}\right). \tag{10.5.5}$$

We can now fit the expression above to the numerical data acquired using a least squares method. We did this for $\chi = \pi$ which is the most relevant value. Note that the product ansatz is only valid for well separated solitons, hence we only fit the data for separation greater than twice the size ($\mu : f(\mu) = \frac{\pi}{2}$) of a single soliton. This is plotted for the parameters $\kappa = 0.1$, $L = 1$ and $m = 0$ in figure 10.7, where the coefficients are found to be $D_e = 0.76$, $\rho_e = 0.73$ and $a = 1.13$. The plots for both $U_0(\rho)$ and $U_\pi(\rho)$ are very close for the relevant separations.

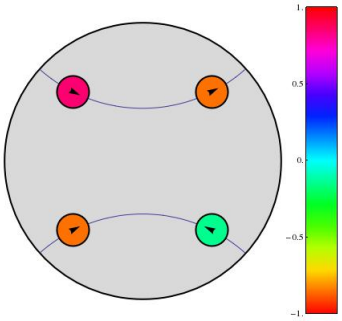

Figure 10.6: Shows two sets of solitons with their connecting geodesics. The top pair are in the maximally repulsive channel, with relative rotations of of $\chi = 0$ and the bottom pair are in the maximally attractive channel with relative rotation $\chi = \pi$. Their relative rotations in the embedded flat space are shown using both their colour and the arrow, where $\chi \in [\pi, -\pi]$.

10.5.3 Higher Charge Rings

We can now minimise our point particle approximation to predict the qualitative forms of solutions for higher charges. The energy for B single solitons is given by the formula,

$$E_B = \sum_{a=1}^{B} \left(\Phi(r_a) + \sum_{b>a} U_\chi(\psi_a, \psi_b, d(\boldsymbol{x}_a, \boldsymbol{x}_b)) \right) , \tag{10.5.6}$$

with positions $\boldsymbol{x}_a$, internal phases ψ_a and radial distance $r_a \equiv |\boldsymbol{x}_a|$.

We used a finite temperature simulated annealing method to minimise the approximation energy (10.5.6), with random initial conditions. The results for charges $B = 1 - 20$ are shown in figure 10.8. The colours of the point particles indicates their internal phases as shown in figure 10.6.

The approximation solutions clearly follow a similar pattern to those of the full field numerics, but can be produced in a fraction of the time. The approximation correctly predicts the B-gon structure for $B \leq 7$, as well as the correct internal phases, changing by π for even B and $\pi \pm \pi/B$ for odd B. For $B = 8$, the approximation picks out the maximally symmetric octagon as the solution, rather than the squashed solution seen in figure 10.4 (h). It then correctly predicts the first

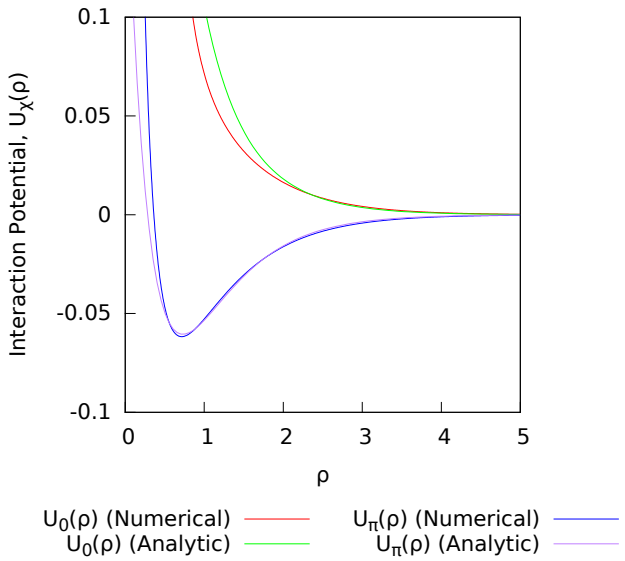

Figure 10.7: Numerical and analytical approximations for the point particle interaction potential $U_\chi(\rho)$. The analytic approximation is $U_\chi(\rho) = D\left(\exp\left(2a\left(1-\rho/\rho_e\right)\right) + 2\cos\chi\exp\left(a\left(1-\rho/\rho_e\right)\right)\right)$ where $D = 0.83$, $\rho_e = 0.7$, $a = 1.1$ and χ gives the relative phase difference. The parameters above have been fit to the numerical data for $\rho > 2\mu$, where $\mu = \rho : f(\rho) = \pi/2$. The numerical approximation was found by removing the gravitational potentials shown above and the single soliton energys and considering a static soliton pair, translated using the hyperbolic isometries.

transition to occur at $B = 9$ to $\{1, 8\}$. The multi-ring structure remains for all charges, though some of the charge values are incorrect in comparison to the full field model. This occurs at values $B = 11, 13, 15, 16, 19, 20$ and appears to occur due to the approximation not packing the lower charged rings tight enough. This is likely due to two issues, in that the approximation cannot model the more compact radial solutions for lower charges that we see in the full field solutions as well as assuming that the particles have zero size. However, while there are minor differences they are very slight and predictable in nature. This would suggest that for higher charges, the approximation should give good approximations to minimal energy solutions, or at least give an indication as to where to look for them.

If we consider higher charge solutions to the approximation we find further popcorn like transitions as predicted. The first of these occurs at $B = 27$, $\{8, 18\} \rightarrow \{1, 8, 18\}$. Using this predicted transition as a guide for initial conditions, we indeed found that the transition occurs either at $B = 27$ or $B = 28$, as shown in figure 10.9 with energies in table 10.5.3 (our numerical accuracy wasn't high enough to differentiate the two solutions for $B = 27$). The next two transitions were then found to occur at $B = 54$, $\{8, 17, 28\} \rightarrow \{1, 8, 17, 28\}$ and $B = 95$, $\{8, 17, 28, 41\} \rightarrow \{1, 8, 17, 28, 41\}$, which can be seen in figure 10.10.

Note that the approximation predicts very consistent numbers for the various number rings before a transition occurs. This indicates that the various rings expand until they saturate some standard bound and then transition to having an additional ring.

Finally we consider the infinite charge limit. One would expect some sort of Skyrmion crystal with a fixed symmetry to become apparent. We minimise the approximation for charge $B = 200$ and $B = 250$ which are shown in figure 10.11. While the ring structure is still apparent for the outer layers, the inner layers are more deformed and may indicate some emergent lattice structure for this high charge. It would be extremely interesting to study this lattice structure, though doing so in hyperbolic space may be a simpler task initially, as discussed in the previous chapter.

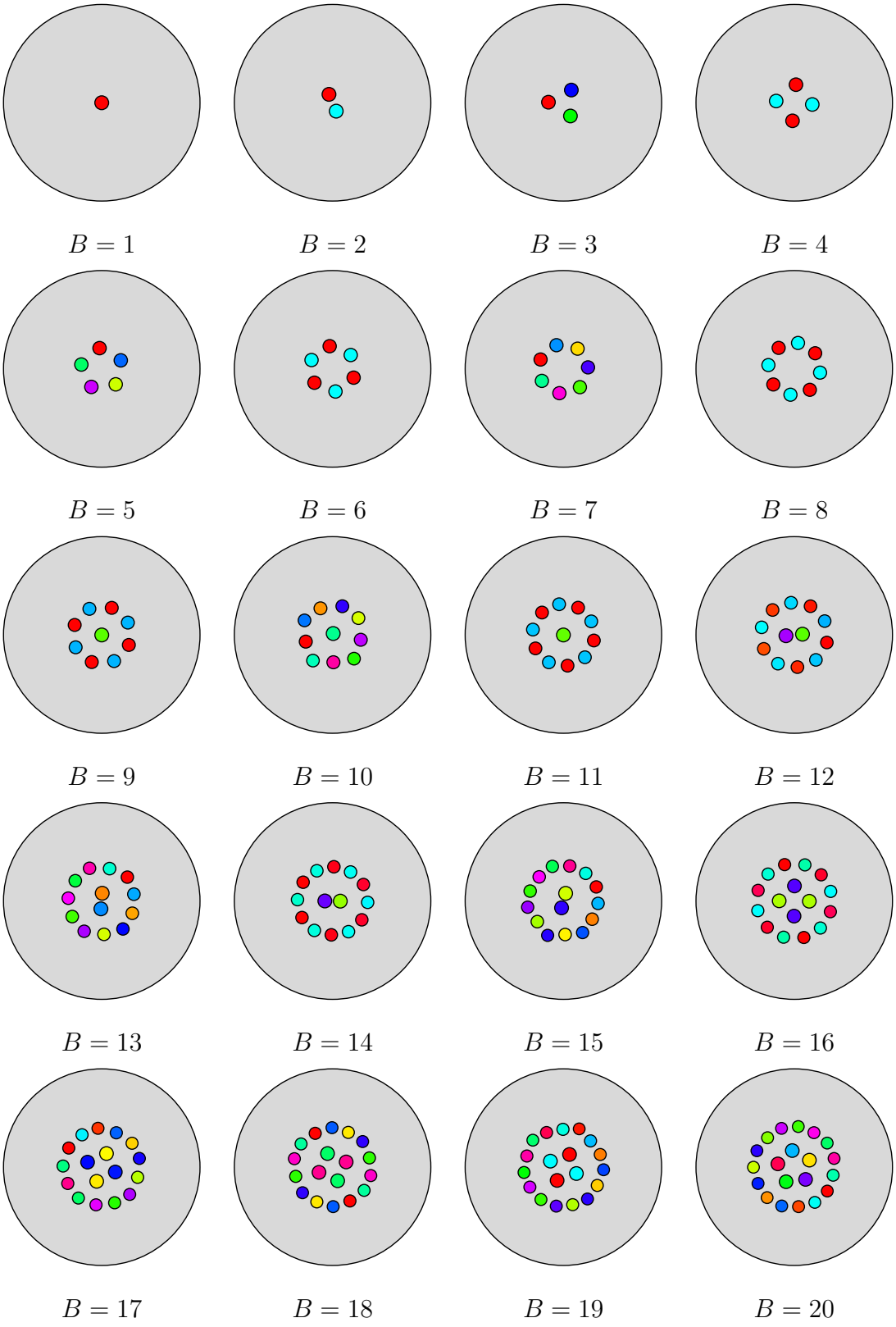

Figure 10.8: Minimal energy configurations for the point particle approximation for $B = 1 - 20$, found using a finite temperature annealing method. The parameters used in the approximation were $L = 1$, $\kappa = 0.1$ and $m = 0$. The approximations correspond to the full field solutions shown in figure 10.4.

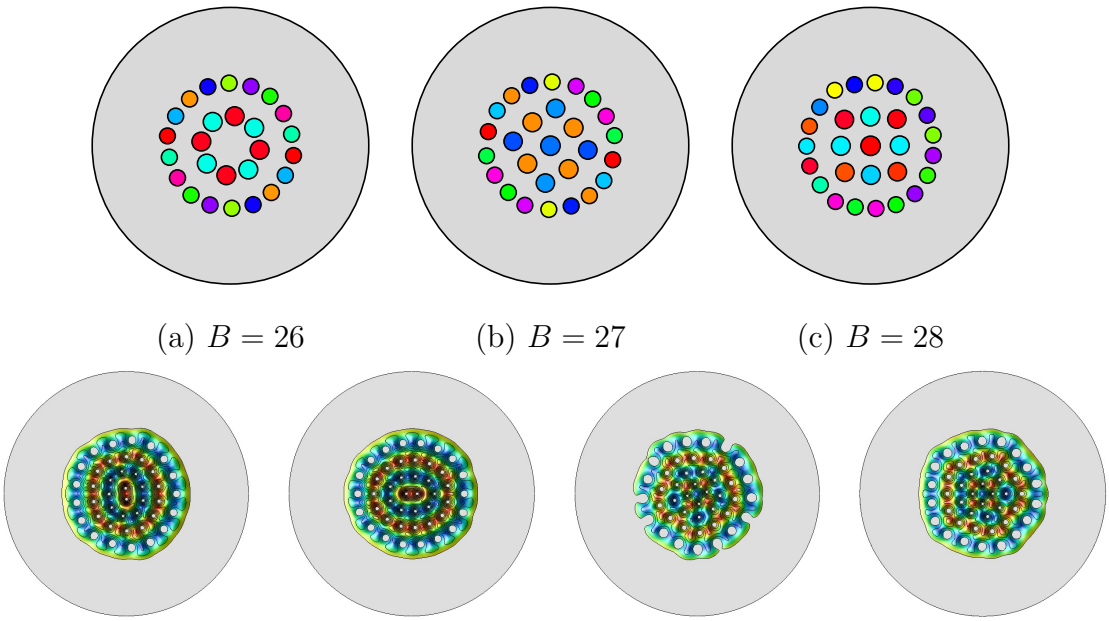

(a) $B = 26$ (b) $B = 27$ (c) $B = 28$

(d) $B = 26$ (e) $B = 27$ (f) $B = 27$ (g) $B = 28$

Figure 10.9: The top row are the approximations for the 2nd popcorn like transition while the bottom row is the corresponding minimal energy full field numerical solutions. We find two solutions for $B = 27$ with energies within numerical error, hence the transition occcurs at $B = 27$ or $B = 28$ as predicted. The energies for these plots are shown in table 10.5.3, for the parameters $\kappa = 0.1$, $m = 0$ and $L = 1$.

B	form	E/B	figure
26	$\{9, 17\}$	1.8357	10.9(d)
27	$\{9, 18\}$	1.8546	10.9(e)
27	$\{1, 9, 17\}$	1.8546	10.9(f)
28	$\{1, 9, 18\}$	1.8723	10.9(g)

Table 10.2: Minimal energies for charge $B = 26-28$, demonstrating the 2^{nd} popcorn transition. We find two solutions for $B = 27$ with energies within numerical error, hence the transition occurs at $B = 27$ or $B = 28$. The parameters used were $\kappa = 0.1$, $m = 0$ and $L = 1$.

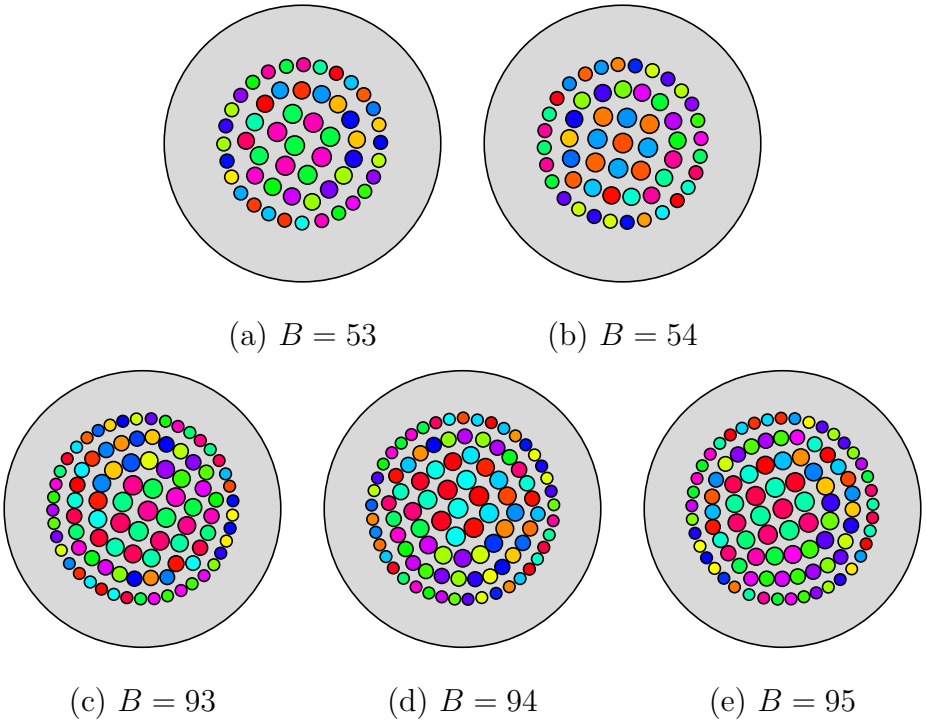

(a) $B = 53$ (b) $B = 54$

(c) $B = 93$ (d) $B = 94$ (e) $B = 95$

Figure 10.10: Point particle approximation solutions for the 3^{rd} and 4^{th} popcorn like transitions for parameters $\kappa = 0.1$, $m = 0$ and $L = 1$.

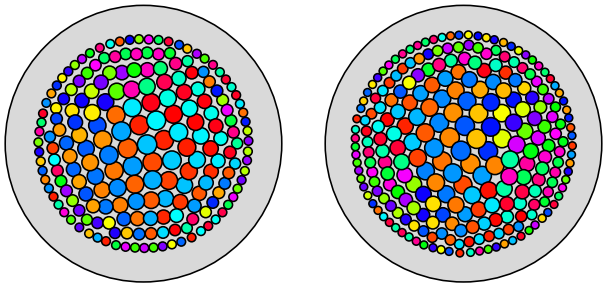

(a) $B = 200$ (b) $B = 250$

Figure 10.11: Point particle approximation for charges $B = 200$ and $B = 250$, for parameters $\kappa = 0.1$, $m = 0$ and $L = 1$. While the exterior particles still have a ring structure, the inner particles are being forced into a lattice structure.

10.6 Conclusions

In this chapter we have studied the various static solutions to the baby Skyrme model embedded in $(2+1)$-dimensional Anti de-Sitter space. We have shown that the solutions do not require a mass term to have stable solutions, as the curvature of the metric acts by introducing an effective mass to the model. We demonstrated that the multi-soliton solutions take the form of growing concentric ring-like solutions, that exhibit popcorn like transitions, similar to those of the baryonic popcorn model in the context of holographic dense QCD.

A point particle approximation was proposed, that accurately predicted the transitions, as well as the qualitative form of the solutions for various charges. This was also used to show an emergent symmetry to the more dense packing of solitons for charges $B = 200$ and $B = 250$. This suggests that the minimal energy form for the $B \to \infty$ limit is some symmetric lattice. It would be interesting to investigate this further, especially due to the interesting nature that tessellations take in this space.

The natural extension to this paper is the analogue in the full $(3+1)$-dimensional Skyrme model. We have demonstrated that a multi-ring like structure exists for baby Skyrmions in AdS_3, if this were to translate to the higher dimensional model, it could take the form of multi-shell polyhedrons. This would most naturally be modelled using multi-shell rational maps. If this were the case, it would also suggest some interesting questions for monopoles in the same space. These have been studied before [57] where it was suggested that they take the form of single shell rational maps. It would be interesting to study Skyrmions in AdS_4 and compare the results with both those presented here and the single shelled rational map solutions for monopoles in the same space.

A further extension would be the application to holographic QCD, where a baby Skyrme model has previously been studied as a toy model of the Sakai-Sugimoto model [58]. An alternative suggestion is the use of a vector meson term to stabilise against spatial rescalings. While a little work has been done where the two models gave similar results [59], it would be interesting to see if a pure AdS_3 background would provide qualitatively different results for some parameter regime.

10.7 Appendix A: Local Minima Static Solutions

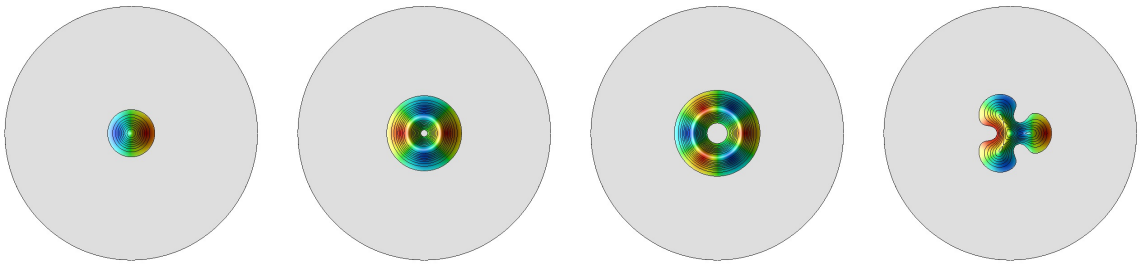

(a) $B = 1$ (b) $B = 2$ (c) $B = 3$ (d) $B = 3$

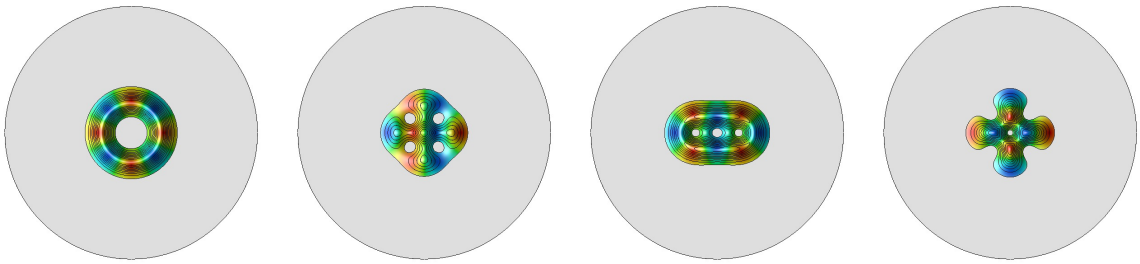

(e) $B = 4$ (f) $B = 4$ (g) $B = 4$ (h) $B = 4$

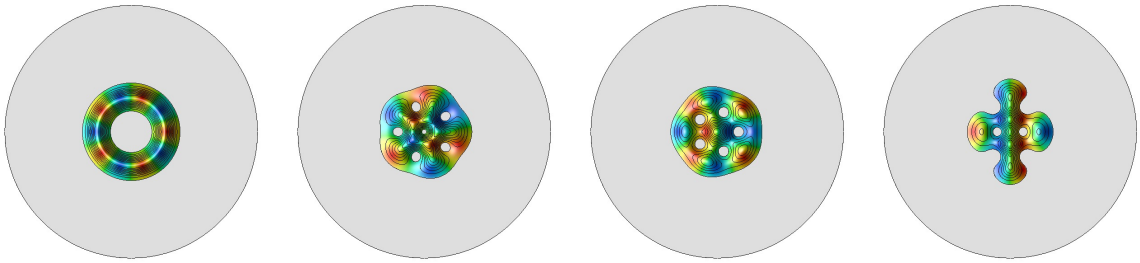

(i) $B = 5$ (j) $B = 5$ (k) $B = 5$ (l) $B = 5$

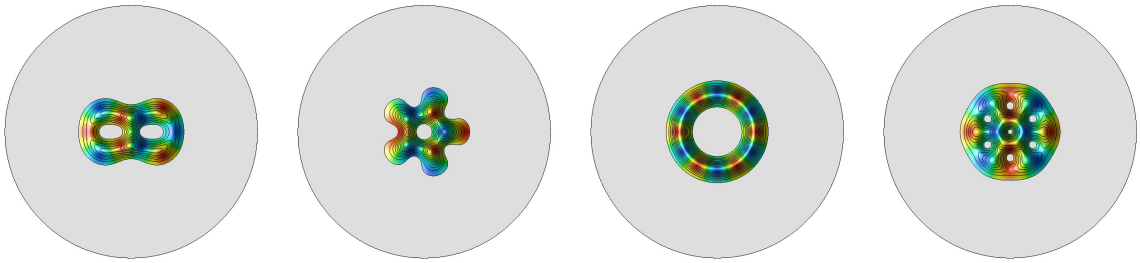

(m) $B = 5$ (n) $B = 5$ (o) $B = 6$ (p) $B = 6$

Figure 10.12: Energy density plots of local minima soliton solutions for charges $B = 1 - 10$, with $\kappa = 0.1$, $L = 1$ and $m = 0$, coloured by the value of ϕ_1.

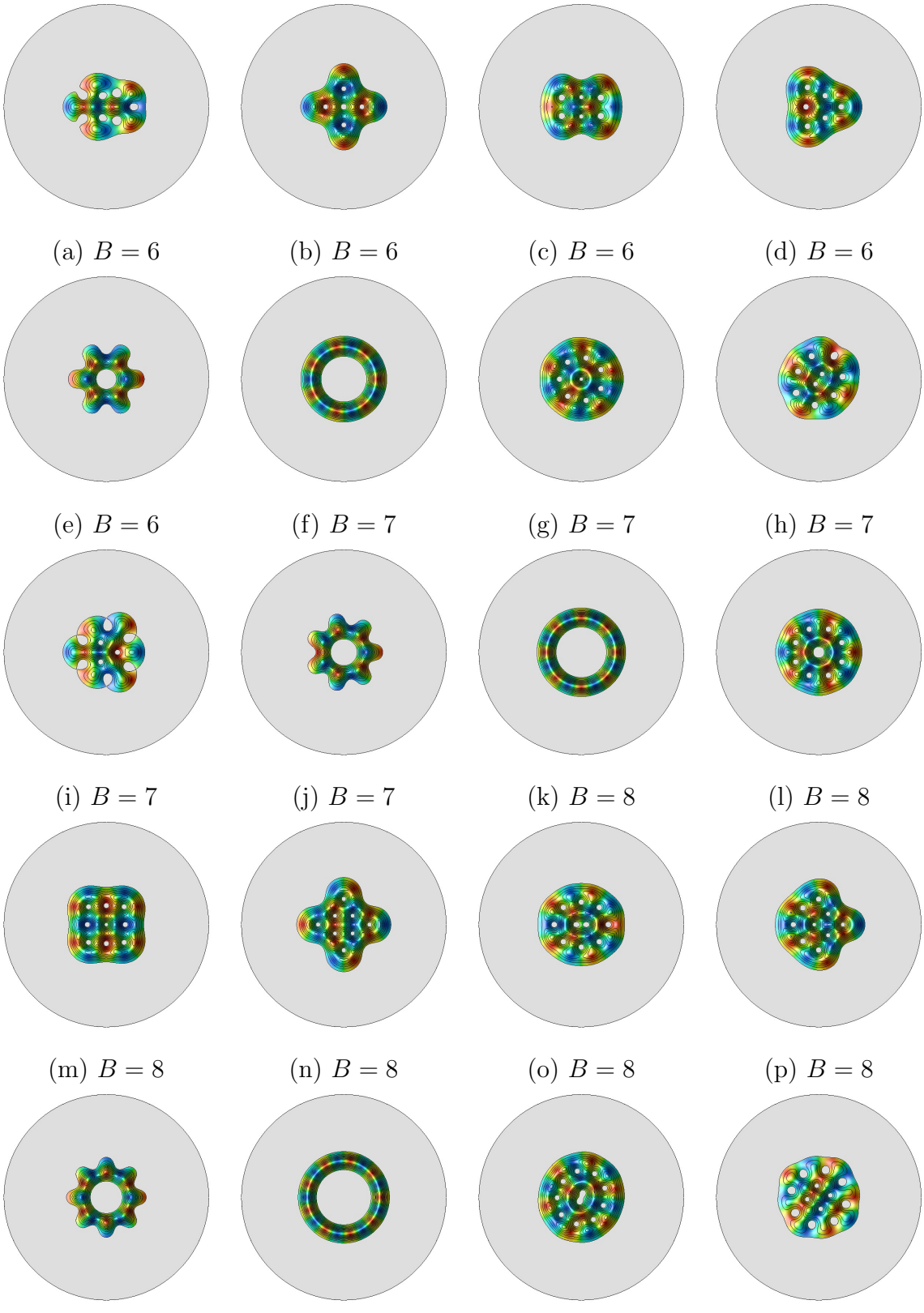

(a) $B = 6$ (b) $B = 6$ (c) $B = 6$ (d) $B = 6$

(e) $B = 6$ (f) $B = 7$ (g) $B = 7$ (h) $B = 7$

(i) $B = 7$ (j) $B = 7$ (k) $B = 8$ (l) $B = 8$

(m) $B = 8$ (n) $B = 8$ (o) $B = 8$ (p) $B = 8$

(q) $B = 8$ (r) $B = 9$ (s) $B = 9$ (t) $B = 9$

Figure 10.13: More energy density plots for local minima soliton solutions for charges $B = 1 - 10$, with $\kappa = 0.1$, $L = 1$ and $m = 0$, coloured by the value of ϕ_1.

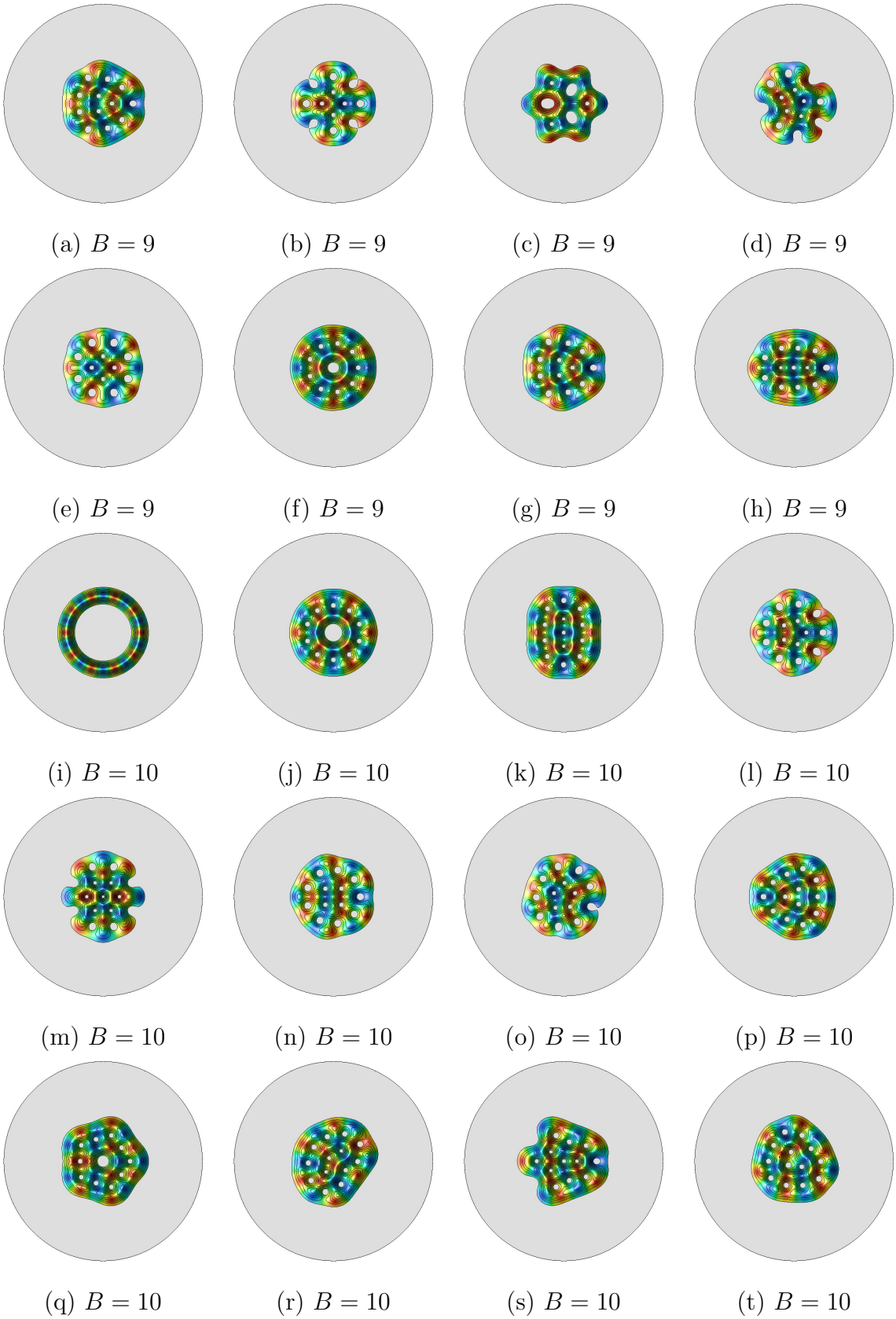

(a) $B = 9$ (b) $B = 9$ (c) $B = 9$ (d) $B = 9$

(e) $B = 9$ (f) $B = 9$ (g) $B = 9$ (h) $B = 9$

(i) $B = 10$ (j) $B = 10$ (k) $B = 10$ (l) $B = 10$

(m) $B = 10$ (n) $B = 10$ (o) $B = 10$ (p) $B = 10$

(q) $B = 10$ (r) $B = 10$ (s) $B = 10$ (t) $B = 10$

Figure 10.14: More energy density plots for local minima soliton solutions for charges $B = 1 - 10$, with $\kappa = 0.1$, $L = 1$ and $m = 0$, coloured by the value of ϕ_1.

Chapter 11

$SU(2)$ Skyrme Model in AdS_4

11.1 Introduction

In the previous chapter we considered the baby Skyrme model in AdS_3, where we showed that solutions take the form of multi-layered concentric rings. The natural extension to this work is to add an extra spatial dimension and consider the full (3+1) $SU(2)$ Skyrme model embedded in AdS_4. We will demonstrate that the prediction made at the end of the previous chapter, that minimal energy solutions will take the form of multi-shell rational maps is correct, at least for low charge solutions. It is also interesting to consider higher charge solutions as we have previously shown in chapter 8 that hyperbolic Skyrmions with massless pions take forms similar to their counterparts in Euclidean space with massive pions. With the curvature of the space forcing solutions towards the origin as well as introducing an effective pion mass term, this could lead to some unforeseen exotic solutions. The work presented in this chapter is intended to appear in a paper at a later date.

11.2 Model

The Lagrangian for the $SU(2)$ Skyrme model on a general Lorentzian manifold M with metric $ds^2 = g_{\mu\nu}dx^\mu dx^\nu$ is given by,

$$L = \int \left\{ -\frac{1}{2} Tr\left(R_\mu R^\mu\right) + \frac{1}{16} Tr\left(\left[R_\mu, R_\nu\right]\left[R^\mu, R^\nu\right]\right) - m_\pi V(U) \right\} \sqrt{-g}\; d^3\boldsymbol{x}. \tag{11.2.1}$$

In sausage coordinates we can write the metric for AdS_4 as,

$$ds^2 = -\left(\frac{1+r^2}{1-r^2}\right)^2 dt^2 + \frac{4L^2}{\left(1-r^2\right)^2}\left(dr^2 + r^2\left(d\theta^2 + \sin^2\theta\, d\varphi^2\right)\right), \tag{11.2.2}$$

where $r \in [0,1)$ and L gives the AdS radius, which is related to the cosmological constant via $\Lambda = -3/L^2$. Similarly to the previous section we use the hyperbolic radius coordinate $\rho = 2L\tanh^{-1}(r)$ to give the alternate metric,

$$ds^2 = -\cosh^2\frac{\rho}{L} dt^2 + d\rho^2 + L^2\sinh^2\frac{\rho}{L}\left(d\theta^2 + \sin^2\theta\, d\varphi^2\right). \tag{11.2.3}$$

The hyperbolic radius has the range $\rho \in [0,\infty)$ and represents the hyperbolic distance from the origin of a given point.

Let us consider the rational map ansatz in AdS_4,

$$U(\rho, z) = \exp\left[\frac{i f(\rho)}{1+|R|^2}\begin{pmatrix} 1-|R|^2 & 2\bar{R} \\ 2R & |R|^2 - 1 \end{pmatrix}\right], \tag{11.2.4}$$

where $f(\rho)$ is a real profile function, with the boundary conditions $f(0) = \pi$ and $f(\infty) = 0$. Substituting this ansatz into the energy that coincides with the Lagrangian (11.2.1), results in the following radial expression,

$$E = \frac{1}{3\pi}\int \left(f'^2 L^2 \sinh^2\frac{\rho}{L} + 2B\left(f'^2 + 1\right)\sin^2 f + \mathcal{I}\frac{\sin^4 f}{L^2\sinh^2\frac{\rho}{L}} + 2m^2 L^2 \sinh^2\frac{\rho}{L}\left(1-\cos f\right)\right)\cosh^2\frac{\rho}{L}\, d\rho \tag{11.2.5}$$

where $\mathcal{I}$ denotes the integral,

$$\mathcal{I} = \frac{1}{4\pi}\int \left(\frac{1+|z|^2}{1+|R|^2}\left|\frac{dR}{dz}\right|\right)^4 \frac{2i\, dz d\bar{z}}{\left(1+|z|^2\right)^2}. \tag{11.2.6}$$

B	E_R	E	G	Figure
1	1.8506	1.8506	$O(3)$	11.1(a)
2	4.0019	3.8822	$O(2) \times \mathbb{Z}_2$	11.1(b)
3	6.2898	5.9923	T_d	11.1(c)
4	8.3593	8.1593	O_h	11.1(d)
5	11.1383	10.6714	D_{2d}	11.1(e)
6	13.7687	13.1400	D_{4d}	11.1(f)
7	15.9506	15.5839	Y_h	11.1(g)
8	19.1875	18.4695	D_{6d}	11.1(h)

Table 11.1: Energies for the rational maps E_R and corresponding single shelled global minimum solutions E for charges $B = 1 - 8$. The symmetry group G of both the rational map and final solution is also included.

As with the flat space case $\mathcal{I}$ must be minimised first by the choice of rational map. As the expression for $\mathcal{I}$ is the same as for the flat space model, the same rational maps can be assumed to minimise the radial energy (11.2.5).

We minimise the energy using a simple gradient flow method, flowing $f(\rho)$ to its minimal energy form. The energies for the parameter choice $L = 1$ and $m = 0$ can be seen in table 11.2 along with their symmetries for charge $B = 1 - 22$. One can also see the first 8 local energies related to the rational map ansatz in figure 11.1 and their energies in table 11.1.

11.3 Multi-Shell Rational Map

In the previous chapter we showed that baby Skyrmion solutions in AdS_3 take the form of highly symmetric multi-layered rings. If this result translates to the results for the full Skyrme model in AdS_4, we may expect configurations to take the form of multi-shelled polyhedral solutions. As we have seen in the previous section, rational maps have polyhedral symmetries and form shell-like solutions. Double-shelled rational maps have been considered in [62] in flat space. They were proposed as an approximate construction of Skyrmions as chunks of the cubic Skyrmion crys-

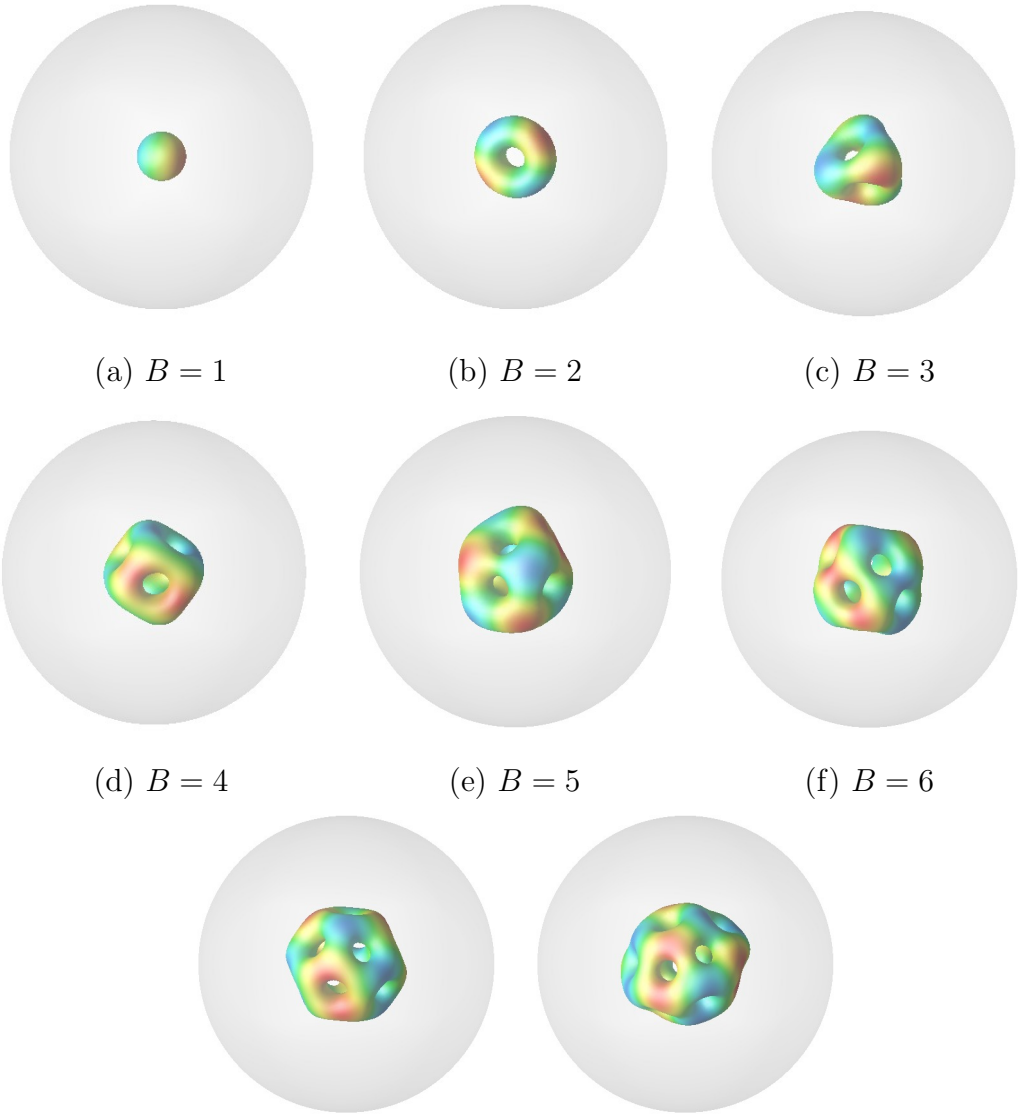

(a) $B = 1$ (b) $B = 2$ (c) $B = 3$

(d) $B = 4$ (e) $B = 5$ (f) $B = 6$

(g) $B = 7$ (h) $B = 8$

Figure 11.1: Energy isosurfaces of the shell like minimal energy solutions that correspond to single-shell rational maps, with $\kappa = 1, m = 0$ for $B = 1 - 8$. The images are coloured based on the value of π_1 and the grey sphere represents the boundary of the space in the Poincare ball model. The energies for these solutions are given in table 11.1.

B	E_R	G	B	E_R	G
1	1.8506	$O(3)$	12	31.4320	T_d
2	4.0019	$O(2) \times \mathbb{Z}_2$	13	34.6596	O
3	6.2898	T_d	14	38.4591	D_2
4	8.3593	O_h	15	41.9903	T
5	11.1383	D_{2d}	16	45.4242	D_3
6	13.7687	D_{4d}	17	48.5426	Y_h
7	15.9506	Y_h	18	52.7858	D_2
8	19.1875	D_{6d}	19	56.6944	D_3
9	22.2371	D_{4d}	20	60.6758	D_{6d}
10	25.1997	D_{4d}	21	64.5541	T
11	28.4272	D_{3h}	22	68.4661	D_{5d}

Table 11.2: Rational map energies E_R for the single shell ansatz for $B = 1 - 22$. The symmetry group G for the rational map is also included.

tal. To generalise the ansatz we can simply change the boundary conditions to be $f(0) = k\pi$, $f(\infty) = 0$. However the energy of this configuration is not particularly low. Hence we will use multiple rational maps that we denote,

$$U(r,z) = \begin{cases} \exp\left(if(r)\,\hat{\boldsymbol{n}}_{R_1(z)} \cdot \boldsymbol{\sigma}\right) & 0 \le r \le r_1, \\ \exp\left(if(r)\,\hat{\boldsymbol{n}}_{R_2(z)} \cdot \boldsymbol{\sigma}\right) & r_1 \le r \le r_2, \\ \qquad \vdots & \\ \exp\left(if(r)\,\hat{\boldsymbol{n}}_{R_n(z)} \cdot \boldsymbol{\sigma}\right) & r_{n-1} \le r \le 1, \end{cases} \tag{11.3.1}$$

where the profile has the fixed points $f(r_k) = (n-k)\pi$, $f(0) = n\pi$ and $f(1) = 0$. Note that while the profile function is continuous, its derivatives are not, and hence U must be treated as a segmented function. The topological charge for this ansatz is simply $B = \sum_{i=1}^{n} N_i$, where N_i is the degree of the rational map in each sector i. This gives the energy of the multi-shell system to be,

$$E = \sum_{i=1}^{n} \int_{r_{i-1}}^{r_i} E_i \, dr \tag{11.3.2}$$

Note that the values for $\mathcal{I}_i$ will not change, hence we will use the same rational maps to minimise the values of $\mathcal{I}_i$. This being said, there is no reason to assume that the full numerical result will have a global minimum with these rational maps and there are more affecting factors. It may be that rational maps with slightly higher values for $\mathcal{I}$ may offer lower energies, due to compatible symmetries. However the energy values for the rational maps with the minimal values for $\mathcal{I}$ should give better upper bounds on the numerical energies.

To find the minimal energy of some multi-shell rational map, we now need to minimise not only multiple profile functions but also the values of r_i. If we perform this process using an annealing method, we acquire the energies given in table 11.3. Note that only the minimal energy multi-shell rational map has been shown in the table. For charges $B = 1 - 10$ the single shell rational maps are the minimal energy. However for charge $B = 11$ we find that a charge one rational map within a charge $B = 10$ rational map has a lower energy than the single shell map by $\sim 2\%$. From this point on the multishell form continues similarly to that of the baby Skyrme model discussed previously. As the charge increases either the outer charge value or inner charge value increases. This is likely due to the outer shell increasing in charge until there is enough room to fit the next charge into the inner map. If one considers the value of r_1, it can be seen that it increases as the charge of the outer rational map increases, indicating that the inner map expands as more space is made available by the larger outer map. Then, when there is enough room to squash the next charge into the inner map the inner charge increases.

11.4 Full Numerical Results

The results for the full field simulations were obtained using a 4^{th}-order Runga-Kutta method, where the kinetic component was cut at regular intervals or if the potential increases. The initial conditions used were the solutions for the multi-shell rational map ansatz with various rational maps. Unfortunately the profile function has discontinuous derivatives and hence the field must be simulated very carefully to prevent the numerical approximations from breaking down.

B	E_{R_s}/B	E_{R_m}/B	r_1	form	B	E_{R_s}/B	E_{R_m}/B	r_1	form
1	1.851	1.851	1	$\{1\}$	12	2.619	2.615	0.252	$\{1,11\}$
2	2.001	2.001	1	$\{2\}$	13	2.666	2.642	0.256	$\{1,12\}$
3	2.097	2.097	1	$\{3\}$	14	2.747	2.681	0.26	$\{1,13\}$
4	2.090	2.090	1	$\{4\}$	15	2.799	2.732	0.289	$\{2,13\}$
5	2.228	2.228	1	$\{5\}$	16	2.839	2.787	0.309	$\{3,13\}$
6	2.295	2.295	1	$\{6\}$	17	2.855	2.812	0.324	$\{4,13\}$
7	2.279	2.279	1	$\{7\}$	18	2.933	2.856	0.328	$\{4,14\}$
8	2.398	2.398	1	$\{8\}$	19	2.984	2.884	0.33	$\{4,15\}$
9	2.471	2.471	1	$\{9\}$	20	3.038	2.906	0.332	$\{4,16\}$
10	2.520	2.520	1	$\{10\}$	21	3.074	2.914	0.333	$\{4,17\}$
11	2.584	2.532	0.247	$\{1,10\}$	22	3.112	2.966	0.337	$\{4,18\}$

Table 11.3: Rational map energies for multi-shell rational map ansatz for $B = 1-22$.

The multi-soliton solutions for $B < 11$ appear to follow the pattern indicated by the rational ansatz taking a single-shell form. The minimal energy configurations for charge $B \geq 11$ however, take the more complicated form of multi-shell solutions. The minimal energies and forms are given in table 11.4.3 for charges $B = 11 - 15$. Certain interesting charges have also been picked out to be discussed below.

11.4.1 $B = 11$

This is the first charge for which the multi-shell form of the rational map ansatz has a lower energy. If we use both the single and multi-shell ansatz as initial conditions, we find this result also holds for the full field simulations. The corresponding energy density isosurface plots can be seen in figure 11.2. So the multi-shell rational map approximation appears to have predicted correctly that the minimal energy form is a multi-shell Skyrmion. Note that we have only considered the standard rational map form for the charge.

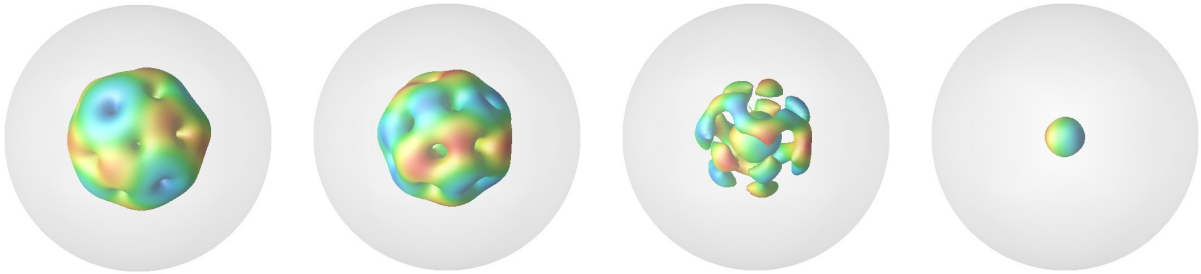

(a) $\{11\}$ (b) $\{1, 10\}$ (c) $\{1, 10\}$ (d) $\{1, 10\}$

Figure 11.2: Energy isosurfaces of the multi-shell solutions found for charge $B = 11$. The first image (a) is the local minimum resulting from minimising the single-shell rational map approximation. The remaining plots (b)-(d) are various values of isosurface for the form $\{1, 10\}$, predicted to be the minimal energy solution by the multi-shell rational map approximation. The images are coloured based on the value of π_1 and the grey sphere represents the boundary of the space in the Poincare ball model.

11.4.2 $B = 12$

While $B = 12$ isn't the first value for the charge to have its rational map energy lowered by introducing multi-shell solutions, it does have several highly symmetric possible solutions. The energies derived from the approximation, propose that $\{1, 11\}$ is the form for the minimal energy solution. However it may be the case that compatible symmetries can produce a lower minimal energy solution. The most natural matching symmetry would be the form $\{6, 6\}$, however this produces a largely inflated value for the energy. Another combination that has a high combined symmetry is the form $\{5, 7\}$, though using alternate forms for $R_5(z)$ and $R_7(z)$ that give slightly higher values for $\mathcal{I}$.

$$R_5(z) = \frac{z\left(z^4 - 5\right)}{-5z^4 + 1} \quad , \quad R_7(z) = \frac{-7z^4 - 1}{z^3\left(z^4 + 7\right)}. \tag{11.4.1}$$

These maps have a shared tetrahedral symmetry generated by,

$$R(-z) = -R(z) \qquad R(1/z) = 1/R(z) \quad R\left(\frac{iz+1}{-iz+1}\right) = \frac{iR(z)+1}{-iR(z)+1}, \tag{11.4.2}$$

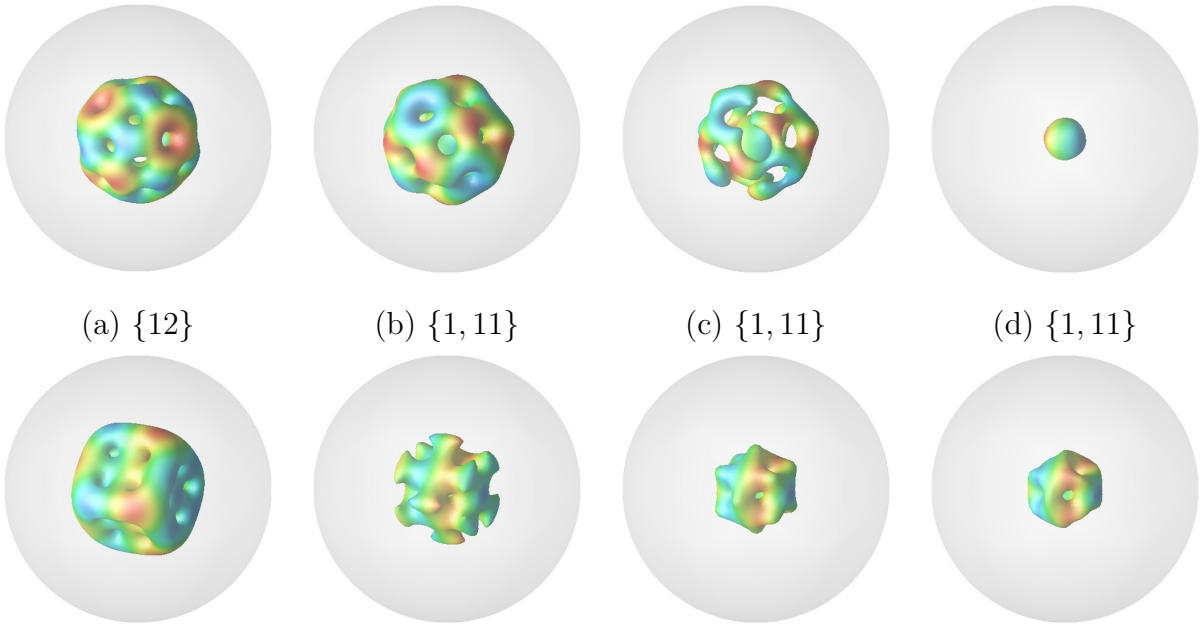

(a) $\{12\}$ (b) $\{1, 11\}$ (c) $\{1, 11\}$ (d) $\{1, 11\}$

(e) $\{5, 7\}$ (f) $\{5, 7\}$ (g) $\{5, 7\}$ (h) $\{5, 7\}$

Figure 11.3: Energy isosurfaces of the multi-shell solutions found for charge $B = 12$. The first image (a) is the local minimum resulting from minimising the single-shell rational map approximation. The remaining plots (b)-(g) are various values of isosurface for the forms $\{1, 11\}$ (predicted to be the minimal energy solution by the multi-shell rational map approximation) and $\{5, 7\}$. The images are coloured based on the value of π_1 and the grey sphere represents the boundary of space in the Poincare ball model.

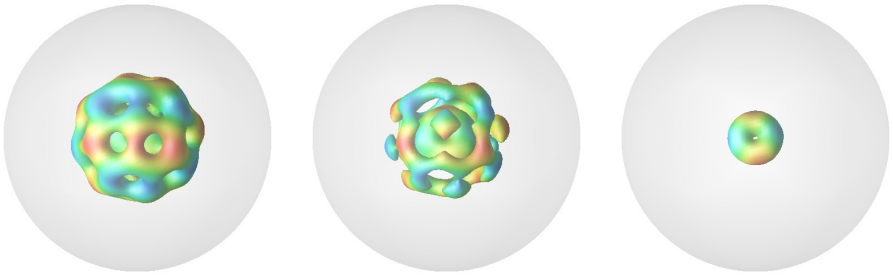

(a) $\{2, 13\}$ (b) $\{2, 13\}$ (c) $\{2, 13\}$

Figure 11.4: Energy isosurfaces of the predicted minimal energy multi-shell solution $\{2, 13\}$ for charge $B = 15$. The image have various values of isosurface which are coloured based on the value of π_1.

along with a $\pi/2$ rotational symmetry $R(iz) = iR(z)$.

We see that this ends up having again a far higher energy than the predicted multi-shell rational map solution. This is a pattern we have observed with several other highly symmetric solutions. This may suggest that it is the size of the multi-shell solution that is more important than the symmetry of the solution which is secondary. Hence the effective gravitational potential dominates.

11.4.3 $B = 15$

The multi-shell rational map ansatz predicts a transition at $B = 15$, in the form of the solutions, from having a single charge soliton at the centre to having a charge 2 soliton at the centre.

For the earlier solutions with charge 1 at the centre it would seem sensible that the outer shells would retain their single shell symmetries, as this gives tightly packed configurations. As the charge 1 centre has a high symmetry, the combined symmetry should then be relatively high. However on increasing the charge of the centre to $B > 1$ there is more to consider in matching symmetries between the outer and inner shell. We have considered the standard form for the rational maps for the solution $\{2, 13\}$ in figure 11.4. While this gives a lower energy than the $\{1, 14\}$ form and $\{15\}$ single-shell form, a larger search considering combined symmetries needs to be performed to be sure it is the minimal energy solution.

B	E/B	form
11	2.46	$\{1, 10\}$
12	2.51	$\{1, 11\}$
13	2.54	$\{1, 12\}$
14	2.59	$\{1, 13\}$
15	2.63	$\{2, 14\}$

Table 11.4: Minimal normalised energies E/B, resulting from minimising the energy of the full field equations with the initial conditions of the multi-shell rational map ansatz, using the rational maps that minimise $\mathcal{I}$, baring a few mentioned examples (that turn out not to be minimal energies anyway).

11.5 Conclusions

We have shown that a multi-shell rational map ansatz has a lower energy for $B \geq 11$. The form of solutions for increasing charge follows a similar pattern to that of the 2-dimensional analogue discussed previously, but with rational maps instead of rings. As the total charge B increases, the outer shell charge increases until there is room for the inner shell to increase.

The full numerical solutions were also considered for several values of charge. It was demonstrated that this multi-shell form extends to the full model. For the charges considered it would appear that the predicted form (from the multi-shell rational map ansatz) is in fact the minimal energy solution, though not necessarily with the same symmetry as predicted.

It is likely that the minimal energy solutions will be those that minimise the size of the solution and maximise the combined symmetry. For those considered the predicted form has a single charge inner rational map, which has an $O(3)$ symmetry naturally. This can easily follow the symmetry of the higher charge outer shell and thus it is unsurprising that the predicted form does indeed minimise the energy. We also considered other solutions that have high combined symmetry but their energies were much higher. This suggests that it is the effective potential of the metric that dominates and must be minimised as a priority over the symmetry of

the solution. This suggests that the multi-shell rational map approximation should give good approximations for the form of solutions.

More work needs to be done on the symmetries of the multi-shell rational maps. Finally it would also be interesting to consider higher charges to see if more exotic solutions start to appear. Massive solutions very quickly start to take the form of cubic crystal chunks in flat space, hence it would be interesting to see if something similar happens in AdS_4.

Part V

Final Remarks

Chapter 12

Conclusions and Further Work

In this chapter we will quickly sum up what has been presented, drawing together the conclusions from each chapter, as well as any questions the work presented here has raised and future work that would be interesting.

We firstly introduced the key principles of the general theory of topological solitons, including existence criteria and stability requirements. These ideas were also demonstrated with a concrete example in ϕ^4-kinks in $(1+1)$-dimensions. Finally the extension to higher dimensions was considered, namely domain walls and sigma models.

In chapter 2 we introduced the baby Skyrme model in (2+1)-dimensions, demonstrating some previously known solutions to the model for low values of topological charge. We then expanded this to higher values of charge, comparing ring like solutions and the previously believed minimal energy solutions, chains of alternating phase. We showed that above a certain charge, dependant on the parameters, the ring like solutions with symmetry D_B become the minimal energy solutions. We also presented a method of predicting the energy of both ring and chain like solutions for various parameters.

We additionally considered two other methods that could form minimal energy solutions, crystal chunk solutions and junctions. Crystal chunk solutions with hexagonal symmetry gave a lower energy but for extremely high values of charge only. Junctions were suggested as a transition between the crystal chunk and ring like solutions. However due to the requirement of multiple junctions and high charge,

finding a solution that reduces the total energy, greater than the accuracy of the numerical simulation, proved difficult and has been suggested as future work. One possible way to circumvent the issues, would be to simulate a junction on a periodic grid, such that the ends of the chains would not interfere with the energy.

We then considered the limit of the topological charge of our systems, showing that the hexagonal crystal is indeed the minimal energy solution for infinite charge, but that the infinite chain or ring (both have the same infinite charge form) have only slightly higher energies.

Finally we demonstrated some dynamical simulations for interesting interactions with ring like solutions. The systems we considered were quite simple, but displayed some interesting behaviour. However one system that hasn't been numerically simulated yet is spin-orbit coupling. A toy model has been considered previously [26] but these ideas could be applied to the baby Skyrme model, along with the idea of ring like solutions.

In chapter 3 we considered a method by which baby Skyrmions can be formed in nature and condensed matter systems, namely domain wall collisions. We demonstrated several situations in which this could occur, showing that the interaction of 3 or more domain wall segments was more reliable than two segments. It was suggested that this could be utilised at a bifurcation point (Y-junction) to create baby Skyrmions at will, in a condensed matter system. This naturally raises some questions as to how reliable this method would be and how to increase this reliability (for example forcing a D_N symmetry is suggested in the chapter itself).

Also presented were simulations for larger systems of domain wall loops. Here the topological charge is conserved and hence any created solitons are counteracted by the creation of anti-solitons that ultimately annihilate. It would be interesting to consider how stimulating an area of space with energy, might form domain walls that interact to form baby Skyrmions and break charge invariance. This could be preformed in a condensed matter system using a laser at a particular point in space.

Chapter 4 considered the affect of breaking the symmetry of the potential term in the baby Skyrme model to the dihedral group D_N, with solutions known as broken baby Skyrmions. This results in a charge 1 solution composed of N topologically

confined partons, represented by different so called colours. The multi-soliton solutions were demonstrated to take the form of polyforms (planar figures formed by regular N-gons joined along their edges). An interesting extension would be to consider the soliton lattice formed by tiling these solutions. While this is likely to produce predictable results for those that tessellate ($N = 3, 4, 6$), for those that don't a more exotic solution is expected.

The dynamics of the model were also considered and shown to depend upon the number of colours N. Each scattering process is broken down into the interactions of the individual partons. Finally the short range forces are shown to differ, where having edges of the polyforms aligned is demonstrated to be energetically favourable. The most natural extension to this work, extending it to the full Skyrme model, is discussed later in the thesis.

Chapter 5 introduces the full $SU(2)$ Skyrme model in $(3+1)$-dimensions. The fundamental concepts are presented with examples given for charge $B = 1 - 8$. The rational map antsatz is also introduced and accuracy indicated. Finally the interaction energy and a simple scattering process is also presented.

In chapter 6 we discuss the extension of chapter 3 to $(3+1)$-dimensions, showing the formation process for Skyrmions from domain wall collisions. As with the previous work it is shown that more than 2 domain walls reduces the amount of constraints required on the initial conditions. The natural extension is to consider domain wall loop systems in 3 spatial dimensions, which would be of interest in cosmology.

Chapter 7 is the extension to the work in chapter 4 to the full Skyrme model. The potential term is modified to consider the affect of breaking the $SU(2)$ symmetry of the model. As with the results in chapter 4 the results can be broken into smaller constituents. We initially consider breaking the isospin invariance of the model, by varying the tree level mass of one of the fields, thus changing it's scale in relation to the others. As the charge increases this leads to particular points on the rational map interacting differently and causes the solutions to be interpreted as being formed of linked toroidal solutions of various charge.

We also consider the extension to the broken baby Skyrmion potential, which

demonstrates a similar splitting of the single soliton into a number of topologically confined partons, positioned in a plane. The results are demonstrated to take the form of shells tiled with polyforms (planar shapes with number of vertices equal to the number of colours). Finally some potentials with polyhedral symmetry are presented, having similar results to the previous potential but with the partons located at the vertexes of the tetrahedron or octahedron.

It would be interesting to extend the work in this chapter to consider the long range inter-lump forces for various types of potential. Additionally some work on the form of a lattice solution would prove interesting, as it could be compared with the results from the broken baby Skyrme results.

Chapter 8 moves on to considering the Skyrme model in curved space, namely hyperbolic $\mathbb{H}^3_\kappa$ with constant negative curvature $-\kappa^2$. It is demonstrated how the profile functions for hedgehog solutions with massless pions take a similar form to those in Euclidean space with massive pions. The form of higher charge solutions was also considered, showing that the minimal energy form becomes the crystal chunk solution for the massless pion case, similar to the results of massive pion solutions in flat space. Finally the dynamics of the model are also considered, showing that scattering occurs along geodesics of the space, with the maximally attractive channel corresponding to a relative rotation of $\pi/2$ around an axis orthogonal to the connecting geodesic.

Chapter 9 then looks at the baby Skyrme model in hyperbolic space presenting some simple results for low charge solutions. The main goal however was to consider the infinite charge lattice in this space. Tessellations are discussed and the complications involved in numerically simulating the baby Skyrmion lattice. The natural extension is finding the minimal energy lattice for the baby Skyrme model. What isn't clear is the affect that changing the parameters of the model would have on the lattice, as the fundamental cell cannot continuously change in the same manner as that of flat space.

Chapter 10 presents the baby Skryme model with an AdS_3 background. The multi-charge static solutions were shown to take the form of concentric rings. As the charge is increased successive transitions occur, dubbed popcorn transitions. The

form of the solutions for higher charges as well as the transition points were predicted using a point-particle approximation, that was tested against the numerical solutions for charge $B = 1 - 20$. It would be interesting to consider the infinite charge limit, which seems to head towards a lattice like structure from the approximation for $B = 200$. It would also be interesting to consider the $O(3)$-sigma model stabilised by a vector meson term in this space and compare the results with those in similar models.

Chapter 11 presents the extension to the previous chapter, namely the full Skyrme model with an AdS_4 background. It was shown that the concentric ring like solutions from the previous chapter extend to multi-shell rational maps in the full model. As the charge increases, the charge contained in each layer of rational map changes in a similar manner to that of the baby Skyrme model. The full numerical solutions appear to follow the rational map ansatz fairly closely, which is surprising as combinations of alternate rational maps have higher combined symmetries.

The extension to this work is to preform a larger search of the possible symmetry combinations for the solutions. Additionally it would be interesting to consider the full numerical solutions for higher charges, as in the hyperbolic model, crystal chunk like solutions start to become favourable. This combined with the centralising affect of the metric could lead to some more exotic solutions than those presented thus far.

Finally the Skyrme model is a rich model with a lot of interesting research currently on going. The key area that has only recently become popular is considering the Skyrme model in curved spaces and I feel this is an area that has and will lead to far more understanding in this model.

Bibliography

[1] P. Jennings and T. Winyard, JHEP **1401**, 122 (2014).

[2] T. Winyard, arXiv 1503.08522 (2015).

[3] M. Elliot-Ripley and T. Winyard, JHEP **09**, 009 (2015).

[4] T. Winyard, arXiv 1507.07482 (2015).

[5] N. Manton and P. Sutcliffe, *Topological Solitons* (Cambridge University Press, Cambridge, 2004).

[6] G. H. Derrick, Math.Phys. **5**, 1252 (1964).

[7] E. Bogomolny, Yad.Fiz. **24**, 861 (1976).

[8] T. Skyrme, Nuclear Physics **31**, 556 (1962).

[9] J. Perring and T. Skyrme, Nuclear Physics **31**, 550 (1962).

[10] A. Vilenkin and E. P. S. Shellard, *Cosmic strings and other topological defects* (Cambridge University Press, Cambridge, 2000).

[11] F. Falk, Zeitschrift für Physik B Condensed Matter **51**, 177 (1983).

[12] W. J. Zakrzewski, Technical report, Los Alamos National Lab., NM (USA) (unpublished).

[13] T. Skyrme, Proc.Roy.Soc.Lond. **A260**, 127 (1961).

[14] B. M. A. G. Piette, B. J. Schroers, and W. J. Zakrzewski, Z.Phys. **C65**, 165 (1995).

[15] J. Sampaio *et al.*, Nature nanotechnology **8**, 839 (2013).

[16] J. Iwasaki, M. Mochizuki, and N. Nagaosa, Nature nanotechnology **8**, 742 (2013).

[17] S. Sondhi, A. Karlhede, S. Kivelson, and E. Rezayi, Phys.Rev. **B47**, 16419 (1993).

[18] X. Z. Yu *et al.*, Nature **465**, 901 (2010).

[19] R. A. Leese, M. Peyrard, and W. J. Zakrzewski, Nonlinearity **3**, 387 (1990).

[20] T. Weidig, Nonlinearity **12**, 1489 (1999).

[21] R. S. Ward, Nonlinearity **17**, 1033 (2004).

[22] J. Jaykka and M. Speight, Phys.Rev. **D82**, 125030 (2010).

[23] D. Foster, Nonlinearity **23**, 465 (2010).

[24] I. Hen and M. Karliner, Phys.Rev. **D77**, 054009 (2008).

[25] B. M. A. G. Piette, B. J. Schroers, and W. J. Zakrzewski, Nucl.Phys. **B439**, 205 (1995).

[26] C. J. Halcrow and N. S. Manton, JHEP **01**, 016 (2015).

[27] A. E. Kudryavtsev, B. M. A. G. Piette, and W. J. Zakrzewski, Nonlinearity **11**, 783 (1998).

[28] M. Nitta, Phys.Rev. **D86**, 125004 (2012).

[29] M. Kobayashi and M. Nitta, Phys.Rev. **D87**, 085003 (2013).

[30] M. Nitta, K. Kasamatsu, M. Tsubota, and H. Takeuchi, Phys.Rev. **A85**, 053639 (2012).

[31] J. Jaykka, M. Speight, and P. Sutcliffe, Proc.Roy.Soc.Lond. **A468**, 1085 (2012).

[32] S. W. Golomb, *Polyominoes - Puzzles, Patterns, Problems, and Packings* (Princeton University Press, Princeton, 1994).

[33] A. Balachandran, V. Nair, S. Rajeev, and A. Stern, Physical Review Letters **49**, 1124 (1982).

[34] A. Balachandran, V. Nair, S. Rajeev, and A. Stern, Phys.Rev. **D27**, 1153 (1983).

[35] E. Witten, Nucl.Phys. **B223**, 422 (1983).

[36] R. A. Battye and P. M. Sutcliffe, Rev.Math.Phys. **14**, 29 (2002).

[37] E. Witten, Nucl.Phys. **B223**, 433 (1983).

[38] T. Sakai and S. Sugimoto, Prog.Theor.Phys. **113**, 843 (2005).

[39] M. F. Atiyah and N. Manton, Phys.Lett. **B222**, 438 (1989).

[40] N. S. Manton and P. M. Sutcliffe, Phys.Lett. **B342**, 196 (1995).

[41] C. J. Houghton, N. S. Manton, and P. M. Sutcliffe, Nucl.Phys. **B510**, 507 (1998).

[42] L. Castillejo *et al.*, Nucl.Phys. **A501**, 801 (1989).

[43] M. Kugler and S. Shtrikman, Phys.Rev. **D40**, 3421 (1989).

[44] M. Kugler and S. Shtrikman, Phys.Lett. **B208**, 491 (1988).

[45] B. J. Schroers, Z.Phys. **C61**, 479 (1994).

[46] S. B. Gudnason and M. Nitta, Phys.Rev. **D91**, 085040 (2015).

[47] I. Hen and M. Karliner, Phys.Rev. **E77**, 036612 (2008).

[48] R. A. Battye, N. S. Manton, and P. M. Sutcliffe, Proceedings of the Royal Society of London A: Mathematical, Physical and Engineering Sciences **463**, 261 (2007).

[49] D. T. J. Feist, P. H. C. Lau, and N. S. Manton, Phys.Rev. **D87**, 085034 (2013).

[50] M. Atiyah and P. Sutcliffe, Phys.Lett. **B605**, 106 (2005).

[51] N. S. Manton and T. M. Samols, J.Phys. **A23**, 3749 (1990).

[52] N. S. Manton and B. M. A. G. Piette, 3rd European Congress of Mathematics, Barcelona, Spain, July 10-14 (2000).

[53] S. Jarvis and P. Norbury, Bulletin of the London Mathematical Society **29**, 737 (1997).

[54] R. Maldonado and N. S. Manton, J.Phys. **A48**, 245403 (2015).

[55] T. Sakai and S. Sugimoto, Prog.Theor.Phys. **114**, 1083 (2005).

[56] S. Bolognesi and D. Tong, JHEP **01**, 153 (2011).

[57] P. Sutcliffe, JHEP **08**, 032 (2011).

[58] S. Bolognesi and P. Sutcliffe, J.Phys. **A47**, 135401 (2014).

[59] M. Elliot-Ripley, J.Phys. **A48**, 295402 (2015).

[60] P. Salmi and P. Sutcliffe, J.Phys. **A48**, 035401 (2015).

[61] R. L. Graham, B. D. Lubachevsky, K. J. Nurmela, and P. R. Östergård, Discrete Mathematics **181**, 139 (1998).

[62] N. S. Manton and B. M. Piette, in *Understanding Skyrmions using rational maps*, Springer (Springer, New York City, 2001), pp. 469–479.